Dissertation
submitted to the
Combined Faculties for the Natural Sciences and for Mathematics
of the Ruperto-Carola University of Heidelberg, Germany
for the degree of
Doctor of Natural Sciences

Put forward by

Diplomant:	Dinko Atanasov
Born in:	Yambol, Bulgaria
Oral examination:	06. July 2016

Precision mass measurements for studies of nucleosynthesis via the rapid neutron-capture process

Penning-trap mass measurements of neutron-rich cadmium and caesium isotopes

Referees:

Prof. Dr. Klaus Blaum
PD Dr. Adriana Pálffy

Zusammenfasung

Obwohl die Theorie über die schnelle Neutronenanlagerung (r-Prozess) schon vor mehr als 55 Jahren entwickelt wurde, wird über den exakten Ort im Universum an dem dieser Prozess stattfindet noch rege debattiert. Theoretische Studien sagen voraus, dass der Verlauf des r-Prozesses geprägt wird durch äußerst neutronenreiche Materie mit sehr asymmetrischen Proton-zu-Neutron Verhältnissen. Die aktuellen Kenntnisse über Eigenschaften dieser neutronenreichen Isotope, die dazu geeignet sind als Eingangsdaten für Studien über den r-Prozess herangezogen zu werden, sind nur unzureichend oder gar nicht vorhanden. Die grundlegenden Eigenschaften der Kerne, wie Bindungsenergie, Halbwertszeiten und Reaktionsquerschnitt spielen eine wichtige Rolle in den theoretischen Simulationen und können diese beeinflussen oder sogar zu drastisch alternativen Ergebnissen führen. Um diese Theorien mit gemessenen Daten zu untermauern und die Produktion neutronenreicher Isotope zu verbessern, wurde an Forschungseinrichtungen wie ISOLDE am CERN, ein gänzlich bemerkenswerter Aufwand betrieben. Das Ziel dieser Dissertation ist es die experimentelle Arbeit zu beschreiben, welche nötig war, um die Präzisionsmassenmessungen der neutronenreichen Isotope Cadmium ($^{129-131}$Cd) und Cäsium ($^{132,146-148}$Cs) zu ermöglichen. Die Messungen wurden an der Isotopenfabrik ISOLDE am CERN mithilfe des aus vier Ionenfallen bestehenden Massenspektrometers ISOLTRAP durchgeführt. Die Cadmium Isotope sind Schlüssel-Nuklide, um die Häufung der im Sonnensystem beobachteten Massenverteilung bei der Massenzahl $A = 130$ zu beschreiben.

Abstract

Although the theory for the rapid neutron-capture process (r-process) was developed more than 55 years ago, the astrophysical site is still under a debate. Theoretical studies predict that the r-process path proceeds through very neutron-rich nuclei with very asymmetric proton-to-neutron ratios. Knowledge about the properties of neutron-rich isotopes found in similar regions of the nuclear chart and furthermore suitable for r-process studies is still little or even not existing. The basic nuclear properties such as binding energies, half-lives, neutron-induced or neutron-capture reaction cross-sections, play an important role in theoretical simulations and can vary or even drastically alternate results of these studies. Therefore, a considerable effort was put forward to access neutron-rich isotopes at radioactive ion-beam facilities like ISOLDE at CERN. The goal of this PhD thesis is to describe the experimental work done for the precision mass measurements of neutron-rich cadmium ($^{129-131}$Cd) and caesium ($^{132,146-148}$Cs) isotopes. Measurements were done at the on-line radioactive ion-beam facility ISOLDE by using the four-trap mass spectrometer ISOLTRAP. The cadmium isotopes are key nuclides for the synthesis of stable isotopes around the mass peak $A = 130$ in the Solar System abundance.

Contents

Abstract iii

Contents iv

List of Figures vii

List of Tables ix

Acknowledgements xi

1 Introduction 1
- 1.1 Nuclear structure . . . 1
- 1.2 History of nuclear astrophysics . . . 3

2 Ion traps 7
- 2.1 Basics of Penning traps . . . 7
- 2.2 The Penning trap . . . 7
  - 2.2.1 Real Penning traps . . . 10
  - 2.2.2 Manipulation of charged particle's motion . . . 15
  - 2.2.3 Destructive Time-of-Flight Ion-Cyclotron-Resonance detection technique . . . 18
- 2.3 Multi-reflection time-of-flight mass spectrometry . . . 21
- 2.4 Developments in multi-reflection ion-traps . . . 22
  - 2.4.1 Basic principle . . . 22

3 Experimental setup 25
- 3.1 The Isotope Separation On-Line at ISOLDE . . . 25
- 3.2 The ISOLTRAP mass spectrometer . . . 28
  - 3.2.1 Offline reference ion source . . . 29
  - 3.2.2 Radiofrequency quadrupole buncher . . . 30
  - 3.2.3 Multi-Reflection Time-of-Flight mass separator . . . 31
  - 3.2.4 Preparation Penning trap . . . 34
  - 3.2.5 Precision Penning trap . . . 37

4 Data analysis and results 39
- 4.1 Principle of mass determination using a Penning trap . . . 39
  - 4.1.1 Analysis procedure . . . 40

4.2 Multi-reflection time-of-flight mass spectra . . . 42
4.2.1 Analysis Procedure . . . 44
4.3 Results . . . 46
4.3.1 Neutron-rich cadmium isotopes . . . 47
4.3.1.1 ^{129}Cd isotope . . . 48
4.3.1.2 ^{130}Cd isotope . . . 50
4.3.1.3 ^{131}Cd isotope . . . 52
4.3.2 Neutron-rich caesium isotopes . . . 52
4.3.2.1 ^{132}Cs isotope . . . 52
4.3.2.2 ^{146}Cs isotope . . . 52
4.3.2.3 ^{147}Cs isotope . . . 53
4.3.2.4 ^{148}Cs isotope . . . 53

5 Physics Interpretation **55**
5.1 Macroscopic-Microscopic mass models . . . 55
5.2 Microscopic mass models . . . 57
5.3 Empirical separation energies and shell gaps . . . 57
5.4 Basics of nucleosynthesis . . . 61
5.5 The element abundance equation . . . 62
5.5.1 Neutrino-driven-wind core-collapse supernovae . . . 64
5.5.2 Compact binary mergers . . . 65
5.6 Results from the r-process calculations . . . 66
5.7 Conclusions and Outlook . . . 68

A Magnetic field at ISOLTRAP - mapping and alignment **71**
A.1 Nuclear magnetic resonance instrument (NMR probe) . . . 71
A.2 3-axis Magnetometer (Hall probe) . . . 72
A.3 Alignment of the Magnetic Field . . . 73
A.3.1 Electron guns - Operation and Detection . . . 73
A.4 **Electron gun Test Bench** . . . 77
A.4.1 Electron guns for Upper & Lower SUMA . . . 77
A.4.2 Test results . . . 77
A.5 Final alignment . . . 78

B Experimental spectra and Analysis results **81**
B.1 Results from the 2014 experimental run . . . 81
B.1.1 ToF-ICR for ^{129}Cd isotope . . . 81
B.1.2 ToF-ICR for ^{130}Cd isotope . . . 82
B.2 Results from the 2012 experimental run . . . 83
B.2.1 ToF-ICR for ^{132}Cs isotope . . . 83
B.2.2 ToF-ICR for ^{146}Cs isotope . . . 84
B.2.3 ToF-ICR for ^{147}Cs isotope . . . 85
B.2.4 ToF-ICR for ^{148}Cs isotope . . . 86

List of Figures

1.1 Binding energy per nucleon . . . 2
1.2 Differences in mass-model predictions for Cd isotopes . . . 3
1.3 Solar System abundances . . . 5

2.1 Schematic drawing of Penning traps . . . 8
2.2 Electric potential . . . 9
2.3 Motion in ideal Penning trap . . . 11
2.4 Magnetic field drift . . . 13
2.5 Dipolar and quadrupolar excitation schemes . . . 16
2.6 Calculations of the final magnetron radius . . . 17
2.7 Principle of the time-of-flight cyclotron resonance detection technique . . . 19
2.8 A typical Time-of-flight resonance . . . 20
2.9 Ramsey type time-of-flight ion-cyclotron resonance . . . 21
2.10 Schematic drawing of electric potential of the multi-reflection time-of-flight device 22

3.1 The ISOLDE facility . . . 26
3.2 Target unit used in the cadmium experiment . . . 27
3.3 Yield simulation from UCx target . . . 29
3.4 ISOLTRAP schematic drawing . . . 30
3.5 Radio-frequency cooler and buncher trap . . . 31
3.6 Multi-reflection time of flight mass separator . . . 32
3.7 Mass spectrum of $A = 160$ . . . 34
3.8 Release curve from the target for $^{148}Cs^{+}$ . . . 35
3.9 Preparation Penning trap . . . 36
3.10 Precision Penning trap . . . 38

4.1 Asymmetry in the peak shape of the multi-reflection mass spectrum . . . 45
4.2 Different peak shapes comparison . . . 46
4.3 ^{85}Rb cross-check measurements . . . 47
4.4 ^{129}Cd time-of-flight ion-cyclotron-resonance spectrum . . . 48
4.5 ^{129}Cd half-live measurement . . . 49
4.6 Excitation energy of the $11/2^{-}$ in odd-A cadmium isotopes . . . 50
4.7 ^{130}Cd time-of-flight ion-cyclotron-resonance spectrum . . . 51
4.8 Mass-excess values from each frequency ratio of ^{130}Cd . . . 51
4.9 ^{131}Cd time-of-flight mass spectrum . . . 52
4.10 Results from different trapping times of ^{131}Cd . . . 53
4.11 Mass excess comparison . . . 54

5.1 Two-neutron separation energy in the region around ^{130}Cd nuclide 58
5.2 One- and two-neutron separation energy for the Cd and Cs isotopes 59
5.3 Empirical one-neutron shell gap 60
5.4 Solar System isotopic *r*-residuals 62
5.5 Reaction cross-section calculations 66
5.6 Calculations of elemental abundances assuming core-collapse supernovae scenario . 67
5.7 Calculations of elemental abundances assuming neutron-star merger scenario . . . 68

A.1 Magnetic field inhomogeneity at z=0 plane 72
A.2 Axial magnetic field strength 72
A.3 Complete axial magnetic field 73
A.4 UT comparisson field 74
A.5 Electron gun parts 75
A.6 Increase of the electron beam radius 75
A.7 Helmholtz coils - magnetic field profile 76
A.8 E-gun test results 78
A.9 Schematic drawing of e-guns 79

List of Tables

1.1 Mass uncertainty required by different fields of applications 2

4.1 Experimental runs - summary 40
4.2 Frequency or Time-of-Flight ratios - summary 49

5.1 Predictive power of nuclear mass models 56

A.1 Electron-gun dimensions 78

B.1 Fit results for ^{129}Cd 82
B.2 Fit results for ^{130}Cd 82
B.3 Fit results for ^{132}Cs 83
B.4 Fit results for ^{146}Cs 84
B.5 Fit results for ^{147}Cs 85
B.6 Fit results for ^{148}Cs 86

Acknowledgements

First of all, I would like to express my gratitude to both of my supervisors Prof. Dr. Klaus Blaum and PD Dr. Yuri A. Litvinov, who gave me a chance to become a PhD student in their group. Thank you very much for being always an open and positive people with who one could have plenty of discussions. I learned a lot from you about physics and life in general and will cherish this experience until the end of my life.

Prior my arrival at CERN, I did not have any idea about the existence of the ISOLTRAP experiment. It turned out to be an experiment as old as me. Following my arrival in Geneva, I met the local ISOLTRAP team, great professionals that welcomed me and accepted me as part of their daily routines. Now after all these years of work together, I would like to thank them all for their support and care.

Special thanks to Dr. Susanne Kreim for her enormous help not only in our common work on the Penning-trap data analysis, but also in helping me with some everyday problems. Special acknowledgements go to Frank Wienholtz, the man behind the machine. I learned many techniques in the lab from you for which I am in debt. I specially would like to thank Dr. Vladimir Manea, the person with whom I shared an office for about 3 years. In this period you proven to be a never failing source of information concerning physics, philosophy, literature and music. During our discussions I have learned so much that I can not describe it in one sentence.

I thank Dr. Christopher Borgmann and Dr. Dennis Neidherr, the people that helped me understand the complexity of the ISOLTRAP's Control System (CS). Behind the great success of each ISOLTRAP experiment is hidden an enormous work on the flawless operation of the CS. I would like to acknowledge Dr. Robert N. Wolf and Dr. Marco Rosenbusch. I had plenty of pleasant beers accompanied by very nice physics topics in the last 4 year. I hope that this continues in the future as well. I would like also to thank the members of the ISOLTRAP collaboration for the nice moments during the collaboration meetings, and in particular would like to wish to the new members of the local team Andreé Welker and Maxime Mougeot success in their future work with this amazing apparatus.

I would like to specially acknowledge Dr. David Lunney for his inspiring ideas that concluded in the work described in this thesis. Furthermore, I thank Dr. Stephané Goriely, for performing the astrophysical calculations presented here.

I am thankful to Dr. Nicolas Winckler, the man who introduced me to the Maximum-Likelihood analysis. This method is applied to the acquired data from the multi-reflection time-of-flight device.

The measurements of exotic and short-lived species begin with the production of the radioactive beam itself. I would like to express my gratitude to the ISOLDE technical group, who's continuous effort to improve the quality of the beam production made these measurements possible. And in particular, I am grateful to the target, RILIS and the operators teams.

I also thank Dr. Deyan T. Yordanov, that helped me a lot during the first year of stay at CERN. I thank my colleagues at GSI for the countless nice moments while starting my PhD. And specifically I would like to acknowledge Prof. Dr. Fritz Bosch, Dr. Shahab Sanjari, Dr. Christophor Kozhuharov, Dr. Pierre-Michel Hillebrand, Dr. Oleksandr Kovalenko and Dr. Daria Schubina.

Last, but not least I want to thank Julieta and my family for the support that they provided during the write-up process. I am very happy to have such an amazing people around me.

To all of you, Thank you!

Dedicated to Julieta and my family...

Chapter 1

Introduction

The identity of atoms is given among other characteristics by their mass. Each nuclide has its own mass value different from all the others. Currently, the masses of more then 3000 nuclides out of the 7000 theoretically expected to occur [Erl+12] have been measured and only about 300 of them are stable. The atomic mass is a fundamental nuclear property and it is inherently connected to the nuclear binding energy. The binding energy itself reflects the interplay of strong, weak and electromagnetic interaction [BLS08] in the atomic system. The importance of mass measurements for short-lived exotic atoms ranges from the verification of nuclear mass models to testing the Standard Model, e.g. with respect to the weak interaction and the unitarity of the Cabibbo–Kobayashi–Maskawa quark mixing matrix [HT09; HT15].

Additionally, the accurate mass measurements contribution goes beyond nuclear and particle physics. The level of accuracy in the atomic mass measurements varies with the requirements of the applications in use. Several examples for the required mass precision are given in Table 1.1. The mass precision from the table relevant for the measurements described in this thesis is in the order of 10-100 keV/c^2. This level of accuracy is sufficient for studies of nuclear shell effects as well as some applications in nuclear astrophysics [Bla06].

1.1 Nuclear structure

Definition of the nuclear mass $M(N, Z)$ is given by the sum of the masses of its separated nucleons (neutrons m_ν and protons m_π mass) minus the total binding energy $BE(N, Z)$, i.e. the energy required to separate the nucleus in its building blocks [BM98]:

$$M(N, Z) = Nm_\nu + Zm_\pi - \frac{BE(N, Z)}{c^2}, \tag{1.1}$$

with Z, N representing the proton and neutron numbers and c being the speed of light. Throughout the elements, the binding energy per nucleon ($A = Z + N$) seems to saturate around 8.5 MeV/c^2 with a group of elements around iron being the most bound, while lightest, like hydrogen, or heaviest, like uranium, being less tightly bound. This trend, presented in Fig. 1.1, was first established through a systematic mass measurement study performed on more then 200 isotopes by F. Aston [Ast23; Ast22]. Conclusion drawn from this study was found in agreement with the concept of the nuclear forces being saturable, which afterwards led to the development of the

Table 1.1: Required relative mass uncertainty $\delta m/m$ as well as the absolute uncertainty δm calculated for a mass $A = 100$ u by various applications in research.

Application	**Research area**	**δm/m**	**δm**
Chemistry	Ionic or molecular specie identification	$10^{-7} - 10^{-4}$	10 keV/c^2 - 100 MeV/c^2
Nuclear Physics	Nuclear structure, mass models	$10^{-7} - 10^{-6}$	10 - 100 keVc^2
Astrophysics	Stellar nucleosynthesis	$10^{-7} - 10^{-6}$	10 - 100 keV/c^2
Weak Interaction	Testing CVC hypothesis and CKM unitarity	$\leq 10^{-8}$	$\leq$ 1 keV/c^2
Metrology	Fundamental constants	$\leq 10^{-9}$	$\leq$ 100 eV/c^2
Atomic Physics	Atomic binding energies, QED	$\leq 10^{-10}$	$\leq$ 10 eV/c^2
Particle Physics	CPT invariance test	$\leq 10^{-11}$	$\leq$ 1 eV/c^2

liquid-drop model of the nucleus, proposed by G. Gamow [Gam30], C. F. von Weizsäcker [Wei35], and Bethe and Bacher [BB36].

This phenomenological formula had a huge impact on the later developments in nuclear theory. The model quickly became the reference with respect to which all nuclear effects could be revealed. One example is the enhanced binding for certain nuclei found as deviations of the nuclear binding energies from the liquid-drop model (LD). This enhanced nuclear stability for some specific values of Z and N played a crucial role in the development of the independent particle model [May49] and

Figure 1.1: The distribution of the binding energy as a function of the mass number. The data presented in the graph contains all measured isotopes from the atomic mass evaluation. In the inset plot a zoom on the chart of nuclides in the region with the highest binding energy per nucleon.

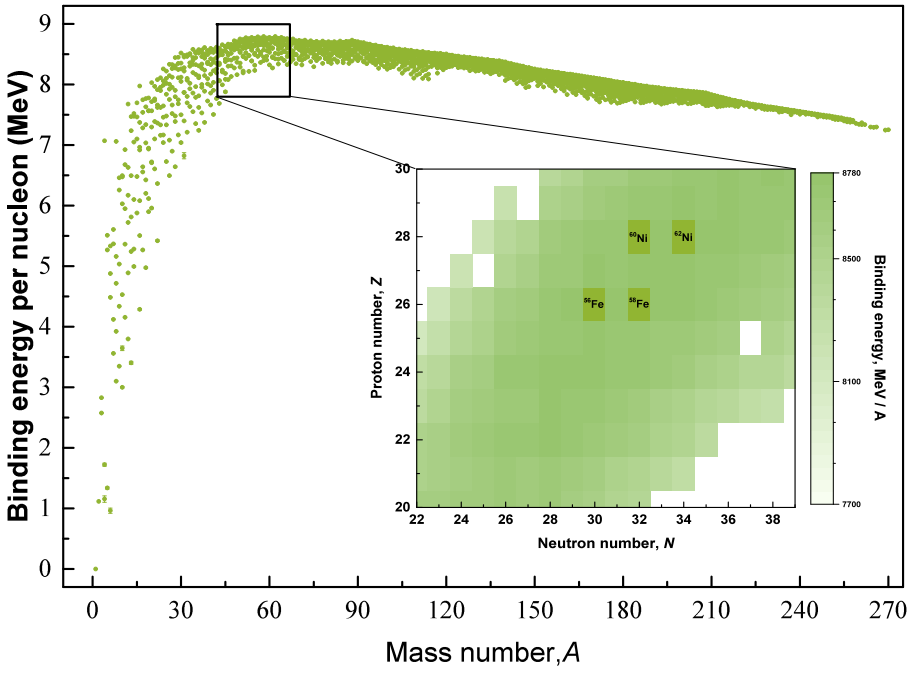

the establishment of "*magic*" nuclear numbers (for N and $Z = 8, 20, 28, 50, 82$ and 126). In that framework description of the nuclear system was given by filling shells with independently moving particles. The deviation at these numbers showed that the nucleus is more bound suggesting an internal structure coexisting with the liquid drop picture.

The theoretical description experienced a huge progress in the last few decades mainly driven by the increase of computational power and by the increasing amount and precision of the available experimental data. For instance, taking closer look at the Atomic mass evaluation [AW95; WAT03; Aud+12a], in 1995 there were about 1800 masses known experimentally, while in the year 2012 this number increased to 3353 (2438 experimental masses and 915 estimated ones). Most of the nuclear mass models nowadays seems to agree within this experimentally known region. However, they seem to diverge by several MeV for unknown exotic nuclides. The disagreement between different mass models is presented in Fig. 1.2.

1.2 History of nuclear astrophysics

The "*nuclear mass defect* ΔM" defined as $M(N, Z) - Nm_\nu - Zm_\pi$, also commonly referred to as "*mass excess*", was at first determined by Aston in his mass measurements, where he showed that the helium atom would have less atomic mass compared to 4 hydrogen atoms [Ast21]. At the same time this discovery was identified by Eddington as being the energy that could be released

Figure 1.2: Comparison of different mass models taken from [Kou+00; Liu+11; Möl+12; Gor+09; RAM15] in the Cd isotopic chain. The mass model by Duflo and Zuker (DuZu) [DZ95; BHM12] was chosen to be a reference. This way a comparison for isotopes with no available experimental data is shown. The experimental data is given by points and taken from the AME2012 [Aud+12a].

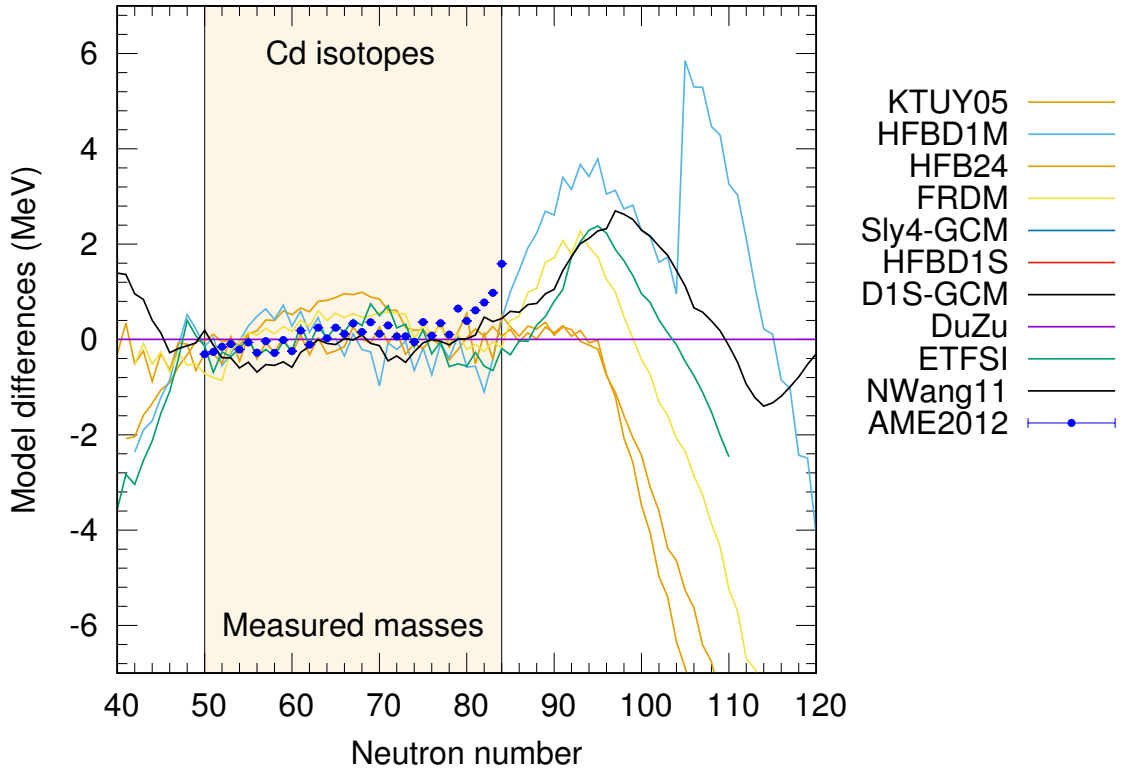

through nuclear reactions in the stellar burning processes [Edd20]. He quantitatively showed that such energy generation could balance the gravitational potential of the outer layers of a star. The energy equivalent of the mass defect can be written in terms of the famous mass-energy relation of Einstein yielding $\Delta E = \Delta M(N, Z)c^2$, which is exactly the total binding energy from Eq. (1.1). Further development by Gamow [Gam28] and independently by Gourney and Condon [GC29] gave explanations of the quantum mechanical probability for particles tunnelling through potential barriers. Later this result was endorsed by Atkinson and Houtermans [AH29] as being the driving force for energy generation of stars through fusion reactions. Later in the work of C. F. von Weizsäcker [Wei38] and H. Bethe [Bet39], the fusion idea was further developed to explain the build up of elements heavier then ^{4}He using carbon, nitrogen and oxygen as catalyst in the reactions. However, in these papers the heavier elements were assumed to be already existing before the star formation. Intense research on this topic concluded in the famous overview papers of Burbidge, Burbidge, Fowler, and Hoyle [Bur+57] and the independent work of Cameron [Cam57], setting up the basis of nucleosynthesis process of heavy elements through means of various nuclear reactions. Further reading about the history of the nuclear physics and in particular nuclear astrophysics can be found in the Chapter *History* of Ref. [Ili07].

The abundances of chemical elements

All elements that surround us, make up life or the celestial objects in the sky have been and are still being produced by nuclear reactions in the interiors of stars. The observational data of the elemental abundances is presented in the lower and upper panels of Fig. 1.3. It represents a complete evaluation of the three most reliable sources nowadays, namely the solar photosphere, carbonaceous chondrites meteorites and some minor theoretical calculations [LPG09]. This observational data is the only evidence for the underlying nuclear process that power the stars.

In the lower panel of Fig. 1.3, the distribution of elements versus their proton number follows at first a steep decrease and only after the peak around $Z = 26$ (commonly referred as "the iron peak") rather flat dependence towards heavier uranium. In the latter part of this distribution, there are a few exceptions of peaks found at the closed nuclear shells. It was also noticed that there is a preference between the production of odd- and even-A elements [Har17], shown for clarity in upper panel of Fig. 1.3. Explanation of this effect can be discussed within the framework of the nucleon-nucleon pairing correlations, in which the coupling of two valance particles (even number) is more stable configuration having lower ground-state energy than in the case of only one particle (odd number).

Nuclear masses as input for r-process calculations

Whereas observational astronomy/astrophysics provides conditions for astrophysical processes to occur, with other words temperatures, pressure, density and chemical composition, the nuclear physics supplies with characteristics for the nuclear landscape such as masses, lifetimes, cross-sections etc. for some important transient isotopes such as the neutron-rich cadmium isotopes. Hence, nuclei and stars are deeply interconnected as stellar evolution might depend on nuclear structure and vice versa nuclear properties can be modified in the stellar interior. Thus, redrawing the pathways for the creation of nuclear matter can be done only by careful investigation, which includes many steps of experimental measurements in nuclear physics and theoretical modelling in astrophysics [Bos03].

Figure 1.3: Abundance distribution versus proton number representing the abundance of chemical elements in our Solar System is presented in lower panel. The data presented in the plot was compiled using experimental evidences from solar photosphere and corona and meteorite (in particular Cl chondrites). In the upper panel the same data is presented versus the atomic number A and split in two groups - even- and odd-A isotopes. Clearly the nuclides with even-A mass numbers are strongly produced.

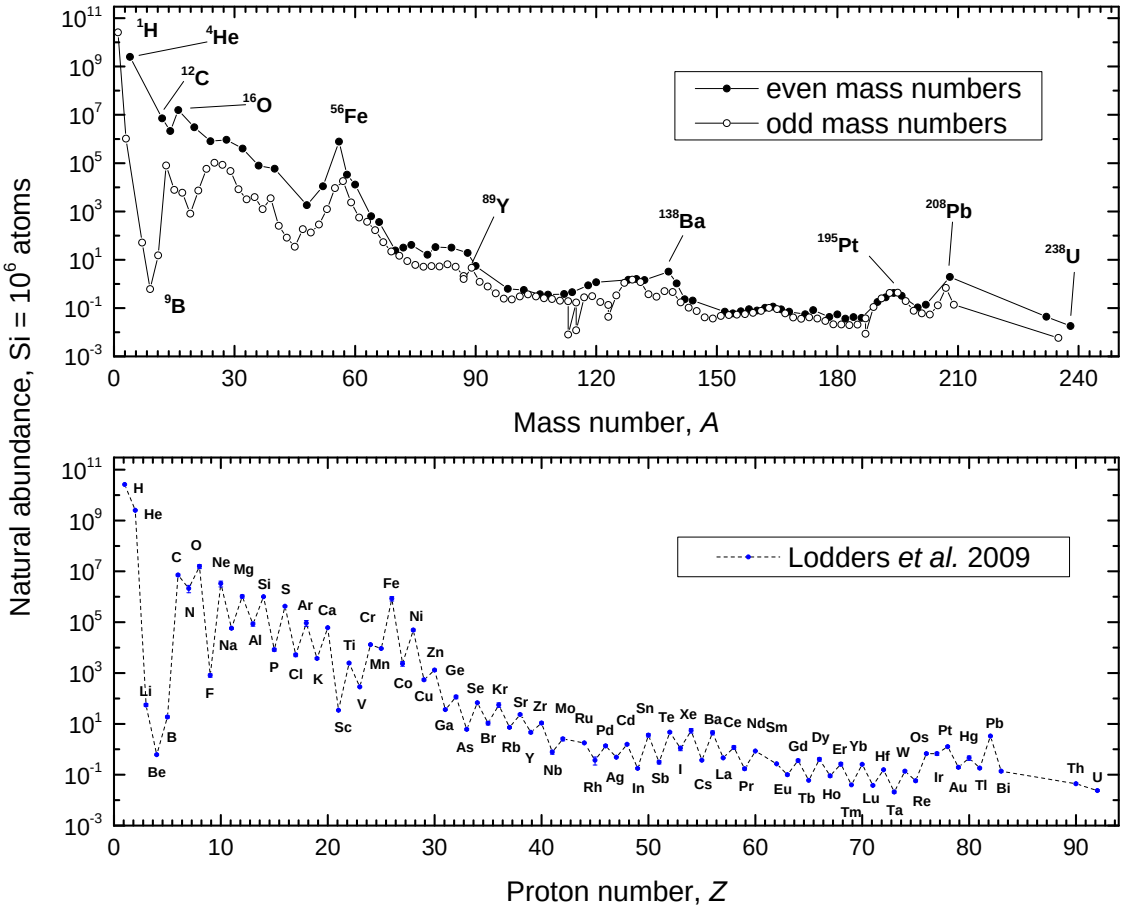

One of the most important nuclear ingredients in astrophysical calculations are the nuclear masses [LW01]. They determine the flow pathway of the nucleosynthesis reactions. Most of the relevant nuclides for the r-process involved in those reaction are experimentally unknown and are only theoretically estimated by nuclear mass models. Estimations are traditionally based upon adjusting to the known nuclear masses. Whether phenomenological or microscopic, mass models rely on measured masses for adjusting their parameters. While measuring masses farther from stability should help constrain the predictions, the final impact depends on how many new masses are used, how far they are from what is known and the less quantifiable inherent uncertainty of the model.

In the past, nuclear research was essentially limited to only stable elements [Bos03], but nowadays radioactive ion-beam facilities exist worldwide, delivering beams of exotic short-lived species. The neutron-rich cadmium and caesium isotopes, described in this work, are just one example of the many such nuclides that can be measured at these facilities.

Chapter 2

Ion traps

Mass spectrometry has a rich history spanning over the last 100 years. Some of the developments made within the field are summarised in a special issue of the International Journal of Mass Spectrometry [BL13]. In that edition, the reader can find description of various techniques developed over the years to address measurements of the masses of many stable nuclei. Furthermore, many novel techniques are described investigating more and more exotic and short-lived radionuclides. The measurements that dominate the field are based on the determination of the revolution frequency as these are in general more precise than position measurements. In short, the mass determination is achieved by the measurement of the frequency with which an ion revolves in a magnetic field. Ion traps and storage rings are examples of devices applying this method. The difference in volume and size between both devices is huge. While storage ring has typically a circumference of many several tens of meters the ion trap has a volume of about one cubic centimetre. But the main feature of these devices is their ability to conduct measurements on stored short-lived single ions by using sophisticated detection techniques like the non-destructive resonant Schottky spectroscopy [FGM08] in the case of storage rings or the ion cyclotron resonance (ICR) in the case of Penning traps.

2.1 Basics of Penning traps

The highest-precision mass measurements can be achieved using the so-called Penning traps [BG86], which have been developed by H. Dehmelt [Deh90] based on the idea of F. M. Penning [Pen36]. This Chapter highlights the main principles for describing Penning traps and is mainly based on the detailed previous work of Brown and Gabrielse [BG86] as well as Bollen [Bol+96] in the case of short-lived nuclides. Nowadays, there are two main types of Penning traps commonly used at experimental setups. In Fig. 2.1 a simple schematic drawing of both types is given. The first kind of Penning traps is based on electrodes with hyperbolic shapes while the second one uses cylindrically-shaped electrodes.

2.2 The Penning trap

In the ideal Penning-trap configuration, trapping of charged particles is achieved by the superposition of a magnetic ($\vec{B} = B_0\vec{e}_z$) and an electrostatic ($\vec{E} = -\nabla\Phi$) field. A static DC potential is

applied to the end cap electrodes in order to confine the ions axially. Expression about the form of the potential can be written as a multipole field and in this specific case as a quadrupole potential:

$$\Phi(x, y, z) = \frac{V_0}{2r_0^2}(2z^2 - x^2 - y^2). \tag{2.1}$$

It is convenient to describe the potential in cylindrical coordinates (with $r^2 = x^2 + y^2$) as the shape of the electrodes creating it have symmetry along the axial direction. Thus, the potential can be re-written as

$$\Phi(r, z) = \frac{V_0}{2d^2}(z^2 - \frac{r^2}{2}) \tag{2.2}$$

where we have introduced a trap characteristic parameter d defined as

$$d^2 = \frac{1}{2}(z_0^2 + \frac{r_0^2}{2}) \tag{2.3}$$

where r_0 denotes the inner ring radius and $2z_0$ is the closest distance between the two end caps. Figure 2.2 shows the electric quadrupole potential and the electric field in cylindrical coordinates.

Figure 2.1: Schematic representation of the two different types of Penning traps. On the left the hyperbolic-shaped electrode configuration and on the right the cylindrical-shaped electrode configuration. Both configurations consist of a ring and two opposing end cap electrodes.

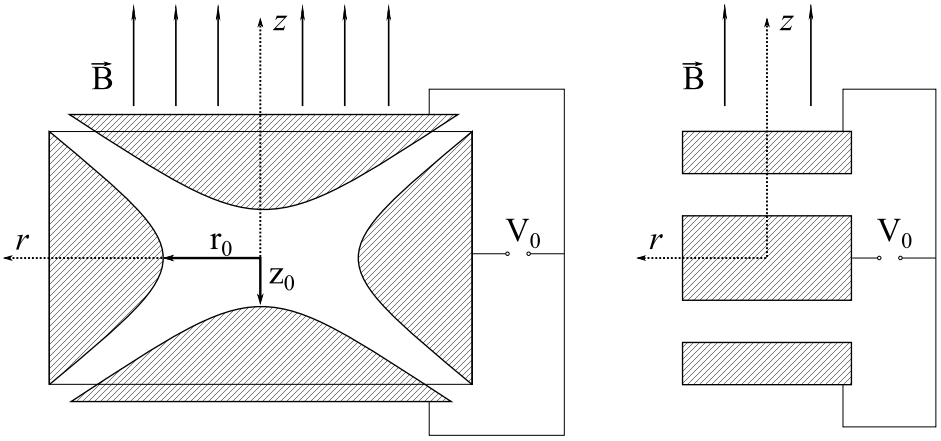

The particles motion is generated by a Lorentz force ($\vec{F}_L$), which points in the direction of the centre of the trap. In an ideal Penning trap, the axial motion or the motion between the two end caps is going to be decoupled from the magnetic field and will be described by a simple harmonic oscillator

$$\ddot{z} + \frac{qV_0}{Md^2}z = 0 \tag{2.4}$$

where q and M are the charge and the mass of the particle, respectively. The solution of the differential equation is

$$z(t) = A_z(0)\cos(\omega_z \cdot t + \varphi_z(0)), \tag{2.5}$$

where $A_z(0)$ and $\varphi_z(0)$ describe the amplitude and the phase of the particles while the oscillator (axial) frequency (ω_z) describes the axial motion periodicity

$$\omega_z^2 = \frac{qV_0}{Md^2}. \tag{2.6}$$

The magnetic field confines the charged particle radially and it performs a circular oscillating

Figure 2.2: Contour colour plot representing the electric quadrupole potential in the (z, r) plane. The electric field is presented with white arrows pointing to the direction of the field.

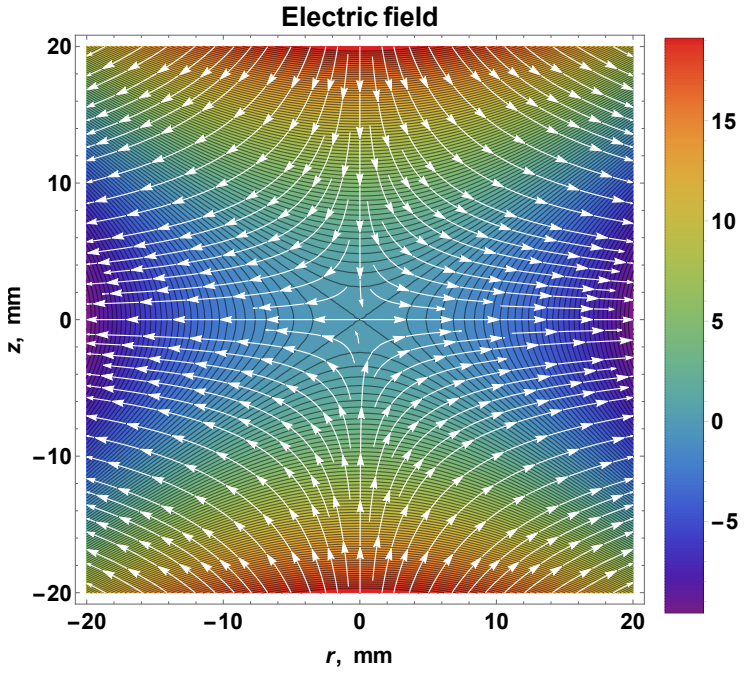

motion with the angular frequency called cyclotron frequency

$$\omega_c = \frac{q}{M} \cdot \mathrm{B} \tag{2.7}$$

For the configuration shown in Fig. 2.1, description of the motion in the radial plane (r) is given by computing the Lorentz force and using Newton's second law

$$M\ddot{\vec{r}} = q(\vec{E_r} + \dot{\vec{r}} \times \vec{\mathrm{B}}), \tag{2.8}$$

where $\vec{r}$ is a radius vector describing the position of the ion at any instant. E_r is the radial part of the electric field derived from the quadratic potential in Eq. (2.2). For convenience, one can re-write the equation of motion:

$$\ddot{\vec{r}} - \omega_c \vec{e}_z \times \dot{\vec{r}} + \frac{1}{2}\omega_z^2 \vec{r} = 0. \tag{2.9}$$

From Eq. (2.9) it becomes obvious that for small axial frequencies (ω_z) the equation reduces to a uniform circular motion at the true cyclotron frequency (ω_c). The existence of a third term is a small modification coming from the repulsive radial part of the electrostatic potential. The general form of the equation in a Cartesian coordinate system can be expressed by two second order linear

differential equations shown below in a matrix form for clarity

$$\begin{bmatrix}\ddot{x}\\ \ddot{y}\end{bmatrix} - \omega_c \begin{bmatrix}\dot{y}\\ -\dot{x}\end{bmatrix} + \frac{\omega_z}{2}\begin{bmatrix}x\\ y\end{bmatrix} = 0. \tag{2.10}$$

To solve the latter a new variable substitution of the type $u = x + iy$ can be made. After the substitution we get

$$\ddot{\vec{u}} + i\omega_c\dot{\vec{u}} + \frac{1}{2}\omega_z^2\vec{u} = 0. \tag{2.11}$$

The solution of this equation is of type $u = e^{-i\omega t}$, which gives rise to the following parametric equation:

$$2\omega^2 - 2\omega_c\omega + \omega_z^2 = 0 \tag{2.12}$$

The roots of this quadratic equation gives the angular eigenfrequencies $\omega_\pm$

$$\omega_\pm = \frac{1}{2}(\omega_c \pm \sqrt{\omega_c^2 - 2\omega_z^2}) \tag{2.13}$$

where the solution is given as

$$u = C_+ e^{-iw_+ t} + C_- e^{-iw_- t} \tag{2.14}$$

with $C_\pm$ being arbitrarily chosen complex constants. Going back to the Cartesian coordinate system we obtain for the solution of the two radial motions

$$\begin{bmatrix}x\\ y\end{bmatrix} = r_- \begin{bmatrix}\cos(\omega_- t - \varphi_-)\\ -\sin(\omega_- t - \varphi_-)\end{bmatrix} + r_+ \begin{bmatrix}\cos(\omega_+ t - \varphi_+)\\ -\sin(\omega_+ t - \varphi_+)\end{bmatrix}. \tag{2.15}$$

The two motions are called modified cyclotron motion (with the angular frequency of ω_+) and the magnetron motion (with angular frequency of ω_-). The latter motion is a slow drift motion caused by the cross product of the electric and magnetic field. The following relations apply to the frequencies of the ion motion:

$$\omega_+ + \omega_- = \omega_c \tag{2.16}$$

$$2 \cdot \omega_+ \cdot \omega_- = \omega_z^2 \tag{2.17}$$

$$\omega_+^2 + \omega_-^2 + \omega_z^2 = \omega_c^2 \tag{2.18}$$

Eq. (2.18) is called invariance theorem [BG86] and connects all eigenfrequecies with the true cyclotron frequency. The motion arising from the superposition of the three independent motions is shown in Fig. 2.3. Measurements of frequencies nowadays are being among the most precise and accurate experimentally obtained variables. Hence, it is obvious why Penning-trap mass spectrometry is focused on frequency measurements - the very precise determination of the cyclotron frequency can be achieved and with that one has precise knowledge about the particle's mass. In this ideal context, the only constrains are the good knowledge of the strength of the magnetic field as well as the charge of the particle. In the next section we will look at the imperfections that can alternate this ideal picture about the motions of particle in a Penning trap.

2.2.1 Real Penning traps

In a real Penning trap there are many factors that lead to deviations from the ideal case. Such trap irregularities will produce shifts in the three eigenmotions and thus modify the eigenfrequecies. Therefore, the value and the uncertainty of the determined masses will be changed due to systematic errors in the system. The knowledge of such imperfections is thus essential for the understanding

Figure 2.3: Schematic trajectory of a charged particle in a Penning trap: Oscillation in the axial direction (motion with eigenfrequency ω_z) and the projection onto the $x-y$ plane representing the radial motion of the particle (a superposition of slow magnetron ω_- and fast cyclotron ω_+ motions) [Bla06].

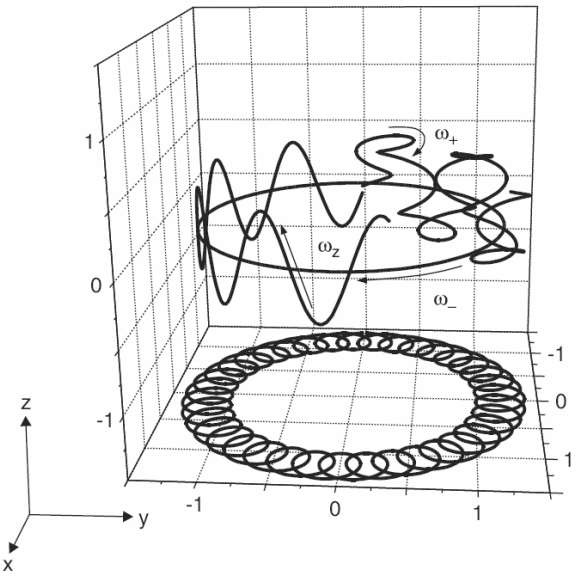

and estimating the systematic errors in the mass determination. Below only the most important trap imperfections will be discussed.

Electric field imperfections

The electric field imperfections are generated by the deviations from the perfect quadrupole potential as defined in Eq. (2.2). Such deviations arise due to mechanical or practical reasons, such as the finite size of the electrodes, the purity of the electrode's material used in the manufacturing process or the injection and ejection holes in the end caps for eternally produced ions. Therefore the field in the trap will always deviate from the ideal case by generating higher order multipoles. There exists calculation for the frequency shifts caused by octupole or dodecapole contributions and are given by [Bol+90]. The general form of the electric potential is then given as

$$\Phi(r,z) = \frac{V_0}{2}\left\{\frac{C_2}{d^2}(z^2-\frac{r^2}{2}) + \frac{C_4}{d^4}(z^4 - 3z^2r^2 + \frac{3}{8}r^4) + \right. \\ \left. + \frac{C_4}{d^4}(z^6 - \frac{15}{2}z^4r^2 + \frac{45}{8}z^2r^4 - \frac{5}{16}r^6) + \dots)\right\}. \tag{2.19}$$

For an ideal quadrupole potential the coefficients $C_4 = C_6 = 0$ and $C_2 = 1$. In any other case the higher orders corrections to the electric field will alternate the ideal eigenfrequencies. Thus, the measured cyclotron frequency ($\omega_c = \omega_+ + \omega_-$) will be shifted by [BG86]:

$$\Delta\omega_c^{elec} = \frac{3}{4}\frac{\omega_z^2}{(\omega_+ - \omega_-)}\left[\frac{C_4}{d^2}(r_-^2 - r_+^2) + \frac{10}{4}\frac{C_6}{d^4}\{3z^2(r_-^2 - r_+^2) + (r_-^4 - r_+^4)\}\right]. \tag{2.20}$$

The first coefficient can be expanded in terms of the magnetron frequency ω_- by using Eq. (2.17):

$$\frac{\omega_z^2}{\omega_+ - \omega_-} = \frac{2\omega_-}{1 - \omega_-/\omega_+} \approx 2\omega_- \approx \frac{V_0}{2d^2 B} \tag{2.21}$$

From here it can be seen that the shift in the cyclotron frequency due to electric field imperfections is in first order approximation mass independent. Minimisation of such shifts can be achieved either by storing the ions with small oscillating amplitudes or by using large characteristic trap dimension d. Furthermore, by applying a small trap potential V_0 and introducing compensation or correction electrodes higher orders of multipoles (C_4 and C_6 coefficients in the potential) can be minimised as well. In addition frequency shifts can be reduced by using cold particles with small amplitudes of the ion motions.

Magnetic field inhomogeneity

The cyclotron frequency measurements aiming at accurate mass determinations demand a high homogeneity and temporal stability of the magnetic field. Currently, magnetic fields with strengths of several Tesla can be produced by using superconducting magnets. However, changes in the temperature and pressure of the cooling liquid as well as instabilities or even impurities of the material in the superconducting coils can cause a steady decrease of the strength of the magnetic field over certain periods of time. Commercial superconducting magnets in high-precision mass spectrometry are used since they usually provide very homogeneous magnetic fields in a small volume in the vicinity of the trap centre. Typical homogeneities in the order of $\Delta\mathrm{B}/\mathrm{B} < 10^{-7}/cm^3$ can be achieved nowadays. Another useful property of the magnetic field is the temporal stability over long periods of time. Currently, the world best temporal magnetic stability achieved is in the order of $(\Delta\mathrm{B}/\mathrm{B})/\Delta T < 17\ ppt/h$ [Van+99], while typical value for magnets installed at ISOLTRAP setup is $(\Delta\mathrm{B}/\mathrm{B})/\Delta T \sim 28\ ppb/h$. Measurements of the magnetic field drifts for a period of over of 3 days for one of the magnets is shown in Fig. 2.4. The homogeneity can be worsen if a material with magnetic susceptibility is introduced to the field. Such material can be simply the trap itself or the surrounding electrostatic optics. Usually materials with low susceptibility (oxygen-free high-conductivity copper and glass ceramics) are used for the trap components. Nevertheless, noticeable perturbations in the field can be observed. Systematic frequency shifts can arise if for example the magnetic field is a function of the even powers of the distance from the trap centre [BG86]. The lowest order correction for the cyclotron frequency can then be derived from the magnetic hexapole component of the magnetic field

$$\mathrm{B} = \mathrm{B}_0\beta_2(z^2 - \frac{r^2}{2}), \tag{2.22}$$

where B_0 is the magnetic field strength at the centre of the trap and β_2 represents the relative strength of the hexapole component. The cyclotron frequency shift is then given by

$$\Delta\omega_c \approx \beta_2\omega_c(r_z^2 - \frac{r^2}{2}) \tag{2.23}$$

During the year 2013, a maintenance of the ISOLTRAP's magnets was carried out aiming to refurbish and improve them. After close examination, they were repaired and brought back in operation. Current values of the magnetic field strength and the relative drifts were measured. The results of the measurements as well as some properties of the magnets can be found summarised in Appendix A.

Figure 2.4: The drift of the magnetic field for one of the magnets installed at ISOLTRAP over a period of 75 hours (lower panel). In the upper panel the day-night drifts are extracted from the linear decay of the magnetic field.

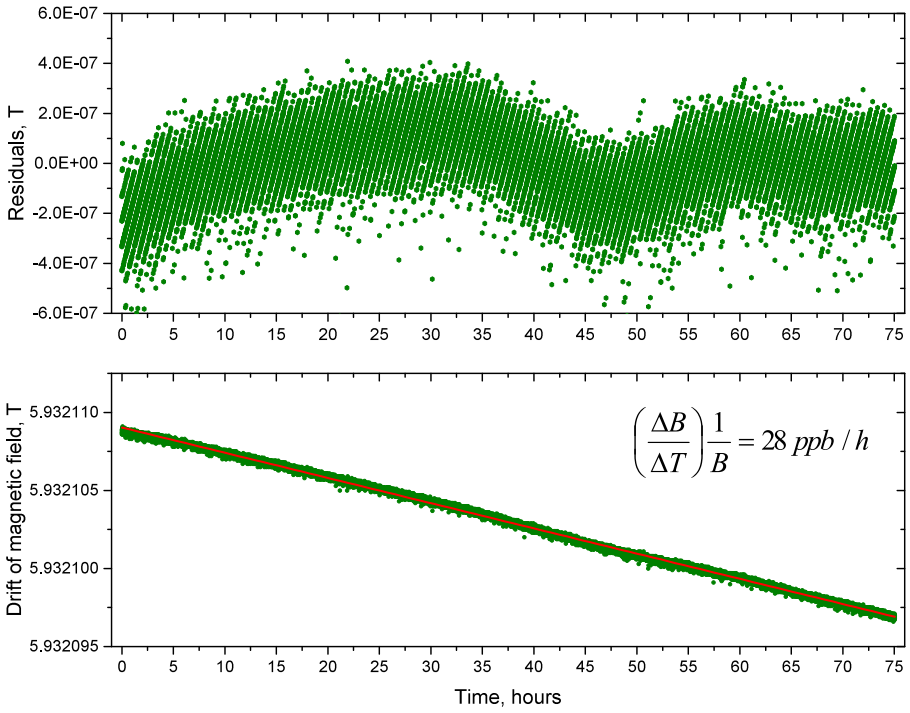

Misalignments

In the ideal case the magnetic field axis is perfectly perpendicular to the radial $(x - y)$ plane. The axial motion in such case is decoupled and the multiplication constants were chosen such that the particles oscillate with the axial eigenfrequency ω_z. In reality, there will always be a small tilt angle between the magnetic field axis and the principle axial in our case the axial direction of the trapping electrostatic field. Again, a misalignment results in systematic frequency shifts of all eigenfrequencies perturbing the frequencies from the values of an ideal trap ω_c, ω_z and ω_- to the values $\overline{\omega}_c$, $\overline{\omega}_z$ and $\overline{\omega}_-$, respectively. The misaligned fields then can be treated in a more general way following [BG86; Bol+90]. For the magnetic field one could write the expression in terms of the angle θ between the magnetic field at the trapping centre and the principle axis plus the angle ϕ that the x axis makes with the plane containing the previous two or

$$\begin{aligned} \mathrm{B}_x &= \mathrm{B}_0 \sin\theta \cos\phi \\ \mathrm{B}_y &= \mathrm{B}_0 \sin\theta \sin\phi \\ \mathrm{B}_z &= \mathrm{B}_0 \cos\theta. \end{aligned} \tag{2.24}$$

The asymmetric electrostatic potential can be expressed in the lowest order approximation (the azimuthal quadrupole component) in terms of an ellipticity parameter ϵ as

$$\Phi(x, y, z) = \frac{m\omega_z^2}{2} \cdot \left[z^2 - \frac{1}{2}\left(x^2 + y^2 - \epsilon(x^2 - y^2) \right) \right] \tag{2.25}$$

Expressing the equations of motion of trapped charged particles, one obtains three coupled, second-order linear differential equations. Assuming a time dependent solution of type $u(t) = e^{-i\omega t}$ a homogeneous system of equations can be derived. The set of equations has a solution, which

is determinant by a characteristic equation, stating that the determinant of the system is zero. Hence, one could obtain the observable cyclotron $\overline{\omega}_+$, axial $\overline{\omega}_z$ and magnetron $\overline{\omega}_-$ frequencies by the following relations

$$\overline{\omega}_+^2\overline{\omega}_z^2\overline{\omega}_-^2 = \frac{1}{4}\omega_z^6(1-\epsilon^2) \tag{2.26}$$

$$\overline{\omega}_+^2\overline{\omega}_z^2 + \overline{\omega}_+^2\overline{\omega}_-^2 + \overline{\omega}_z^2\overline{\omega}_-^2 = \omega_c^2\omega_z^2(1-\frac{3}{2}\sin^2\theta - \frac{\epsilon}{2}\sin^2\theta cos2\phi) - \frac{3}{4}\omega_z^4(1+\frac{\epsilon^2}{3}) \tag{2.27}$$

$$\overline{\omega}_+^2 + \overline{\omega}_-^2 + \overline{\omega}_z^2 = \omega_c^2 \tag{2.28}$$

where the last equation represents the fundamental Brown-Gabrielse invariance theorem [BG86; Bol+90]. The deviation from the ideal case or the systematic frequency shift $\Delta\omega_c^{tilt} = \overline{\omega_c} - \omega_c$ can be shown to be mass independent, for small angles $\theta << 1$ and small ellipticity $\epsilon << 1$ (the ϕ dependence is insignificant)

$$\Delta\omega_c^{tilt} \approx \frac{9}{4}\omega_- \sin^2\theta. \tag{2.29}$$

During the commissioning stage this particular systematic shift was investigated. Alignment of the magnetic field axis with respect to the principle axis was carried out. Using collimated electrons emitted from a hot cathode and placed at the center of the magnetic field, the angle θ could be minimised as low as $\theta = 0.08$ mrad. More information about the whole procedure can be found in Appendix Appendix A.

Storing more then one particle

High-precision mass measurements normally require only few particles at a time of the measurement stored in the trap. Due to their ionisation state, particles can influence each other via Coulomb interaction. Such interactions lead to modifications of particles motions and hence frequency shifts. These Coulomb effects have been studied extensively in Penning traps [Bol94]. Results from these studies give a quite conclusive picture on the frequency shifts that can be observed.

If the stored particles are having comparable masses, the excitation field (see later) will act on the centre of the charge over mass cloud. In such case frequency shifts are not observed. This is not the case whenever the species simultaneously stored in the trap are differing in mass. The contaminating species introduce a frequency shift $\Delta\omega_{Cb}$ in the obtained resonance. The shift size increases with the number of the contaminating particles. The sign of $\Delta\omega_{Cb}$ was found to depend strongly on the difference in the cyclotron frequencies compared to the width of the resonance. When the mass resolving power ($R = M/\Delta M$) is insufficient, a resonance at the common centroid of the two species is obtained. This resonance is narrower compared to simple superposition and corresponds to the average of all stored particles in the trap. When both species are resolved and a double resonance is observed, the frequency associated to each specie will be shifted towards lower frequencies. The frequency shift was found to be proportional to the number of the contaminating ions.

Measurements of radioactive particles at on-line beam facility, such as ISOLDE, often can not be performed on a sample with a few particles of only one single specie in the sample. The major drawback of the ISOL-type facilities (see Chapter 3), for example, is the delivery of contaminating particles together with the particles of interest. This contamination can either be isobars, molecular compounds that originate from the target source or ionised rest gas produced by charge exchange or energetic electrons emitted in beta decay. In order to check for contaminations and estimate the resulting frequency shift, a post-analysis procedure was developed [Kel+03]. The cyclotron

frequency is determined as a function of the number of particles present in the trap for one cycle. A linear least-square fit is then applied on the resulting curve from which the unperturbed cyclotron frequency and its uncertainty are deduced by extrapolation to single ion trapped, accounting for the detector efficiency.

2.2.2 Manipulation of charged particle's motion

The stored particles in the Penning trap are usually manipulated during the measurement process by external radiofrequency (rf) electric fields. The effects of the radiofrequency fields depend on the type (multipolarity) of the excitation as well as its frequency. The most common excitation schemes used with Penning traps are dipolar and quadrupolar rf excitations. With the dipolar fields an excitation of all eigenmotions is possible and the net result is an increase of their motional amplitudes. In the case of the second excitation, the quadrupolar field allows the manipulation of two eigenmotions simultaneously at either the sum ($\omega_{rf} = \omega_+ + \omega_-$) or the difference ($\omega_{rf} = \omega_+ - \omega_-$) of the eigenfrequencies [Bol94].

In the ideal Penning trap, the eigenmotions of the particles can fully be described by using quantum mechanics [BG86; Bla+03a]. The total energy of the quantum mechanical system is given by the sum of the energy for each individual eigenmotion yielding the following relation

$$E = \hbar\omega_z(n_z + \frac{1}{2}) + \hbar\omega_+(n_+ + \frac{1}{2}) - \hbar\omega_-(n_- + \frac{1}{2}), \tag{2.30}$$

where $n_z, n_+, n_- = 0, 1, 2\ldots$ are the principle quantum numbers of the corresponding eigenmotions with 0 being the ground state of the particle. The potential energy of the particle in the radial plane is negative as the particles experience a potential hill in the direction towards the centre of the trap. Nevertheless, the contribution to the total energy from the modified cyclotron motion is always positive due to its large kinetic energy. In contrast, the magnetron motion contributes to the total energy with a negative sign, making this motion unbound or metastable. This special property of the magnetron motion plays an important role when the particles' motion is cooled via a buffer-gas cooling technique (see Sec. 3.2.4).

In the following sections, the dipolar and quadrupolar excitation schemes will be described in more detail. The different schemes applied to the system can produce excitation from one quantum state to another. For this purpose the ring electrode is four-fold segmented allowing a radiofrequency to be applied as shown in Fig. 2.5.

Dipolar excitation

This type of excitation can be applied to an electrode configuration presented in the left panel of Fig. 2.5. The resulting electric field created in addition to the quadrupole trapping potential is described by the following equation

$$\vec{E}_d(t) = -\frac{V_d}{a}\cos(\omega_{rf}t + \phi_{rf})\vec{e}_x \tag{2.31}$$

where $\omega_{rf}, V_d, \phi_{rf}$ are adjustable parameters for the frequency, amplitude and phase, respectively. The radial part of the coupled differential equations can now be written as:

$$\ddot{\vec{u}} + i\omega_c\dot{\vec{u}} - \frac{1}{2}\omega_z^2\vec{u} = -\frac{q}{m}\frac{V_d}{a}\cos(\omega_{rf}t + \phi_{rf}). \tag{2.32}$$

Figure 2.5: Schematic view of the four-fold segmented ring electrode and different configurations for the excitations schemes. On the left: combination of electrodes used for dipolar rf excitation. On the right: electrode configuration used for quadrupolar rf excitation.

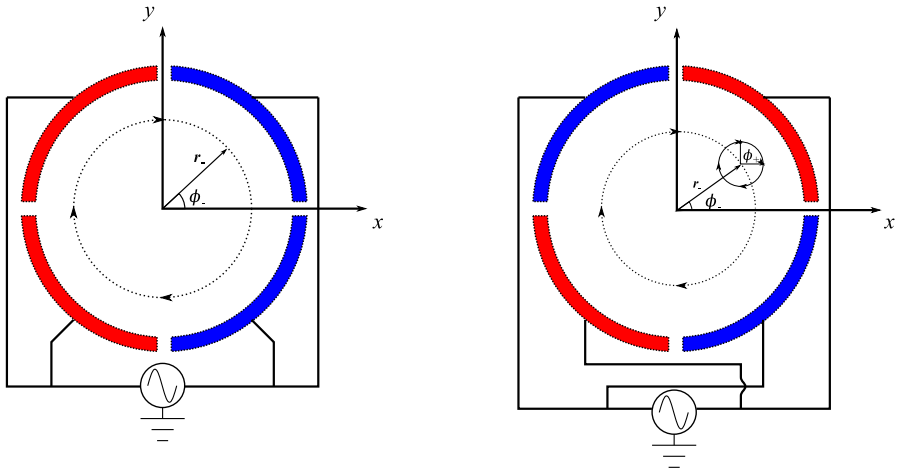

The solutions of these equations will have the same form as before, but now with the exception that the radii $r_\pm$ have a time dependency

$$\begin{bmatrix} x(t) \\ y(t) \end{bmatrix} = r_-(t) \begin{bmatrix} \cos(\omega_- t - \phi_-) \\ -\sin(\omega_- t - \phi_-) \end{bmatrix} + r_+(t) \begin{bmatrix} \cos(\omega_+ t - \phi_+) \\ -\sin(\omega_+ t - \phi_+) \end{bmatrix}. \tag{2.33}$$

As already mentioned, the dipolar excitation allows to modify single motions depending on the applied frequency. Therefore, by varying the external frequency one can excite different eigenfrequencies. For the resonance case the time-dependent radii can be approximated by [Bla+03a]

$$\lim_{\Delta\omega \to 0} r_\pm(t) = \sqrt{r_\pm^2(0) + \left(\frac{qV_d}{ma}\frac{t}{2(\omega_+ - \omega_-)}\right)^2 \mp \frac{r_\pm(0) qV_d \sin(\Delta\phi)}{(\omega_+ - \omega_-)} t}, \tag{2.34}$$

where $\Delta\omega = \omega_{rf} - \omega_\pm$ and $\Delta\phi = \phi_{rf} - \phi_\pm$. Previously, it was shown that the magnetron frequency is in first order mass independent. Thus, excitation on this frequency will affect all ions stored in the trap. This can be used to prepare all ions in the same state, i.e. excite all species to the same magnetron radius or even to remove them completely. Three scenarios for the phase difference can be distinguished:

- $\Delta\phi = 0$ - the magnetron radius (r_-) grows slowly at the beginning afterwards linearly with the excitation time.
- $\Delta\phi = \pi/2$ - in this scenario the dipolar excitation field is anti-parallel to the particle's motion. In the resonance case with the magnetron eigenfrequency the initial radius increases linearly with time from the very beginning of the excitation.
- $\Delta\phi = 3\pi/2$ - in this situation the dipolar excitation field is parallel to the particle's motion. When in resonance with the the magnetron motion the magnetron radius (r_-) decreases linearly with time to zero and afterwards grows linearly with the excitation time.

Figure 2.6: a) The final magnetron radius as a function of the duration of the dipolar-excitation pulse. Each curve corresponds to different phase between the rf excitation and the initial magnetron motion. b) The final magnetron radius as a function of the difference in phase between the rf excitation pulse and the initial magnetron motion for three values of the duration of the dipolar-excitation pulse [Bla+03a].

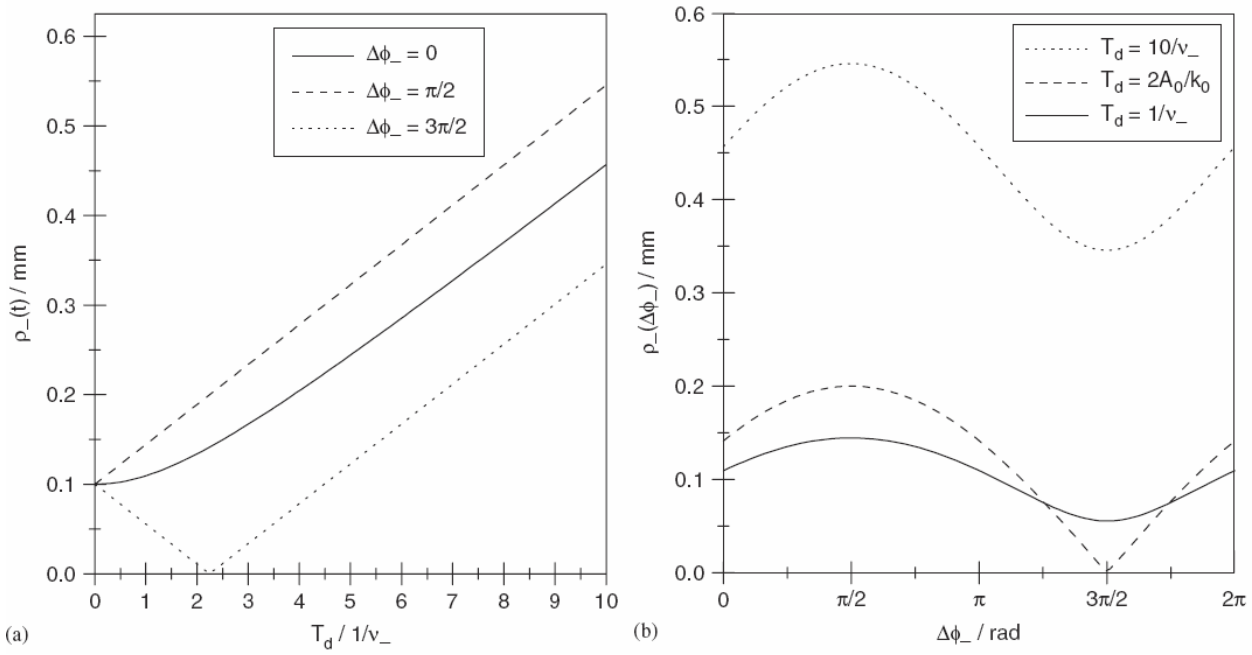

Quadrupole excitation

Another important type of excitation is the so-called quadrupole excitation, which is schematically presented in the right panel in Fig. 2.5. As explained above, it couples two different motions when applied at differences or sums of their frequencies. The azimuthal electric field has then the form:

$$\vec{E}_x = -\frac{2V_q}{a^2}\cos(\omega_{rf}t - \phi_{rf})y\vec{e}_x, \tag{2.35}$$

$$\vec{E}_y = -\frac{2V_q}{a^2}\cos(\omega_{rf}t - \phi_{rf})x\vec{e}_y \tag{2.36}$$

where V_q is the amplitude of the applied excitation at radius a. In the case of ISOLTRAP the excitation frequency ω_{rf} couples the modified cyclotron and the magnetron motion $(\omega_+ + \omega_-)$ producing periodical oscillations between the two motions [Kön+95]. The equation of motion in the radial plane then will become:

$$\ddot{\vec{u}} + i\omega_c\dot{\vec{u}} - \left(\frac{\omega_z^2}{2} - \frac{q}{m}\frac{V_q}{a^2}\cos(\omega_{rf}t + \phi_{rf})\right)\vec{u} = 0 \tag{2.37}$$

The solutions of this equation are given in [Kön+95; Yaz06]

$$r_\pm(t) = \left(r_\pm(0)\cos(\omega_b t) \mp \frac{1}{2}\frac{r_\pm(0)(i(\omega_{rf} - \omega_c) + r_\mp(0)k_{rf}^\pm}{\omega_b}\right)e^{i\frac{1}{2}(\omega_{rf}-\omega_c)t}, \tag{2.38}$$

where

$$\omega_b = \frac{1}{2}\sqrt{(\omega_c - \omega_{rf})^2 + k_{rf}^2},$$

and

$$k_{rf}^{\pm} = k_{rf} e^{\pm i\Delta\Theta}.$$

If the four-fold segmented ring electrode has an inner radius $r_0 = a$ then the amplitude of the external oscillating field V_{rf} will be in first order approximation equal to the amplitude of the azimuthal quadrupole field V_q.

The effect of the quadrupole excitation causes the initially pure magnetron motion with radius $r_{-,0}$ to completely convert to pure cyclotron motion with radius $r_+ = r_{-,0}$. The conversion period is given as

$$T_{conv} = \frac{M}{q}\frac{2a^2}{V_{rf}}(\omega_+ - \omega_-)\pi = \mathrm{B}\frac{2a^2}{V_{rf}}\frac{\omega_+ - \omega_-}{\omega_c}\pi. \tag{2.39}$$

It should be noted here that the conversion time is in first order mass independent and depends only on the magnetic field B and the driving oscillating amplitude.

2.2.3 Destructive Time-of-Flight Ion-Cyclotron-Resonance detection technique

The measurement of the cyclotron frequency ($2\pi\nu_c = \omega_c$) of a particle trapped in a Penning trap can be divided in two major categories, known as non-destructive and destructive detection techniques. The non-destructive method is the Fourier-transform ion-cyclotron resonance (FT-ICR) detection technique [CM74]. The destructive techniques recognised nowadays are called time-of-flight ion-cyclotron-resonance (TOF-ICR) and phase-imaging ion-cyclotron resonance (PI-ICR) detection [Eit+09].

The FT-ICR method is based on Fourier-transform ion-cyclotron resonance [MH02], where the stored particles induce an image-current on the trap electrodes while being stored. The induced current is in the order of a few fA for singly charged particle. The name non-destructive hence is given as the measurement can be repeated many times without losing the particles from the trap. Either a large sample of particles or a cryogenic environment are some of the requirements in order to overcome the thermal noise induced to the measurement electronics. When the lifetime of the particles of interest becomes too short the destructive ion-cyclotron resonance techniques are used, as the particles might be lost due to decay. The PI-ICR is a novel detection technique, developed just few year ago and primarily focused to improve the TOF-ICR by precisely monitoring the state of the particle's motion in the trap. The PI-ICR is currently being implemented at ISOLTRAP in order to enhance the performance of the spectrometer. In the following, the focus will be placed on the description of the TOF-ICR detection method. This technique was mainly used to determine the masses of the caesium and cadmium isotopes within this thesis work with the best precision possible.

The destructive time-of-flight ion-cyclotron resonance detection principle was first proposed by Bloch [Blo53] and afterwards applied for the first time to mass measurements by Gräff *et al.* [GKT80]. This technique has the advantage compared to FT-ICR in its sensitivity for single particles stored in the trap at room temperature. Clearly, if one would like to observe a resonance and determine the frequency of the cyclotron motion, the measurement has to be repeated multiple times. The final result is a resonance scan compiled from different driving frequencies around the true cyclotron frequency.

The TOF-ICR detection principle is based on the coupling of the magnetic moment $\vec{\mu}$ of the particles to the gradient of the magnetic field $\vec{\nabla}\vec{B}$ which they experience while drifting from the strong magnetic field towards a detector placed downstream the Penning trap. In this context, the cyclotron resonance is monitored via the change of the kinetic energy which accompanies a full conversion from pure magnetron to cyclotron motion. Usually, this means that at first particles are desired to have a finite magnetron radius (about 0.7 mm) so that they probe less of the trap imperfections (as seen from Fig. 2.19). Such preparation is achieved as was described in the previous subsection on dipolar excitation Sec. 2.2.2. For convenience at ISOLTRAP the dipole excitation at the magnetron frequency (ω_-) is applied to the opposite electrodes. The remaining two electrodes from the four-folded segmented ring are used for dipole excitation at the modified cyclotron frequency (ω_+). The latter is used to excite unwanted particles to cyclotron radius where they can be lost due to hitting the trap electrodes for example. This mechanism is called "*dipole cleaning*". With such fine purification typical mass resolving powers of 10^6 can routinely be achieved.

Prior to the particles ejection towards the detector, a quadrupolar excitation is applied (with frequency ν_{rf} and amplitude V_{rf}). The radial kinetic energy of the stored particles is given as:

$$E_r \propto \omega_+^2 r_+^2(t) + \omega_-^2 r_-^2(t) \approx \omega_+^2 r_+^2(t). \tag{2.40}$$

The energy transfer from pure magnetron to pure cyclotron motion can then be expressed to be frequency dependent. Given the correct amplitude, for the resonance case ($\omega_{rf} = \omega_+ + \omega_-$) the energy conversion will be maximum. In the more general case for excitation off-resonance ($\omega_{rf} \neq \omega_+ + \omega_-$), the conversion will not be complete and thus the radial kinetic energy compared to the resonance case would be smaller. If the particles now are ejected from the trap (Fig. 2.7), an additional force in the axial direction will be experienced due to the magnetic field gradient:

$$\vec{F} = -\vec{\mu} \cdot \vec{\nabla}\vec{B}. \tag{2.41}$$

The mean magnetic moment of the stored particles in the Penning trap can be expressed as:

$$\vec{\mu} = -\mu\vec{e}_z = -\frac{q}{2}(\omega_+ r_+^2 + \omega_- r_-^2)\vec{e}_z. \tag{2.42}$$

Figure 2.7: Principle of the time-of-flight cyclotron resonance detection technique. After sequence of dipole and quadrupole excitation in the trap, ions are ejected out of it and left to drift through a magnetic field gradient, which is qualitatively presented on top.

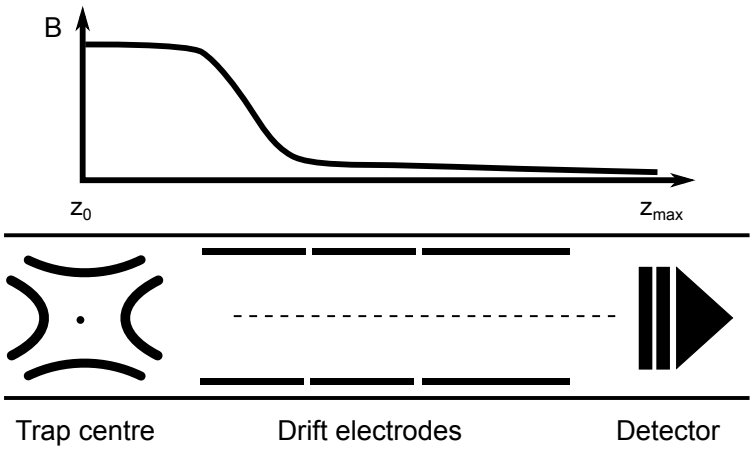

Furthermore, the energy due to the cyclotron motion ($E \approx E_r$) for particle with magnetic moment in the magnetic field can be described as:

$$\vec{\mu} = \frac{E_r}{\mathrm{B}}\vec{e}_z. \tag{2.43}$$

After substitution in Eq. (2.41) for the additional axial force one obtains the following relation:

$$\vec{F} = -\frac{E_r}{\mathrm{B}}\frac{\partial \mathrm{B}}{\partial z}\vec{e}_z. \tag{2.44}$$

If a rectangular excitation pattern is chosen then the radial kinetic energy can be derived by combination of Eq. (2.38) and Eq. (2.40) which leads to [Kön+95]:

$$E_r = \frac{\sin^2(\omega_b T_{conv})}{\omega_b^2}. \tag{2.45}$$

The total time of flight from the trap centre to the location of the detector can be calculated using the following equation:

$$T(\omega_b) = \int_{z_0}^{z_{max}} \sqrt{\frac{m}{2(E_0 - qV(z) - \mu(\omega_b)\mathrm{B}(z))}}dz, \tag{2.46}$$

with E_0 being the particles initial axial energy while stored in the trap; $V(z)$ and $\mathrm{B}(z)$ are the electric and magnetic fields along the ejection path. The principle is schematically presented in Fig. 2.7, while a typical time of flight spectrum is presented in Fig. 2.8.

Figure 2.8: Left: The typical Time-Of-Flight resonance (here $^{85}Rb^+$ with T_{rf} = 1200ms), the mean TOF is plotted versus the rf-excitation ν_{rf}. Right: The corresponding integrated spectrum shown with the faster (in-resonance) ions and the slower (off-resonance) ions. The so-called in-resonance ions (shown in the red area) have an excitation frequency ν_{rf} very close to ν_c. The naming in/off-resonance is just to illustrate the relation between the TOF and the rf-excitation frequency ν_{rf}.

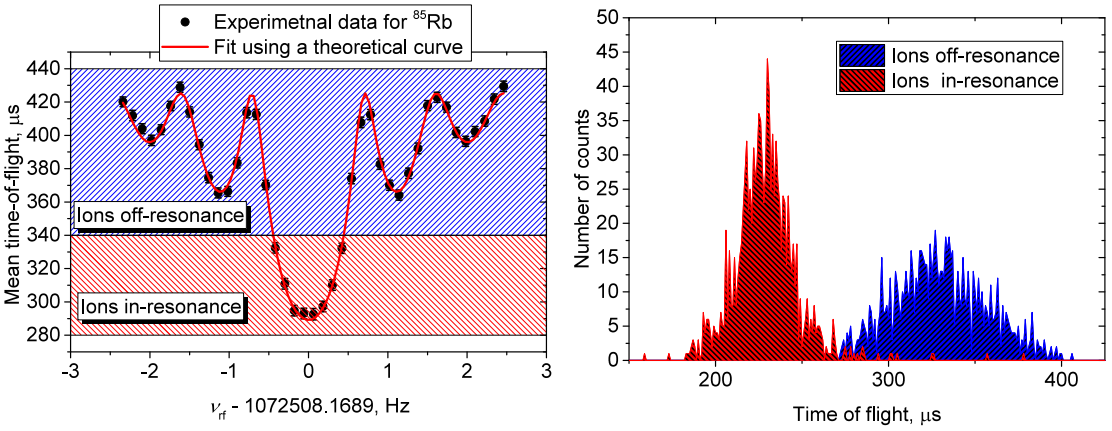

Ramsey-type excitation in TOF-ICR

The Ramsey-type excitation is an alternative scheme that can be applied instead of the single rf pulse that couples the magnetron and cyclotron ion motions. Its based on the novel technique invented by N. Ramsey [Ram90] back in 1949 for separated oscillatory fields in a molecular beam

experiments. In 1992, Bollen *et* al. [Bol+92b] suggested to use the Ramsey method to improve the accuracy of mass determination of radioactive nuclides by means of Penning-trap mass spectrometers. In essence the authors showed successful application of more than one rf-pulse applied to the trapped ions by keeping the phase of the external oscillating field during the nth excitation fixed with respect to the first one. As a result in the obtained time-of-flight spectrum, Ramsey fringes were observed, see Fig. 2.9. In spite the initial success of these measurements, the first on-line experiments for short-lived ions applying this excitation pattern, were only performed in 2007 by George *et* al. [Geo+07]. These were delayed in order to derive more elaborate theoretical analysis [Kre07] and consecutively include damping effects [Kre08]. The accuracy of the TOF-ICR measurement is determined by the width and shape of the resonance line. To compare with the conventional technique an improvement in precision by a factor of 3 is obtained and reduction in measurement time by a factor of 10 [Geo+08].

Figure 2.9: A TOF-ICR spectrum of $^{133}Cs^{+}$ by using a two pulse Ramsey excitation scheme. The duration of the rf-excitation was set to 100 ms while the waiting time between the two pulses was 1000 ms.

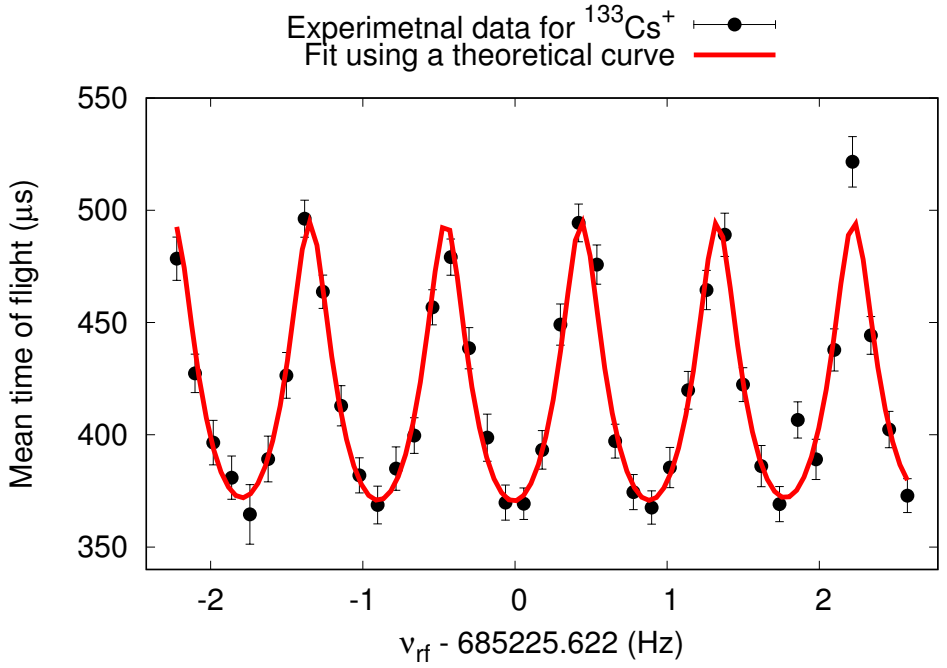

2.3 Multi-reflection time-of-flight mass spectrometry

Recently at the ISOLTRAP experiment the so-called multi-reflection time-of-flight mass spectrometry (MR-TOF MS) was employed [Wie+13]. While initially the MR-TOF device was introduced to purify the ions of interest from contaminants [Wol+13], it was quickly realised that it can be used as a mass-measurement tool as well. In the following section the theoretical concept for this type of mutli-reflection devices will be presented. Simple schematics is presented in Fig. 2.10 where two sets of ion-mirrors are confining the charged particles axially.

Figure 2.10: Simplified drawing of the axial electric potential, which is applied on the mirror electrodes of the multi-reflection time-of-flight device to create a trapping region.

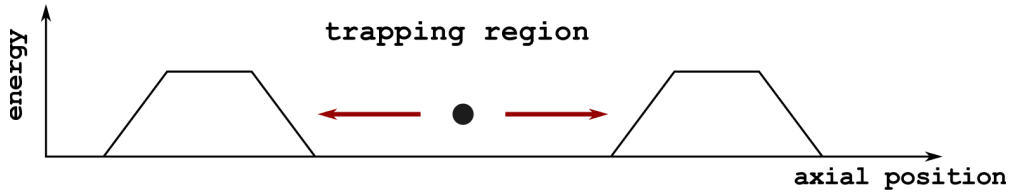

2.4 Developments in multi-reflection ion-traps

The time-of-flight mass spectrometry (TOF MS) was first introduced back in 1946 by Stephens who applied the simple idea of a linear flight path to charged particles [RFD15]. The main principle behind it is that particles with different mass-over-charge ratio will disperse in space after acceleration in an electric field since they will acquire different velocities. However, following developments throughout the next 40 years in the field a high resolving power was achieved by improving the design of the TOF spectrometers, for example by adding few more mirror electrodes. In comparison with today's spectrometers of *multi-turn* and *multi-reflection* types, delivering sufficient mass separation with resolving powers in the order of $10^5 - 10^6$, the instruments from the early years could achieve only values around 50. For further historical overview of the multi-turn and the multi-reflection TOF MS devices see [Wol13]. Currently the TOF MS is still behind the relative mass precision achieved by using static magnetic fields, like in Penning-trap mass spectrometry, but it showed its great advantage to perform fast measurements of short-lived species [Wie+13].

2.4.1 Basic principle

The operation of the MR-TOF MS as an ion-trap is based on the principle of capturing the charged particles in the volume of a static electric potential well. Such potential well can be produced by two ion-optical mirrors (as shown in Fig. 2.10) creating an electric potential barrier $qU(z)$, with q being the charge of the trapped particle and $U(z)$ the electric potential as a function of the position along the z-axis. If the kinetic energy of the particles is less than the barrier height they are confined axially and travel back and forth between the two ion-mirrors, while several focusing elements integrated in the mirrors confine them transversely [Wol+12b]. Such configuration can be viewed as a constant energy (E) acceleration from a well defined potential $E = qU$, giving for the kinetic energy:

$$\frac{1}{2}Mv^2 = qU, \tag{2.47}$$

where M, and v are the particle's mass and velocity, q is the charge of the particle in units of the elementary charge (e). The time of flight for a length L can then be expressed as:

$$t = \frac{L}{v} = \left(\frac{M}{q}\frac{L^2}{2U}\right)^{1/2}. \tag{2.48}$$

Here the time of flight of the particle is proportional to the square root of the mass-over-charge ratio. This relation is very important and will be used later in the analysis. The capability of a TOF MS is expressed as the ability of a device to discriminate between particles with different mass-over-charge ratios. Thus, the time dispersion Δt of the system resolving two particles with

difference in mass ΔM is given as:

$$\Delta t = \frac{L}{\sqrt{2U}}\left[\left(\frac{M+\Delta M}{q}\right)^{1/2} - \left(\frac{M}{q}\right)^{1/2}\right]. \tag{2.49}$$

Consequently the mass resolving power can be determined by the time dispersion of the peaks:

$$R = \frac{M}{\Delta M} = \frac{t}{2\Delta t}. \tag{2.50}$$

Thus, high mass resolving power can be achieved by increasing the flight path of the particles or by decreasing the individual signal width. Extending the flight path has been first demonstrated by Wollnik [WP90]. He improved the design of the TOF MS by folding the flight path into one device by forcing the particles to travel multiple times between two ion mirrors arranged in a configuration anti-parallel to the direction of flight. However, successful application for high-resolution mass spectrometry was only shown a few years ago. In this case of individual flight times of the particles are given as $T_i \propto \sqrt{M_i/q_i}$ according to Eq. (2.48). The separation in time of two particles with indexes i and j will be linearly dependent on the number of revolutions n spend in the TOF device:

$$\Delta T_{ij} = n|T_i - T_j|. \tag{2.51}$$

As a result, the mass separation of different particles can be expressed through the number of revolutions spent in the device and by adjusting/focusing the individual time spread in the detector plane.

The first step in the mass measurements with the MR-TOF MS device are performed by obtaining a calibration by using the times of flight $t_{1,2}$ of two particles with well-known masses $m_{1,2}$, respectively. A system of three equations can then be written as:

$$\begin{aligned} T_1 &= a \cdot \sqrt{M_1/q_1} + b \\ T_2 &= a \cdot \sqrt{M_2/q_2} + b \\ T_x &= a \cdot \sqrt{M_x/q_x} + b, \end{aligned} \tag{2.52}$$

where T_x is the measured total time-of-flight of particle with mass-over-charge ratio M_x/q_x. Here the constants a and b are specific for the measurement device. From the first two equations an expression for the two constants in terms of time-of-flight and mass-over-charge ratio can be obtained:

$$a = \frac{T_2 - T_1}{\sqrt{M_2/q_2} - \sqrt{M_1/q_1}} \tag{2.53}$$

$$b = T_1 - \frac{T_2 - T_1}{\sqrt{M_2/q_2} - \sqrt{M_1/q_1}} \cdot \sqrt{M_1/q_1}. \tag{2.54}$$

Its clear from Eq. (2.53) that the constant a is linearly dependent on the total flight time which on the other hand is directly connected with the number of revolutions performed by the stored particles. By substituting the two constants in Eq. (2.52) and reshuffling the terms one obtains an expression for the unknown mass:

$$\sqrt{\frac{M_x}{q_x}} = \left(\frac{2T_x - T_1 - T_2}{2(T_1 - T_2)}\right)\left(\sqrt{\frac{M_2}{q_2}} - \sqrt{\frac{M_1}{q_1}}\right) + \frac{1}{2}\left(\sqrt{\frac{M_1}{q_1}} + \sqrt{\frac{M_2}{q_1}}\right). \tag{2.55}$$

This expression is the central equation used for the determination of unknown masses by the MR-TOF MS technique at ISOLTRAP.

Chapter 3

Experimental setup

Prerequisite for precision mass measurements of short-lived isotopes is their production in sufficient quantities. Different nuclear reactions and target/projectile combinations, for instance fission, spallation, projectile fragmentation, fusion and transfer reactions, are employed to optimise the production of rare nuclides of interest [BLS08]. Unfortunately, in all these methods not only the specific species of interest are produced, but also a wide variety of other nuclides, which act as contamination complicating the measurements. Two main complementary separation techniques were developed, namely the Isotope Separation On-Line (ISOL) and "in-flight" separation methods. The latter one employs fast projectile and relatively thin targets, such that the reaction products emerge from the target with energies close to those of the projectile. Kinematic focusing in the forward direction is used to collect and separate "in-flight" the swift secondary beams. The advantages of this method are the quick separation (in the order of μs) and the "chemical blindness", i.e. the production of radioactive ions regardless of their atomic and chemical properties. However, the produced secondary beam has a large emittance due to the nuclear reaction process [FGM08]. Furthermore, in order to store such fast particles in a trap they have to be slowed down from several hundreds of MeV/u to a few keV/u. Examples of traps at in-flight separation facilities are HITRAP [Her+15], SHIPTRAP [Blo15] at GSI, Darmstadt and LEBIT at the NCSL at MSU [Rin+06]. The "in-flight" separation technique is successfully applied at GSI, Darmstadt, RIKEN in Japan and NSCL/MSU in the United States [Ben+00] and is planned in the second-generation radioactive ion-beam facilities RIBF, FRIB, FAIR [BND13].

An introduction to the ISOLDE facility and the ISOL production and separation mechanism will be given, followed by a description of the experimental apparatus ISOLTRAP, that was used for the measurements described in this work.

3.1 The Isotope Separation On-Line at ISOLDE

The basic principle behind the production of very exotic (neutron-rich or neutron-deficient) nuclei at ISOL-type facilities is a thick target (up to a few 100 g/cm^2) material bombarded by highly energetic protons or light ion beams (beam energies can be in the range of 100 - 2000 MeV/u). Various nuclides are then produced via proton induced spallation and/or fission. By interactions with the surrounding target material, the reaction products are neutralised and thermalised in the target volume. Due to the heat applied on the target container (between 1000 - 2000 K) the

newly created radioactive isotopes are evaporated and – after a diffusion process through a transfer line – they enter into an ion source. After ionisation, the ions are extracted and accelerated by electric fields to energies of up to a few tens of keV. The ISOLTRAP experiment is situated at

Figure 3.1: Schematic representation of the ISOLDE experimental hall. A proton beam from PSB/CERN with energy of 1.4 GeV is impinged on a tick target material, in our case an UCx. Following the ionisation and extraction from an ion source, the ion-beam is accelerated and separated either by GPS or by HRS mass separators. Then, the selected species are transferred to the experimental setup, ISOLTRAP, located at the end of the central beam line. Only parts of the facility relevant for the experiments done at ISOLTRAP are labelled.

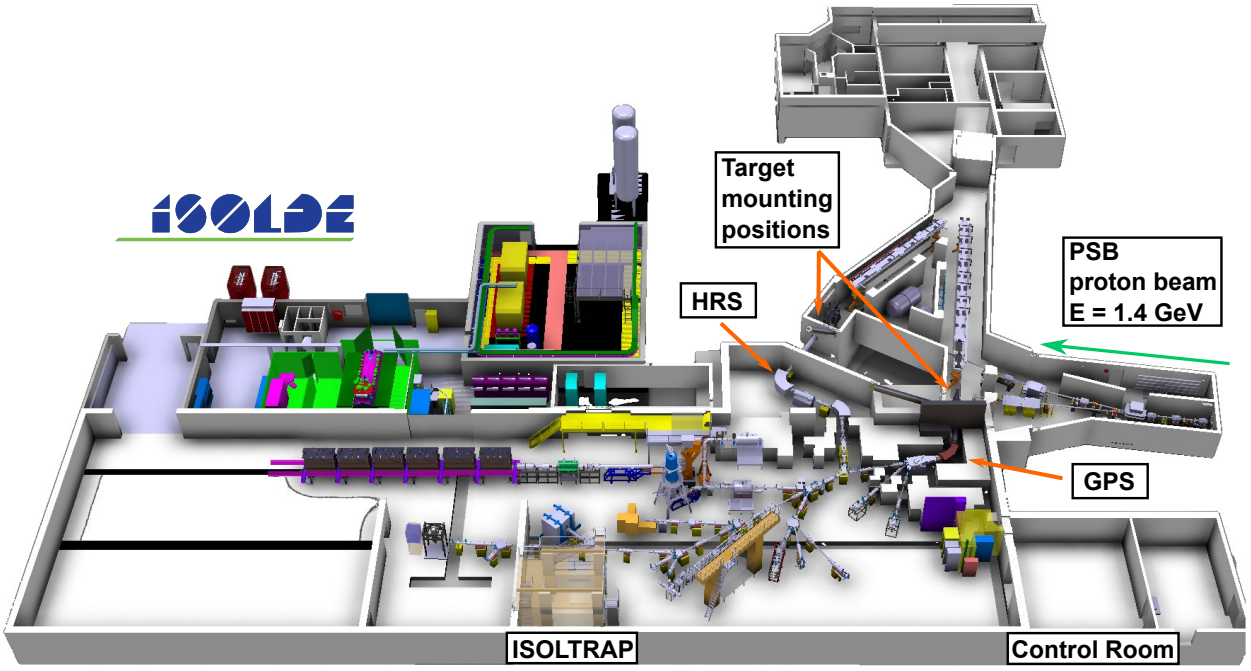

the ISOLDE facility (shown in Fig. 3.1) located within the European Particle Physics Laboratory CERN in Geneva, Switzerland [Kug00]. As the name of the facility suggests, the ISOL mechanism is used for production of exotic nuclides. A pulsed proton beam is currently delivered by CERN's Proton-Synchrotron Booster as a primary beam. The currently used characteristic of the proton beam are a kinetic energy of 1.4 GeV and an average intensity of up to 2 μA. More then 1200 radioactive nuclides are available after the bombardment of various primary targets. Depending on the demands of the specific experiments, different layouts of the target material and container are used. For the specific cases, discussed within this work, the chosen target material was an uranium-carbide (UCx). As an alternative to the usual target design a tungsten rod was added [Kös02]. A photograph of the target highlighting the main components is shown in Fig. 3.2. The proton beam is steered towards the tungsten rod which acts as a source of thermal neutrons (or in other words neutron converter). The thermal neutrons induce uranium fission in the target material. In this way a reduction of more abundant stable spallation products produced by the direct impact of the proton beam can be achieved.

The production rate in such configuration depends on the primary beam intensity, the target thickness and, finally, on the reaction cross section. However, the intensity of the extracted ion beam will in addition be dependent on the efficiency of the diffusion and ionisation. In the particular case of short-lived radioactive isotopes, the time required for all these processes is the main limit.

Thus, the chemical properties and the half-lives are crucial factors in the production and extraction mechanisms of the radioactive species.

Figure 3.2: The target unit used within the cadmium experimental campaign. (1) Tungsten rod acting as neutron converter, (2) target container, (3) cooling block of the quartz transfer line. *Picture credits: Bernard Crepieux*

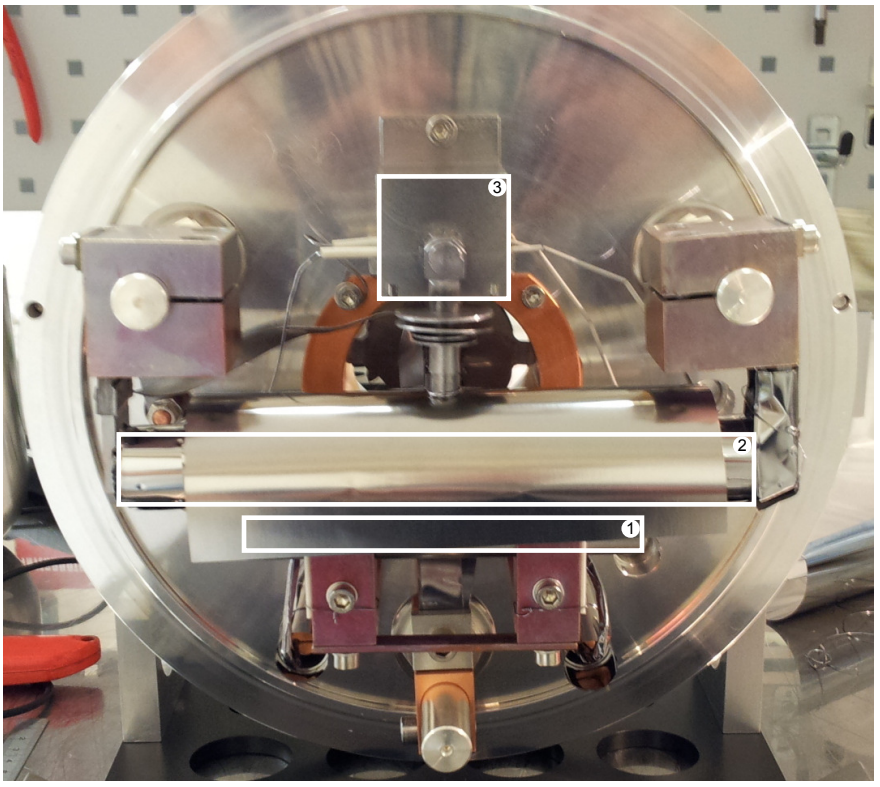

Three techniques are widely used for the production of singly charged ion-beams at ISOLDE.

- Surface ionisation - ions can be created by surface ionisation when they contact the heated walls of the ion-source cavity. The production efficiency of this technique depends on the work function of the specific element. For example, alkali metals have low work function and are easily extracted as singly charged ions. However, such a method is chemically non-selective as the only variable is the temperature that can be applied on the walls of the ion source.

- RILIS [Mar+13] - ions are be created through resonant laser excitation within the volume of the ion-source. In this ionisation mechanism several laser beams are overlaid with the diffusing radioactive atoms coming out of the target into the volume of the ion source. The laser light kicks out an electron from the atomic shell into the continuum by using multi-step transitions. Hence, the resonant excitation is highly selective since the atomic energy transitions vary with the chemical elements and even within one isotopic chain.

- Plasma - creating ions from plasma is the third technique available at ISOLDE. This production scheme is mostly used for gases or in the cases for which the first two methods have poor efficiency. This is a non-selective method but it can produce high currents for specific isotopes and even ions in highly-charged states.

Whenever RILIS or plasma ionisations are in use, the ion-source walls are heated for fast release, which can still enable surface ionisation. Therefore, usually ion beams delivered to the experiments contain surface-ionised elements. These act as contamination and can frequently disturb the obtained experimental data. This effect is easily reduced by carefully choosing the material from which the ion source is manufactured. Another way of dealing with the surface-ionised contamination is the introduction of cold quartz into the transfer line. In this way certain species are trapped or their movement towards the ion source delayed. The latter, when used in cooperation with RILIS ionisation, showed the production of higher-purity beams [Bou+08; Bou+07]. Further developments are ongoing, like, e.g. the construction of the so-called Laser Ion Source Trap (LIST), which aim will be to repel the surface-ionised contamination prior to performing the laser ionisation [Bla+03b; Fin+13].

The front-end unit, containing the target container and the ion source, is floated to high-voltage potential, usually between 30 and 60 kV. Singly-charged ions are extracted and accelerated (kinetic energy corresponds to the potential at which the unit is set) and transported through one of the two available electro-magnetic separators at ISOLDE - the general purpose separator (GPS) or the high-resolution separator (HRS) with mass resolving power of $m/\Delta m = 1000$ and 5000 [Gil+03], respectively, see Fig. 3.1. Using the separator's magnets specific isobars can be selected out of the whole available set of species created in the ion source. The mass resolving power of the HRS separator can partially be enhanced by introducing movable mechanical slits in order to select a narrow part of the ion-beam.

The resulting beam intensity I_{RIB} can be described by the following equation [Rav79; Kös01]:

$$I_{RIB} = (\sigma_{prod} \cdot N_{tar} \cdot I_p) \cdot \epsilon_r \cdot \epsilon_{ion} \cdot \epsilon_{pa}, \tag{3.1}$$

where σ_{prod} is the production cross section specific for the elements created by interaction of primary proton beam with intensity I_p on a target material with thickness N_{tar}. For a realistic yield estimation of the extracted beam the efficiency for the release ϵ_r, ionisation ϵ_{ion} and post-acceleration ϵ_{pa} have to be considered. It is obvious, that by careful choosing the target-ion-source combination a variety of very exotic and short-lived nuclides can be produced, as for instance, the neutron-rich ^{131}Cd. An example of nuclides produced from the UCx target equipped with a neutron converter, is visualised in Fig. 3.3.

3.2 The ISOLTRAP mass spectrometer

The ISOLTRAP experiment is mainly dedicated to precision mass measurements of short-lived isotopes with characteristic lifetimes of the investigated species reaching down to milliseconds [Muk+08; Wol+12a; Kre+13]. Currently the experimental setup is composed of four main devices: a linear segmented radiofrequency cooler and buncher, a multi-reflection time-of-flight mass separator, a preparation Penning trap and a precision Penning trap. In the following a detailed description of each device will be given. The full setup is shown in Fig. 3.4 as well as some additional ion-optical elements used for beam transport and manipulation. For ion detection, several multi-channel plate detectors are installed along the beam line. Prior to the high-precision mass measurements, the ISOLDE beam needs to be decelerated from its initial energy (up to 60 keV) down to a few electron volts. Such action inevitably leads to an increase in the beam emittance, which before injecting the ions into the precision Penning trap, should be decreased or in other words the beam should be cooled.

Figure 3.3: Simulation for the ISOLDE production yields from a UCx target and impinging proton beam with energy of 1.4 GeV. *Simulation and picture credits: Alexander Gottberg and Frank Wienholtz.*

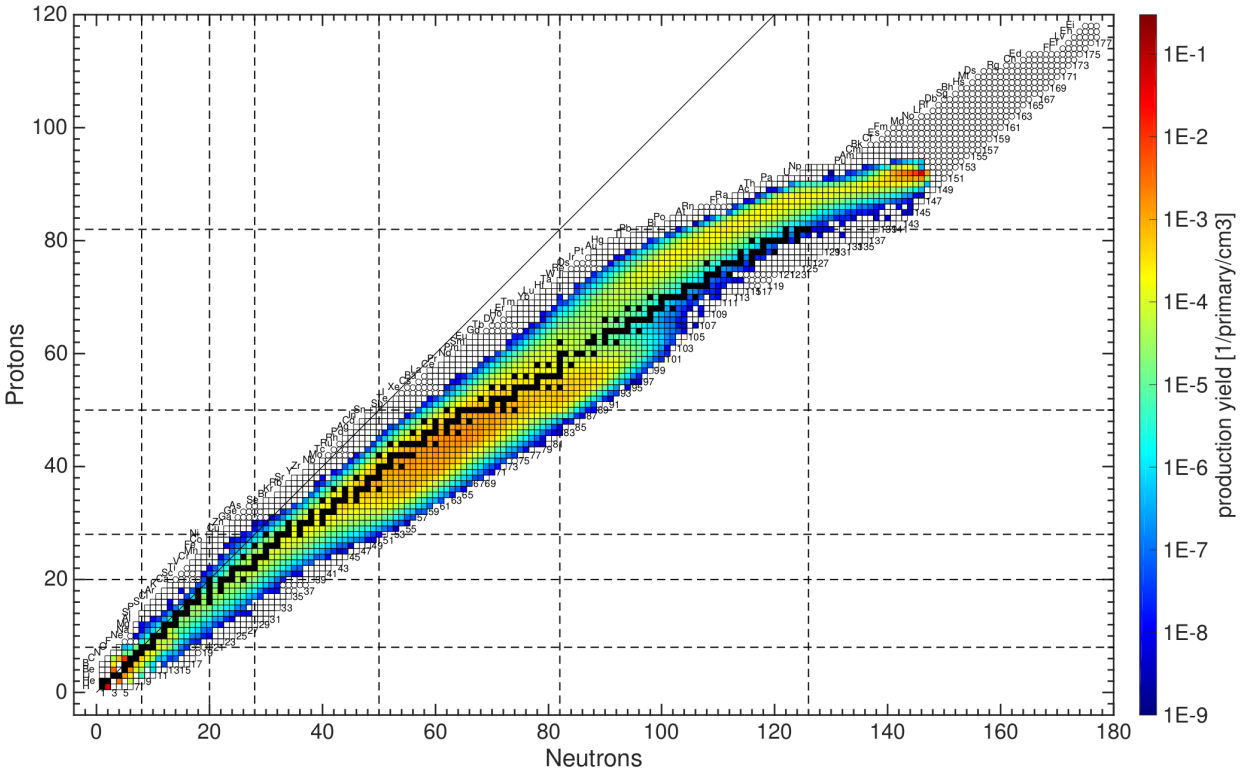

3.2.1 Offline reference ion source

For offline tests, commissioning and calibration purposes a dedicated ion-source is installed at the experimental setup [Kre+13], see Fig. 3.4. Normally, the ion-source employs a surface-ionisation, which is able to deliver sufficient quantities of stable alkali ^{39}K, ^{85,87}Rb, ^{133}Cs ions. Positively charged ions are produced by heating a commercial pellet (Heat Wave) to temperature of about 1000 degrees Celsius. Ions are extracted and focused using a set of steering and lens electrodes. Voltages are then applied on a kicker and bender electrodes injecting part of the beam into the radiofrequency cooler and buncher.

Having access to nuclides with well-known masses is used during a none running periods to test the ISOLTRAP system and more particularly to investigate systematic and statistical deviations [Bec+08]. For example the mass of ^{85}Rb is measured using as a reference to the mass of ^{133}Cs (see below for the description of the measurements and Fig. 4.3 for an example of the results). Another useful application of having a reference ion source is the ability to perform transport optimisation of ions between the beginning of the setup until the last measurement detector. This task is carried out once before the actual measurements begin in order to minimise the losses due to not optimal injection into the trap or bad transport throughout the experimental system. Most commonly, due to temperature drifts in the power supplies, voltages applied to transport elements can vary and steer the beam to a trajectory, where it can collide with the walls of the surrounding vacuum chamber and be lost.

Figure 3.4: Schematic drawing of the ISOLTRAP setup. The main components of the experimental setup, like trap devices, deceleration cavities, detectors etc., are presented. For details see text.

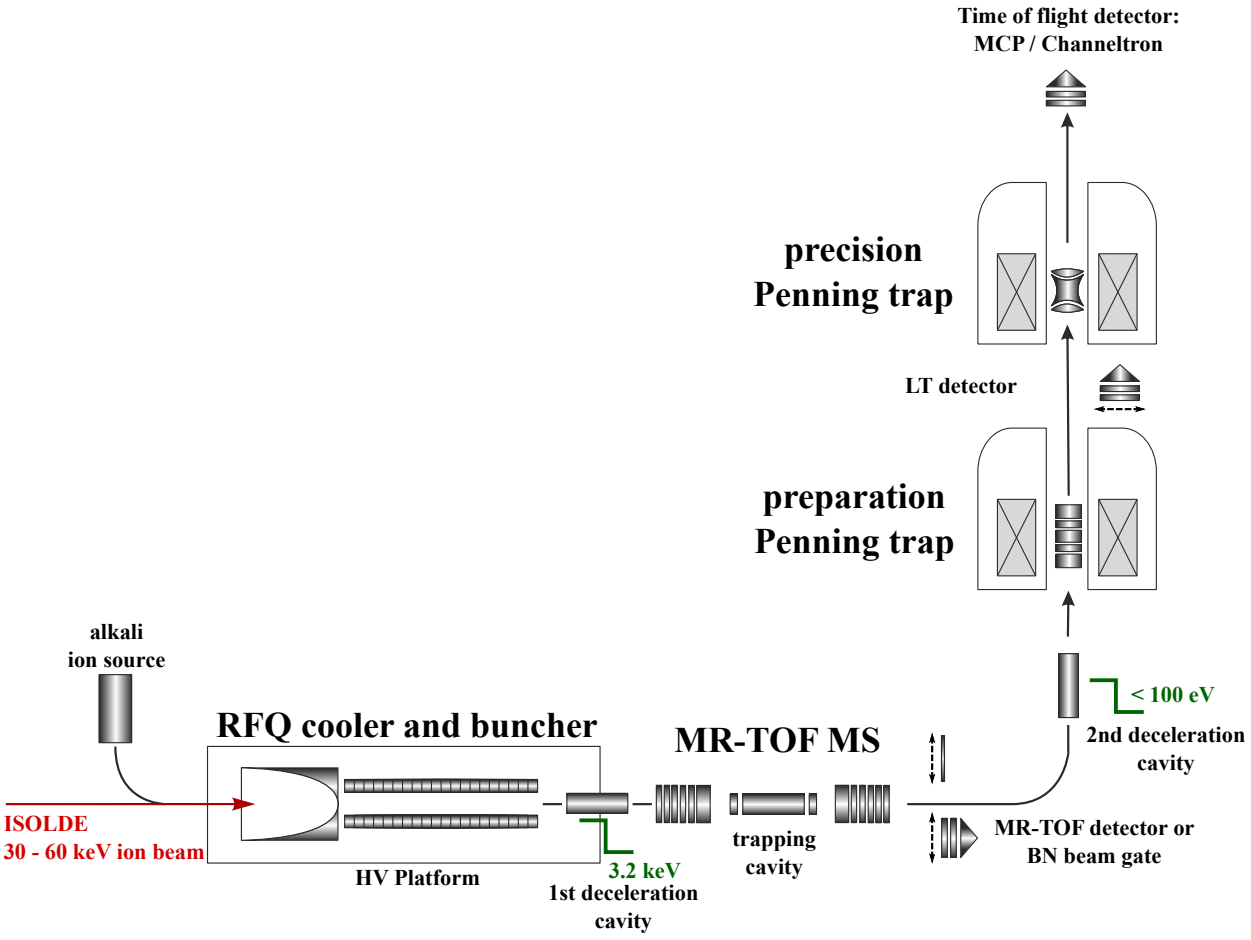

3.2.2 Radiofrequency quadrupole buncher

The radiofrequency quadrupole cooler and buncher (RFQ) [Her+01; Her+03] installed at the ISOLTRAP experiment is a linear gas-filled Paul trap consisting of four rods in a quadrupole configuration. Each rod is 26-fold segmented with the main purpose to superimpose an axial DC potential to a radially applied radio-frequency (RF) potential.

The entire RFQ setup with all of its components and electronics is placed inside a high-voltage cage allowing the device to be used at the potential of the ISOLDE beam. Once the ISOLDE beam approaches the RFQ, it is focused and decelerated down to a few hundreds electron volts by an egg-shaped electrode, but still having enough energy to enter the trap. The beam is then trapped radially by the radio-frequency field and axially by potential well, created by using the DC potential applied to different segments of the rods.

The ion-beam is constantly cooled in a helium buffer-gas environment and as a consequence loses some of its kinetic energy by multiple collisions with He atoms. Nominal pressure of about 10^2 Pa of the helium buffer-gas is routinely used in the setup during measurements. Finally through cooling and radial confinement through the RF field, it is possible to achieve transverse emittance of the beam of $\epsilon_{trans} \approx 10\ \pi$ mm mrad and longitudinal emittance of $\epsilon_{long} \approx 10$ eVμs. After

sufficient accumulation of about several tens of milliseconds (the duration of the accumulation and cooling depends on the investigated species), the last segments are switched from configuration with a trapping potential to one with an extraction potential, allowing the ion-bunch to be ejected towards the rest of the experimental setup. A pulsed drift tube is placed after the cooler-buncher and floated to a potential lower by 3.2 kV as compared to the rest of the HV platform. Whenever the bunch is at the centre of the drift tube the whole drift tube is switched to ground potential leaving the ions at energy of 3.2 keV.

Figure 3.5: A sketch and a photograph of the linear segmented radiofrequency quadrupole trap at ISOLTRAP. The trap electrodes are made of stainless steel with insulators out of glass ceramic (Macor). The main purpose of this device is the accumulation, cooling and bunching of the ISOLDE beam. The size of the inner scale in the photograph is 10 cm.

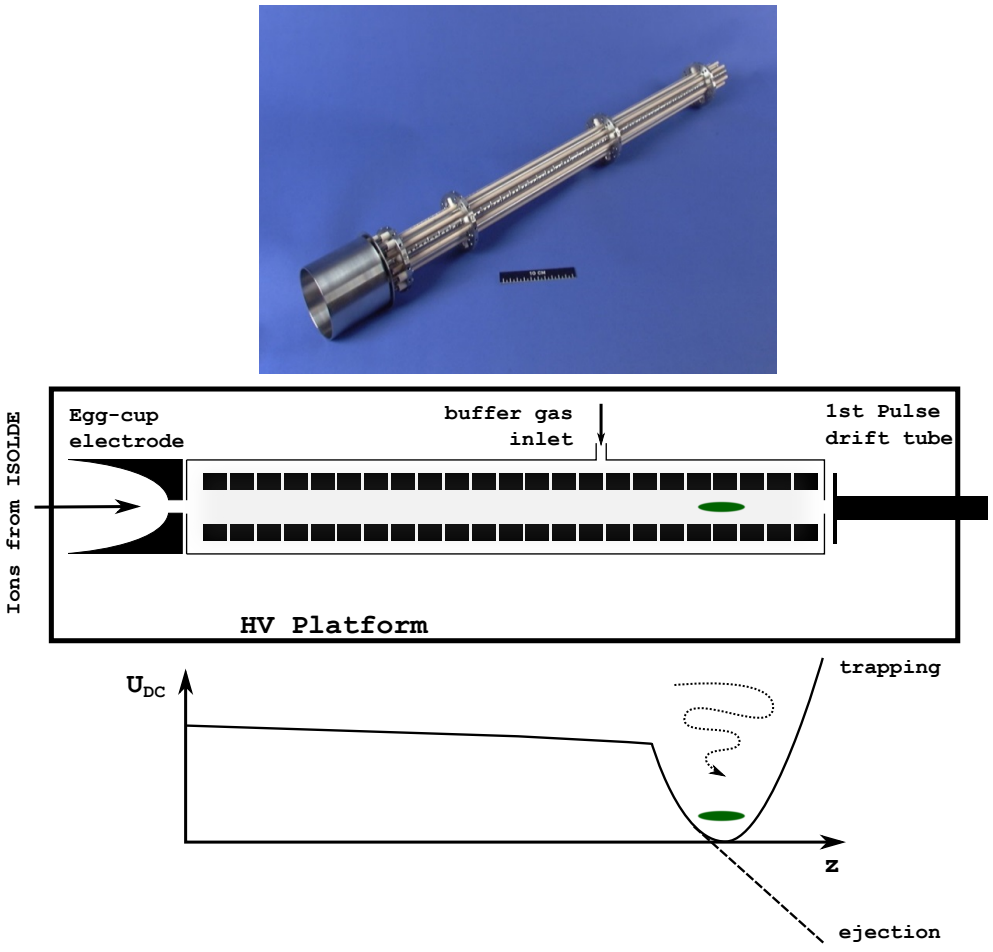

3.2.3 Multi-Reflection Time-of-Flight mass separator

After the ion-bunch is ejected from the RFQ, it is transported to the multi-reflection time-of-flight mass separator (MR-TOF). The device comprises two sets of electrostatic mirrors with a drift tube located in the centre between the two mirrors, presented in Fig. 3.6. Initially installed at ISOLTRAP in 2010 [Wol+12a], the MR-TOF had as the main purpose the purification of the ion-bunch from unwanted isobaric contamination. The cleaning procedure is always performed prior to the injection of the ion-beam into the tandem Penning-trap system. Generally speaking, the

Figure 3.6: The multi-reflection time-of-flight mass spectrometer. The main components of the device are presented - on the left and right the two sets of mirror electrodes and in the middle the field free drift tube. *Picture credits: Robert N. Wolf*

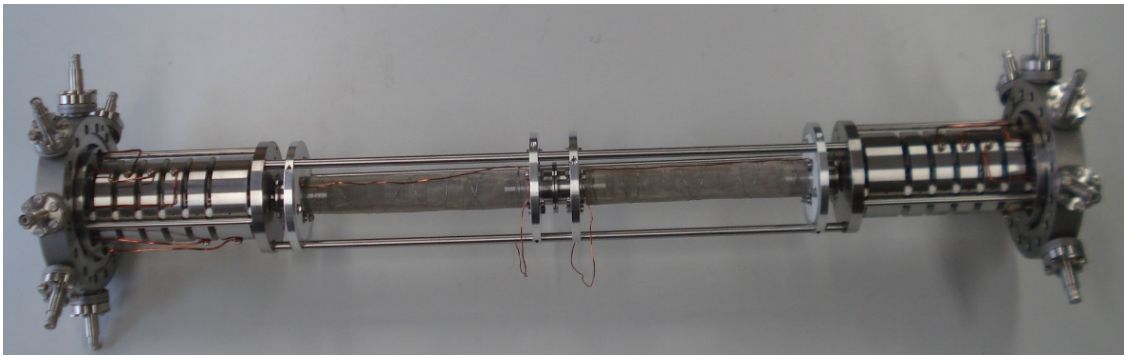

separation of the bunch to its individual components relies on their mass difference. The ion-bunch is trapped between two sets of electrostatic mirrors by using the in-trap lift technique [Wol+12b]. The ions perform multiple oscillations between the mirrors and each oscillation increasing their flight path. Isobars having the same velocity but different masses will separate in time of flight. Species with heavier masses will tend to slow down and thus, separate in time of flight from their lighter companions. With every oscillation the overall flight path increases and therefore the separation as well [Wol+12a].

The final mass resolving power strongly depends on the velocity spread of the ions which is directly translated into the width of the time-of-flight distribution, Δt. It was shown that resolving powers 2.50 in the order of 10^5 can be achieved in only few tens of milliseconds [Wol+12b].

At the exit of the MR-TOF MS device one can place a counting detector, such as multi-channel plate (MCP) detector or an electron multiplier (EM), or a beam gate selector (Bradbury-Nielsen beam gate BNG [BN36] in this case). The detector is used to measure flight times of each individual isobar, composing the initially injected ion-bunch. The BNG selector consists of multiple equally-spaced parallel wires winded on a metal frame. The spacing between each two wires is 0.5 mm. By applying voltage with equal value but opposite polarity to neighbouring wires, ions are deflected and thus not transmitted to the rest of the setup (gate in closed state). When ions of interest arrive at the BNG, by switching the voltages to zero, they are allowed to pass through the gate unaffected (gate in open state). By using fast switching between the two states of the BNG, one could select ions in a very specific and narrow time-of-flight window. For singly charged ions with $A = 100$ u and energy of 3 keV the time resolution is $\tau_{res} \approx 13$ ns. This switching technique allows transmitting only the ions of interest to the rest of the setup enhancing the overall performance of the following tandem Penning-traps system. By using the MR-TOF MS in combination with BNG, a suppression of isobaric contamination by a factor of 10^4 was shown to be achievable. An example of the time-of-flight spectrum is presented in Fig. 3.7.

Mass separation

Nowadays, the MR-TOF device offers a wide range of applications in addition to the one described above - the beam purification used in the precision mass measurement program at ISOLTRAP. As discussed in Sec. 2.3, the information obtained via time of flight (ToF) can be used to perform mass measurement studies. By using ions with well-known masses each ToF spectrum can be calibrated

and converted to a mass spectrum. This was demonstrated for the first time at ISOLTRAP with the measurements of neutron-rich calcium isotopes (reaching the mass number of $A = 54$) [Wie+13]. In that experiment the low production yield as well as the short half-lives of ^{53,54}Ca in combination with the hugely abundant contamination (predominantly ^{53,54}Cr isotopes), made impossible the usage of the traditional Penning-trap technique. The obtained relative mass uncertainty was below 10^{-6} presenting the MR-TOF MS as a possible technique for such challenging mass measurements. The MR-TOF MS of ISOLTRAP has played a decisive role to the success of the experiment determining the mass of ^{82}Zn, through its outstanding isobaric purification and suppression on time scale which is an order of magnitude faster than conventional methods [Wol+13].

Ion-beam analysis

The MR-TOF device was employed as a diagnostic tool in the process of the target and ion-source parameter optimisation relevant for the radioactive-ion production [Sto13]. This activity investigated the production cross section, effusion and diffusion behaviour, as well as the ionisation efficiency. Currently all the relevant parameters can be assessed in the time periods when the ISOLDE targets are irradiated by proton beam. Faraday cup devices are employed to monitor the changes in the production yield with respect to the temperature at which the target material is heated. However, the sensitivity of this approach is not high and is thus applicable mainly to stable ions. The identification of the radioactive species is performed via much more sensitive beta- and gamma-decay spectroscopy. All these techniques have their limits, either by the measurable ion count rate of the order of one pA, or by the branching ratio of the respective decays and the half-life of the ion of interest as well as by the background and detection efficiency [Kre+13].

An example of the study of the ISOLDE beam composition in the rare-earth region is presented in Fig. 3.7. It was taken during an experiment on cancer treatment collection. The program of this experiment is focused on nuclides with mass number $A = 149$ and in particular Tb, which is a promising candidate for cancer therapy [Mül+12].

After the mass separation one can obtain the time of flight of the species in the ISOLDE beam. The identification of the species in the online spectrum can be done in three ways:

- First by using the offline calibration with K, Rb or Cs ions at known trapping times.
- Second way is to use an abundant and resolved specie within the online spectrum, for instant the Dy^+ in Fig. 3.7.
- The third choice is by using the mass determination via the precision Penning trap.

Once the calibration is complete, each individual ToF peak can be assigned to a different ion or molecule. The changes in the yields of different species can then be monitored online and consequently optimised by varying target and ion-source parameters, such as target and transfer line temperatures, delay from the proton impact time prior opening the ISOLDE beam gate, or position of the separator slits. An example of the delay from the proton impact is given in Fig. 3.8. This way the release from the target for a given element produced at the proton impact ($t = 0$) can be sampled.

In general, estimates for the absolute production yields can be given using this method. However, the ISOLDE yield represents the ion-beam composition delivered and folded by half-life, charge-exchange loss and/or molecular break-up happening in the buffer-gas collision process during the

accumulation time in the cooler and buncher. To derive the absolute yield, the efficiency of the ISOLTRAP setup up to the MR-TOF device is first calibrated via the signal from the known intensity of a reference beam. Typical efficiency of the setup lies in the order of one to a few percent. The advantages of ion-beam yield analysis using the MR-TOF MS constitute the measurement time on the order of 10 ms, direct ion detection, non-scanning operation, resolving power in the order of 10^5, and no dependence on the ion decay properties. The procedure for the optimisation of the target and ion-source parameters could be directly performed on the investigated isobars. The latter played crucial role, since the production of the most exotic species investigated in this experiment was tiny [Kre+13].

Figure 3.7: An example of time-of-flight spectra for mass $A = 160$ isobars coming from ISOLDE. The spectrum is centred on the stable dysprosium ions, while the study was focused on the radioactive ytterbium. After performing Penning-trap mass spectrometry, all other constituents in these spectra can be identified by the difference in their time of flight with respect to the ytterbium peak. The dashed lines indicate the expected positions of the mono-atomic and diatomic-oxide contaminants in the beam.

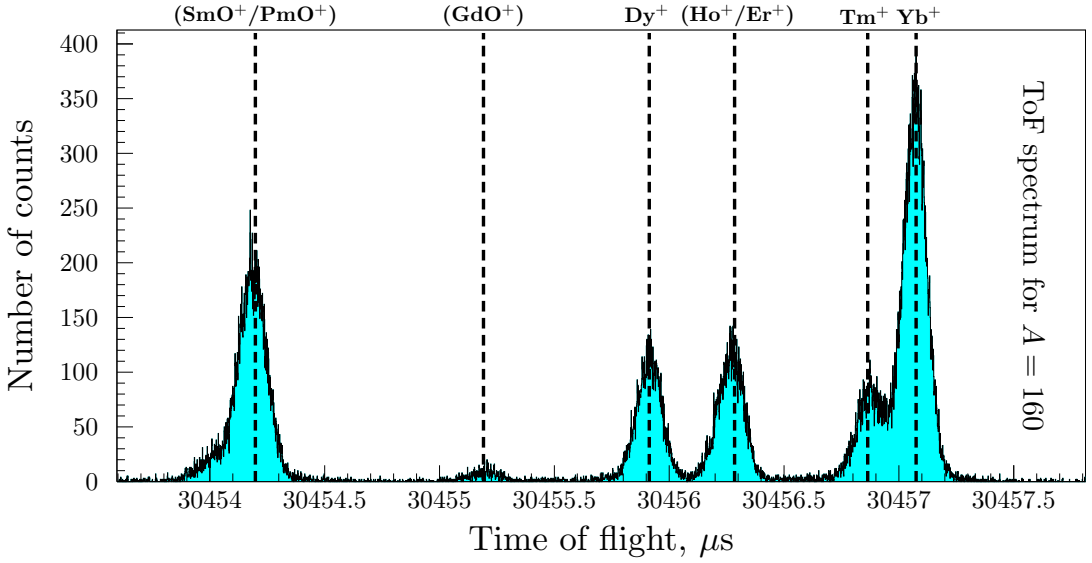

As previously mentioned, calibration of the MR-TOF MS can be performed either with offline $^{85}Rb^+$, $^{133}Cs^+$, $^{39}K^+$ or by using one/many online isobar/s (this applies only if the mass of the isobar/s in the spectra is known with sufficient precision). The offline calibration needs to be carried out before and after the online measurement, due to the temperature drifts as observed in the time-of-flight spectra. These drifts can lead to changes by few μs in the interval of a few days. On the one hand, the temperature dependence refers only to the absolute time of flight and affects the offline calibration (needs to be performed every time when online measurement is taken). On the other hand, the difference between different time-of-flight peaks present in the same spectra is a stable quantity. Therefore, whenever an online isobar with a well-known mass is available, it is taken as the preferred calibrant, minimising the effects of the temperature fluctuations.

3.2.4 Preparation Penning trap

The energy of the incoming ion-beam is further decreased by a second pulsed drift tube down to 100 eV before injection into the preparation Penning trap [Rai+97]. This Penning trap has a

Figure 3.8: Experimental release curve of $^{148}Cs^{+}$ ($T_{1/2}$ = 146 ms), obtained with the MR-TOF MS by varying the delay between the proton impact time on the target and the opening of the ISOLDE beam gate.

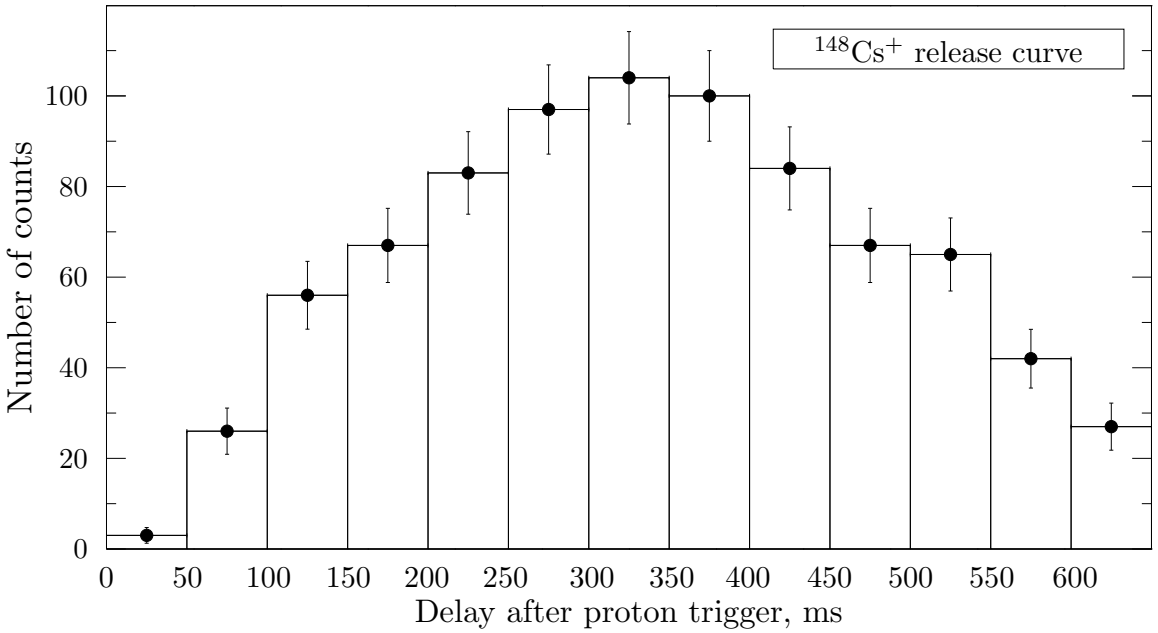

cylindrical shape and is placed in a superconducting magnet with a field strength of about 4.7 T. Main purpose of this device is to further clean the beam from isobaric contamination and to cool down the ions before they are transferred to the measurement trap. The trap itself is constructed from 20 cylindrically-shaped electrodes, which can be subdivided into the inner and the outer configurations. The inner configuration, e.g., the ring electrode, is the place where an excitation of all ion motions can be applied for the isobar-cleaning process. This electrode is 8-fold segmented, which allows the usage of even higher order excitation, such as octupolar excitation [Ros+12]. The outer configuration consists of two types of electrodes, correction or end-cap electrodes. This part of the trap is where ions are trapped, cooled and sometimes accumulated before they are moved into the inner (centre) region.

When the ion ensemble is loaded into the trap, it is likely to have a large energy spread probing bigger volume of the trap region. The mass resolving power for the isobaric cleaning is directly proportional to the relative velocity spread of the ion ensemble. This spread becomes an important issue when performing high-precision mass measurements. Therefore, ion cooling is used in order to reduce the energy spread and to have the ions better localised in the trap [Sav+91]. The simplest cooling technique employs a buffer gas. In this way there is an energy exchange between the "hot" trapped ions with the "cold" buffer gas molecules. Trap characteristics are unaffected once the buffer gas pressure is sufficiently low. Usually, the buffer gas specie is chosen to be a light inert gas. Having these considerations in mind, the precision Penning trap is filled with helium buffer gas and typically maintained at pressure of about $p = 10^{-3} - 10^{-4}$ Pa.

Due to the collisions with the buffer gas, ions injected into the trap will loose kinetic energy. The resulting damping force is dependent on the velocity of the ions and it can be written as:

$$\overrightarrow{F} = -2m\gamma\overrightarrow{v}, \tag{3.2}$$

Figure 3.9: Left: A photograph of the preparation Penning trap used at ISOLTRAP. Right: A sketch of the device is presented. The cylindrical trap has an inner diameter of 35 mm and is 250 mm long. The inner diameter of the last electrode (Endcap D in the sketch) is 1.5 mm.

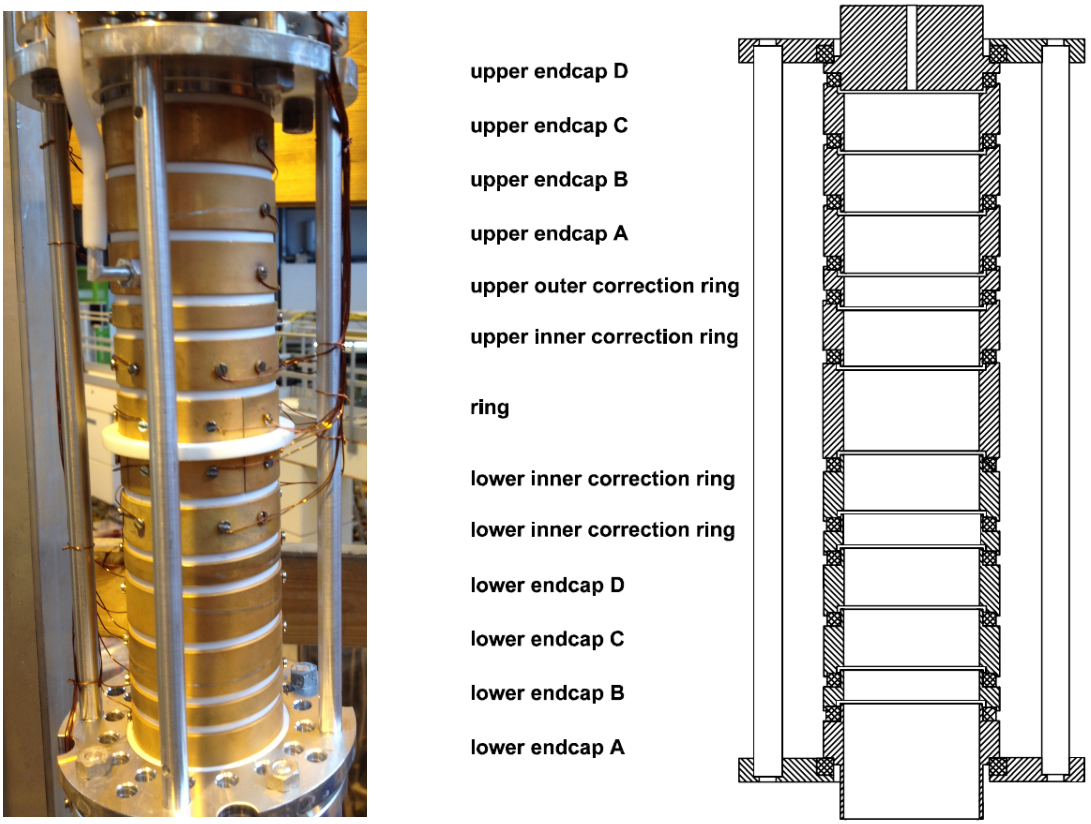

where γ is a damping coefficient which can be determined by the buffer gas properties:

$$\gamma = \frac{q}{2M}\frac{1}{K_0}\frac{pT_0}{p_0T}, \tag{3.3}$$

with q and M being the charge and mass of an ion, K_0 is the reduced mobility constant for the room temperature $T_0 = 300$ K and atmospheric pressure $p_0 = 10^5$ Pa. The damping force changes the motion of the trapped ions by decreasing their cyclotron motion and increasing their magnetron one. To avoid ion losses the two motions are coupled via quadrupolar excitation. By appropriately choosing the amplitude of the quadrupolar excitation and the buffer-gas pressure, one can decrease all ion-motions' amplitudes, that is cooling the ions. The evolution of the magnetron and the cyclotron motion can be described as:

$$\rho(t) = \rho_0 e^{-\alpha t}, \tag{3.4}$$

where ρ_0 is the initial magnetron or cyclotron radius at which the particles were injected, the constant α is a damping coefficient expressed as:

$$\alpha_\pm = \pm\gamma\frac{\omega_\pm}{\omega_+ - \omega_-}. \tag{3.5}$$

The isobaric separation procedure starts after all ions are cooled down to the centre of the preparation trap. Isobaric selectivity is achieved by first applying a dipolar excitation, which will increase the radius of the magnetron motion of all trapped species since in first order approximation it is mass independent. The amplitude of the dipolar excitation is chosen such that all ions are excited to the orbit with radius bigger than 1.5 mm. The latter is the radius of an aperture installed behind the last end-cap electrode. In order to achieve the isobaric selectivity, a quadrupolar excitation is applied to a specific cyclotron frequency matching the one of the ions of interest. Therefore, only ions having this one specific frequency (and consequently one specific mass due to 2.7) will be re-centred back to the trap axis. This is because the quadrupolar excitation converts the slow magnetron motion to the fast cyclotron motion. In the presence of the buffer-gas the latter is damped very quickly to the centre of the trap. When the ions are ejected from the trap, all species left with a large magnetron radius will encounter the walls of the aperture and be lost in the process. In general, a mass resolving power of the order of $R \approx 10^5$ can be achieved by this method, which is sufficient to remove most of the isobaric contaminants coming with the ions of interest.

3.2.5 Precision Penning trap

After this isobar cleaning process, the selected ion species are transferred to the precision Penning trap for performing the actual mass measurement. The ToF-ICR technique is used as described in Sec. 2.2.3. The precision Penning trap is a hyperbolic trap having a four-fold segmented ring electrode and lower/upper end-caps. A photograph of the device as well as a simplistic drawing are given in Fig. 3.10. The lower end-cap is put to a lower potential allowing the ions to enter the trap. When the ions are in the centre, a trapping voltage is applied to the end-cap. Furthermore, the ring electrode of the preparation and the precision trap are set to the same trapping potential. Having these precaution steps prior to the actual measurement ensures two facts: (1st) a minimum amplitude of the ions' axial motion in the precision trap and (2nd) the part of the trap region explored by the ions has almost negligible field imperfections.

The precision trap is operated at a pressure of about $p = 10^{-5}$ Pa in order to minimise disturbing collisions with rest-gas atoms and molecules, which can broaden up the resonance and thus increase the uncertainty in the determination of the cyclotron frequency. The trap itself is placed in the centre of a homogeneous 5.9 T superconducting magnet.

While stored in the precision trap, the cooled ions are subject to the dipolar excitation at the magnetron frequency causing ions to increase their magnetron radius to about 0.7 mm. After applying the quadrupolar excitation, ions are ejected and detected using a multi-channel plate detector, which is placed at a distance of about 1.2 m downstream the trap and outside of the magnetic field.

To clean finally any remaining close-lying isobaric and isomeric contamination, which could not be separated in the previous two traps (MR-TOF and the preparation trap), it is possible to perform a purification technique in the precision trap itself. For this, a dipolar excitation at the modified cyclotron frequency (ν_+) of the expected contaminant is applied [Web+05]. The amplitude of the excitation is large and chosen such that the resulting cyclotron radius increases until the contaminating ions hit the surrounding walls. To avoid sideband excitations of the ions of interest, the dipolar excitation signal is modulated by a Gaussian envelope.

The mass-resolving power in the case of a Penning-trap mass spectrometry can be derived through the cyclotron frequency

$$R = \frac{\nu_c}{\Delta\nu_{FWHM}},$$

Figure 3.10: Left: A photograph of the precision Penning trap taken during 2013. Right: A simplified sketch of the trap, where the correction elements are shown in light grey and the main electrodes are coloured in dark grey.

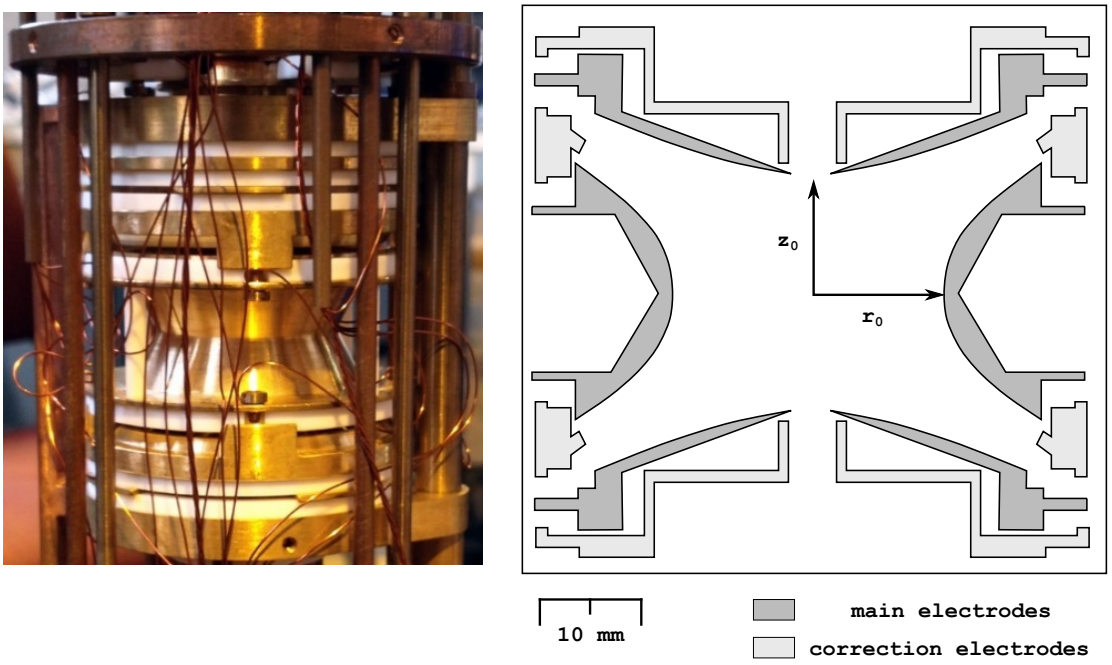

with $\Delta\nu_{FWHM}$ being the full-width at half-maximum of the central dip in the ToF-ICR spectrum. Resolving power that can be achieved using the precision trap for an ion with $A = 100$ u is 10^7. This allows for the resolving of nuclear ground and isomeric states [Bol+92a; Bla+04]. Trap-assisted decay spectroscopy setup was installed behind the precision trap, benefiting from the high-resolving power. Description of the setup and the results obtained from experiments performed in 2013 can be found in Refs. [Kow+12; S+13].

The duration time used for the quadrupolar excitation determines the width of the resulting time-of-flight resonance and scales as $\Delta\nu_c/\nu_c \approx 1/T_{rf}$. Typical applied excitation times range from 100 ms to about 1.2 s, depending on the half-life of the measured species. However, excitation times of up to 10 s can be applied for nuclei close to stability.

Chapter 4

Data analysis and results

This chapter describes the analysis of the acquired Penning-trap (PT) and the MR-TOF MS data. Furthermore, a discussion on the newly applied maximum-likelihood method is given. The results for each measured nuclide of cadmium and caesium isotopes are presented. Details of the experimental campaigns are summarised in Table 4.1.

4.1 Principle of mass determination using a Penning trap

As it was already introduced in the previous chapters, the ion mass can be determined from measurements of the cyclotron frequency. However, following the relation in Eq. (2.7), a calibration of the magnetic field needs to be carried out simultaneously with the cyclotron frequency measurement. Since such task is currently not possible, the calibration is done by taking cyclotron frequency measurements of reference ions with a well-known mass before and after the corresponding measurement of the ion of interest. Afterwards an estimate of the magnetic field strength is done by using the following interpolation function:

$$\bar{\nu}_{ref} = \frac{(\nu^a_{ref} - \nu^b_{ref}) \cdot (t^m - t^b)}{(t^a - t^b)} - \nu^b_{ref}, \tag{4.1}$$

where ν_{ref} correspond to the cyclotron frequency of the reference ion, t is the measurement time and the indices a, b, m indicate that the measurement was performed *after* (a), *before* (b)or with the ion of interest (m), respectively. Assuming all ions have the same charge state $q = +e$, substituting the magnetic field with the estimated cyclotron frequency for the reference ion and replacing the ion mass with the atomic mass, one obtains:

$$M = \frac{\bar{\nu}_{ref}}{\nu} \cdot (M_{ref} - m_e) + m_e, \tag{4.2}$$

where m_e is the mass of the electron. However, in this way the atomic mass uncertainty of the reference specie is included into the uncertainty of the resulting mass. Therefore, to decouple the experimental uncertainties from the ones coming from the reference ion, the results from the mass measurements at ISOLTRAP are useful to report as frequency ratio:

$$r = \frac{\bar{\nu}_{ref}}{\nu}. \tag{4.3}$$

Table 4.1: Summary of the two experimental campaigns. The dates of the experiments are given in the first column. The target material, the ion-source type, the ISOLDE mass separator and the ion-beam energy are given. The last column presents the measured nuclides.

Date	Target/line	Source	Separator	Energy	Measured nuclides
Oct 2012	UCx/Ta	Ta-surface	HRS	50 keV	^{132,146,147,148}Cs
Aug 2014	UCx/quartz-insert	RILIS	HRS	30 keV	^{129,130,131}Cd

Following this approach the masses of the ions of interest can be recalculated at any later time whenever improvement in the mass of the referent ion is available. The ratio in Eq. (4.3) obtained at ISOLTRAP is thus invariant and does not vary. Thus a mass measurement at ISOLTRAP consist of three independent cyclotron frequency measurements:

1. calibration measurements with a reference ion to determine the magnetic field in Eq. (2.7)
2. measurement of the cyclotron frequency of the ions of interest.
3. repeat the reference measurement (1).

The uncertainty of the frequency ratio is determined according to the uncertainty propagation law. The final value is composed of the experimental standard deviations of the three measurements including various uncertainties due to systematic effects. The resonance curve usually consists of 41 frequency steps, accumulating more then 1000 ions in total for the reference measurements. In the case of more exotic radioactive species a measurement with less ions is required (either due to the half-life constrains or low production yields). Therefore, the duration of the measurement needs to be a compromise between the lowering of the statistical error due to the increase in the total number of measured ions on one hand and raising the uncertainty coming from the magnetic field drift on the other hand. Finally, the total uncertainty of the frequency ratio measurement contains uncertainties from three different sources:

$$\sigma_{tot}^2 = \sigma_{stat}^2 + \sigma_{mass}^2 + \sigma_{res}^2, \tag{4.4}$$

where $\sigma_{stat}, \sigma_{mass}, \sigma_{res}$ are the statistical, mass-dependent and residual systematic uncertainties, respectively. A study done back in 2003 year had as a primary aim to identify and quantify all effects that contribute to the uncertainty of the primary result. More information about the scale of the various uncertainties can be found in [Kel+03]. A similar study is planned for the near future, aiming to verify the current state of the setup.

4.1.1 Analysis procedure

The analysis of the Penning-trap data follows several steps:

- All ToF-ICR spectra are evaluated by a dedicated computer software EVA [SR16], widely used among the Penning-trap experiments. The program fits the spectra using the theoretical line shape described in [Kön+95], which has 4 free parameters. The uncertainty of each data point in the ToF-ICR spectra is weighted by the number of ions in this point as well as

by the width of the ToF distribution. After the least-square minimisation procedure, the free parameters such as cyclotron frequency and initial magnetron radius together with their uncertainties are obtained.

- The next step in the analysis is to check for the presence of contaminations within the obtained spectra by the so-called *z-class* analysis. This procedure is performed for a ToF-ICR spectra containing sufficient statistics. In essence, a cyclotron frequency is determined for different numbers of ions that were present in the precision trap, grouped in classes. Each determined centroid frequency is then plotted versus the number of the ions for this particular class. A linear least-squares fit is then applied to the data points. The fit is extrapolated to a final number of ions corresponding to unity or to such that accounts for the efficiency of the detector [Bol+92a; Kel+03].

- The interpolation of the cyclotron frequency of the reference ion to the time of the measurement of the ions of interest is performed next. The uncertainty from the field fluctuations is taken into account and is added quadratically to the statistical uncertainty [Kel+03]:

$$\frac{\sigma_{\mathrm{B}}(\nu_{ref})}{\nu_{ref}} = 6.35(45) \cdot 10^{-11}/\mathrm{min} \cdot \Delta T, \tag{4.5}$$

  where ΔT is the time interval between the two reference measurements. The time duration in experiments using short-lived radionuclides, whose production rate is low, can in some cases be in the order of several hours required for the collection of sufficient statistics to determine the cyclotron frequency. In such cases the uncertainty due to the field fluctuations can become comparably large and thus can be avoided by interrupting the on-line collection for a quick reference measurement.

- Afterwards follows the determination of the frequency ratio and its uncertainty by using the interpolated cyclotron frequency of the reference ion and the frequency from the resulting fit for the ion of interest.

- The weighted mean value for all available frequency ratios for a given nuclide and its weighted uncertainty can be computed via:

$$\bar{r} = \frac{\sum_i \frac{r_i}{\sigma^2(r_i)}}{\sum_i \sigma^2(r_i)}, \tag{4.6}$$

$$\sigma^2(\bar{r}) = \frac{1}{\sum_i \sigma^2(r_i)}. \tag{4.7}$$

  The consistency of the data is checked by calculating the reduced χ^2 using the weighted average ($\bar{r}$). The distribution of different frequency ratios should follow the χ^2 distribution. Thus, if $(\chi^2/(NDF^{1}) \leq 1)$ the averaged ratio is used without modifications. If the value is $(\chi^2/(NDF) > 1)$ it indicates a source of an additional systematic uncertainty. If the origin of this uncertainty is not identified then the uncertainty $\sigma(\bar{r})$ is increased by a factor $\sqrt{\chi^2/(NDF)}$ according to [NG10].

- In the last step, the remaining mass-dependent shift and the residual uncertainties are accounted in the final result. The mass-dependent shift is a result of the systematic studies carried out with different carbon clusters [Kel+03] and was estimated to be:

$$\sigma_{mass} = 1.6 \cdot 10^{-10}(M - M_{ref})u^{-1}. \tag{4.8}$$

[1] number degrees of freedom

This uncertainty can either be due to imperfections in the quadrupole rf-field or by a misalignment in the trapping electrostatic field. Eq. (4.8) shows also the importance of choosing the mass of the referent ion. The mass of the latter should be kept as close as possible to the mass of the ion of interest. For example in the case of cadmium the corresponding mass difference was kept below 7 u by choosing ^{133}Cs as the reference ion. Thus, the resulting uncertainty σ_{mass} has a magnitude of $1.1 \cdot 10^{-9}$. The residual systematic uncertainty determines the systematic limit of the ISOLTRAP mass spectrometer. Currently, the uncertainty is estimated to be:

$$\sigma_{res} = 8 \cdot 10^{-9} \tag{4.9}$$

The final comparison with already existing experimental data is done by converting the frequency ratio to the mass excess, via:

$$ME = (M - A \cdot \mathrm{u}), \tag{4.10}$$

where the atomic mass m is calculated according to Eq. (4.2), A is the mass number and u = 931494.009(7) keV/c^2 is the atomic mass unit [Aud+12a].

4.2 Multi-reflection time-of-flight mass spectra

The MR-TOF MS data consists of online and offline time-of-flight spectra for the ions of interest and the reference ions, respectively. As discussed in Chapter 2, Sec. 2.4.1, the determination of the unknown masses relies on the precise knowledge of the nuclides' time-of-flights. Here, as in the case of the Penning-trap data, the atomic mass uncertainty of the reference species will contribute to the uncertainty of the resulting mass. Therefore, the results from the MR-TOF MS data are also reported as ratios. The time-of-flight ratio in this case is the multiplication factor from Eq. (2.55):

$$C_{ToF} = \frac{2T_x - T_1 - T_2}{2(T_1 - T_2)}. \tag{4.11}$$

The unknown mass can then be calculated as a weighted mean value of all ToF ratios and its weighted uncertainty likewise it is done for the frequency ratios.

The conventional approach to bin the data and perform χ^2 analysis suffers from information loss and arbitrariness of the binning procedure. This becomes especially important for low count rates. One way to overcome this problem is by using unbinned likelihood estimation [Myu03]. It is known that the unbinned likelihood method is superior with regard to the expected chi-square distance between experimental data and model, and in general also with regard to the mean square errors of the individual model parameters. Therefore, our aim was to develop and apply the unbinned maximum-likelihood procedure to analyse the MR-TOF MS data for ^{131}Cd isotope. In addition to the consideration mentioned above, the low production yield and the short half-life of this particular cadmium isotope resulted in spectra with number of counts per time bin not exceeding 10-15, which can be interpreted as a lower limit for the usage of traditional χ^2 statistics [Arz+07].

In the following a presentation of the newly applied Maximum-Likelihood method is given. The method also aimed at investigating different shapes for the asymmetric ToF peaks (see Fig. 4.1).

Maximum-Likelihood method

Likelihood is the hypothetical probability that an occurred event would yield a specific outcome or result [Fie97; Ald97]. The basic difference between the concepts of probability and likelihood

is that probability is referring to the occurrence of future events, while likelihood refers to the past events with already known outcomes. The method employed for this analysis is a procedure giving the value of one or more parameters for a given sample of observable/s by making the known likelihood distribution of a probability density function (PDF) a maximum, hence the name Maximum Likelihood (ML). The likelihood function can be written as a product of the PDF at each point $\vec{x}$ for a given parameter q as:

$$L(q) = \prod_i F(x_i; q) = F(x_0; q) * F(x_1; q) * F(x_2; q)..., i = 1, ...n. \tag{4.12}$$

It is convenient to re-write the above statement in terms of the negative logarithm of the ML ($-\ln L(q)$) and substitute the product by a sum operation:

$$-\ln L(q) = -\sum_i \ln F(x_i; q), \tag{4.13}$$

where the estimation of the model parameters is then performed by a minimisation procedure:

$$\left.\frac{d \ln L(q)}{dq}\right|_{q_i=\hat{q}} = 0. \tag{4.14}$$

The ML estimator for the parameter variance of a given model is calculated by the second derivative of the $-\ln L(q)$ at the minimum:

$$\hat{V}(q) = \left(\frac{d^2 \ln L}{dq^2}\right)^{-1}. \tag{4.15}$$

Having these concepts in mind, one can take a normal distribution (Gaussian distribution) as the most frequent distribution example occurring in nature and compute the likelihood and its estimators:

$$L(x_1, x_2..., x_n|\mu, \sigma) = \prod_i \frac{1}{\sigma\sqrt{2\pi}} e^{-(x_i-\mu)^2/2\sigma^2}.$$

If we take the logarithm and its first derivative:

$$\ln L = -\frac{1}{2} n \ln(2\pi) - n \ln \sigma - \frac{\sum (x_i - \mu)^2}{2\sigma^2},$$

with

$$\frac{d \ln L}{d\mu} = \frac{\sum (x_i - \mu)}{\sigma^2} = 0$$

we get the mean estimator of the distribution

$$\hat{\mu} = \frac{\sum x_i}{n}.$$

Similarly we can write the expression for the standard deviation

$$\frac{d \ln L}{d\sigma} = -\frac{n}{\sigma} + \frac{\sum (x_i - \mu)^2}{\sigma^3} = 0$$

giving for its estimator the form

$$\hat{\sigma} = \sqrt{\frac{\sum (x_i - \mu)^2}{n}}.$$

Maximum-Likelihood estimators

The parameter estimator in statistical modelling is known as a method used to infer the values of an unknown parameter of a given distribution. The properties of perfect estimators are:

- **Consistent**: the true parameter value that generated the distribution is recovered asymptotically following $\lim_{n\to\infty}(\hat{q}) = q$, i.e. the correct answer is given if infinite number of samples exists
- **Unbiased**: The bias b of the parameter estimator is defined as the difference between this estimator's mean value and the true value of the parameter being estimated. An estimator with $b = 0$ is called unbiased and for finite statistics gives the right answer on average.
- **Efficient**: lowest-possible variance of parameter estimates achieved asymptotically

$$V(\hat{q}) = \left(1 + \frac{db}{dq}\right) \cdot \left(\frac{d^2 \ln L}{dq^2}\right)^{-1}$$

In reality there are no perfect estimators and the maximum-likelihood estimators (MLE) are in general *consistent*, *mostly unbiased* (their bias scales as $1/n$ and a special care should be taken at small n), *efficient* for large n (giving the smallest possible error) and *invariant* (after performing a transformation of the type $(\hat{q})^2 = \widehat{(q^2)}$ the result would not change). Main advantage of the MLE compared to regularly used χ^2 is demonstrated by RooFit team as they correctly treat histogram data with low statistics (even bins with zero counts). The result is simply explained by the fact that the events in the histogram bins are Poisson or binomial distributed while in the case of χ^2 they would be distributed according to Gaussian.

4.2.1 Analysis Procedure

The MR-TOF MS experimental data represent the number of counts observed in a given time-of-flight window. An example of the measured spectrum is presented in Fig. 4.1. The data were collected online by using a Multi-channel analyser from FASTcom company (model P7887), which has a minimum time resolution of 250 ps. However, the P7887 was configured to record the data in a time bin of 1 ns. The hardware stored the data in an ascii format which later is fed to the analysis software. The data were prepared as a one-dimensional histogram (TH1D class in ROOT). Within the software, a maximum-likelihood method is implemented. In the following section description of the method is given.

RooFit environment

In the MR-TOF MS analysis, PDF models were constructed and employed in the fitting procedure by taking advantage of the libraries of the data-analysis toolkit RooFit [VK05]. This is a software analysis environment specifically build to work with probability density functions. It extends the ROOT data analysis framework [BR97] by providing basic data modelling capabilities in addition to the visualisation and data processing tools already available with ROOT. The most important key features of RooFit are:

Figure 4.1: An example of an off-line time-of-flight spectrum for off-line ^{85}Rb ions trapped in the MR-TOF device for a time of 500 revolutions.

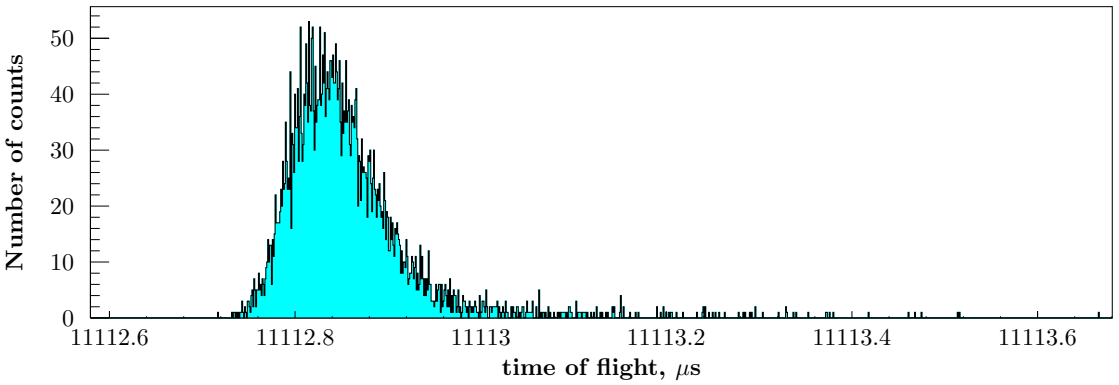

- *natural and self-documented vocabulary* - constructing models in terms of its building blocks and their assembly within the model (e.g. addition, composition and convolution of several distributions).
- *data description language* - observable quantities are being modelled using naturally descriptive titles, units and any cut ranges
- *generic fitting capabilities* - fitting routines can be applied to any model with (binned/unbinned) maximum-likelihood or χ^2 approach
- *correct error estimation* - tools for calculating a Poisson or binomial uncertainties for experimental data

Building a PDF model

The peak of interest does not follow an ideal Gaussian distribution, as seen from the 1-D Time-of-flight spectrum in Fig. 4.1. A slight asymmetry is observed which is commonly referred as a tail in the Gaussian peak. Therefore, the aim of this analysis was to investigate a PDF model, which takes into account the tails of the peaks. For this reason a PDF which is a convolution of a Gaussian probability distribution:

$$G(x;\mu,\sigma) = e^{-(x-\mu)^2/2\sigma^2}, \tag{4.16}$$

and Single- (SEG) or Double- (DEG) sided exponential distribution:

$$E(x;\tau) = e^{-x/\tau} \tag{4.17}$$

$$E(x;\tau) = e^{-|x|/\tau}, \tag{4.18}$$

was constructed:

$$M(x;\mu,\sigma,\tau) = G(x;\mu,\sigma) \otimes E(x;\tau) = \int_{x_{min}}^{x_{max}} e^{-(x-\mu)^2/2\sigma^2} \cdot e^{-|x-x'|/\tau} dx', \tag{4.19}$$

where x_{min} and x_{max} denote the limits for the range under consideration, μ, σ are the Gaussian mean and standard deviation, τ is the decay time of the exponent PDF. Three possible solutions to build such a convolution model exist in RooFit (one analytic and two numerical). A precision and

fast calculation of the convolution integral is a necessary condition since the PDFs are evaluated a large number of times in the course of the fitting procedure. An analytical expression for the convolution integral is hence highly recommended. For our study analytic functions were already implemented in the RooFit library (named within the library as RooDecay and RooGaussModel) and were thus used in this analysis.

The Single-sided exponent PDF produces a tail in the Gaussian distribution only on one of its sides and hence leaves the final distribution asymmetric. In the case of the Double-sided exponential in the convoluted PDF, the result will sometimes lead to a symmetric final distribution and in some cases with tails on both sides. Both convoluted distributions did produce tails which could be used to describe the data more accurately than an ideal Gaussian distribution. However, the study found that in the SEG case the final stability of the fitting routine depends critically on the selected fitting range. An example of ToF spectra is presented in Fig. 4.9 together with three fits considering the three discussed distributions.

Although these convoluted distributions show reasonable results, no arguments could be found to explain why this particular distribution would produce asymmetric ToF peaks. Thus in the next steps only results for the Gaussian distribution obtained by maximum-likelihood and least-square minimisation procedure were considered.

Figure 4.2: The same time-of-flight peak as in Fig. 4.1, but in a zoomed time window. Three different peak distributions are presented after a fit to the data. A Gaussian distribution is given in red. A convoluted Gaussian with single-sided exponential (SEG) is shown in black and convoluted Gaussian with double-sided exponential is presented in blue (DEG).

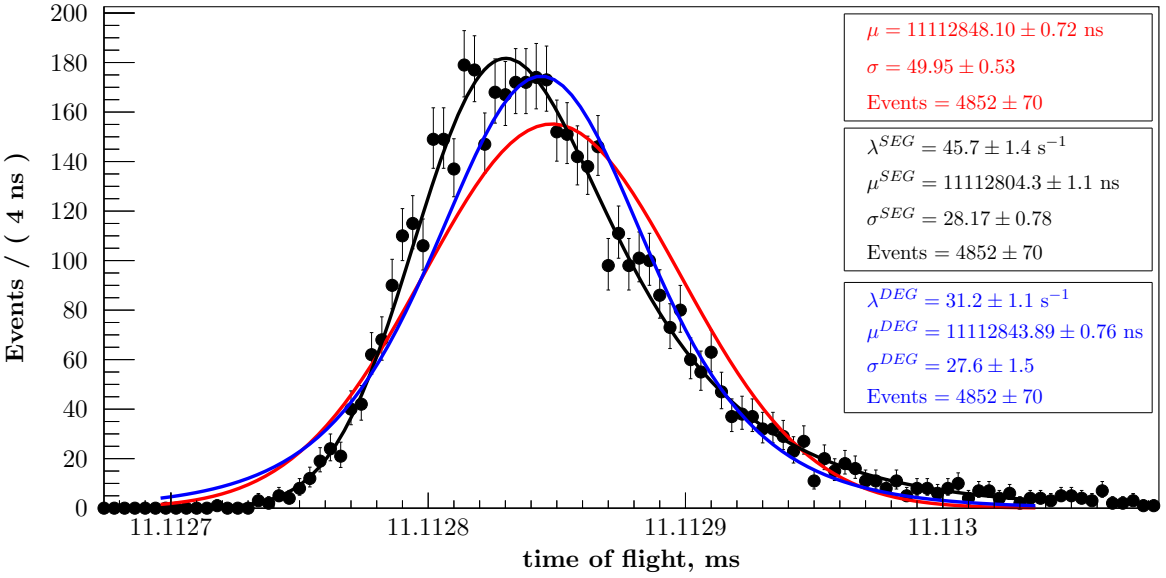

4.3 Results

The masses of two isotopes of cadmium (^{129,130}Cd) and four isotopes of caesium (^{132,146,147,148}Cs) were measured using the precision Penning trap and the ToF-ICR technique. The ^{131}Cd isotope was measured using the MR-TOF MS technique and was analysed by the Maximum-Likelihood method.

All of the obtained frequency ratios are summarised in Table 4.2. All obtained results are compared to AME2012 [Aud+12a], which is the latest published mass evaluation, and consequently included in the new upcoming evaluation. All measurements used $^{133}Cs^{+}$ as a reference ion [Aud+12a; Bra+99] available from the surface-ion source at ISOLTRAP. Before and after all experimental runs, cross-reference measurements were carried out in order to minimise any temporal systematic shifts in the system. Therefore, multiple ToF-ICR measurements determining the mass of ^{85}Rb have been performed. These studies take advantage of the second reference ion mass available from the offline ion-source. Results from these cross-check spectra show that the difference of the reference ion-mass determined with ISOLTRAP and the tabulated value in AME2012 [Aud+12a; Bra+99] is 0.26(1.21) keV. The results obtained from the cross-reference study are shown in Fig. 4.3.

Figure 4.3: Results of the time-of-flight ion-cyclotron-resonance measurements on the reference ^{85}Rb ions. The black line represents the tabulated value in the AME2012. The difference to this value after 11 measurements is $\Delta = 0.14$ keV. The shaded band indicates the total uncertainty as calculated in Eq. (4.4) and corresponds to $\sigma_{tot} = 1.24$ keV.

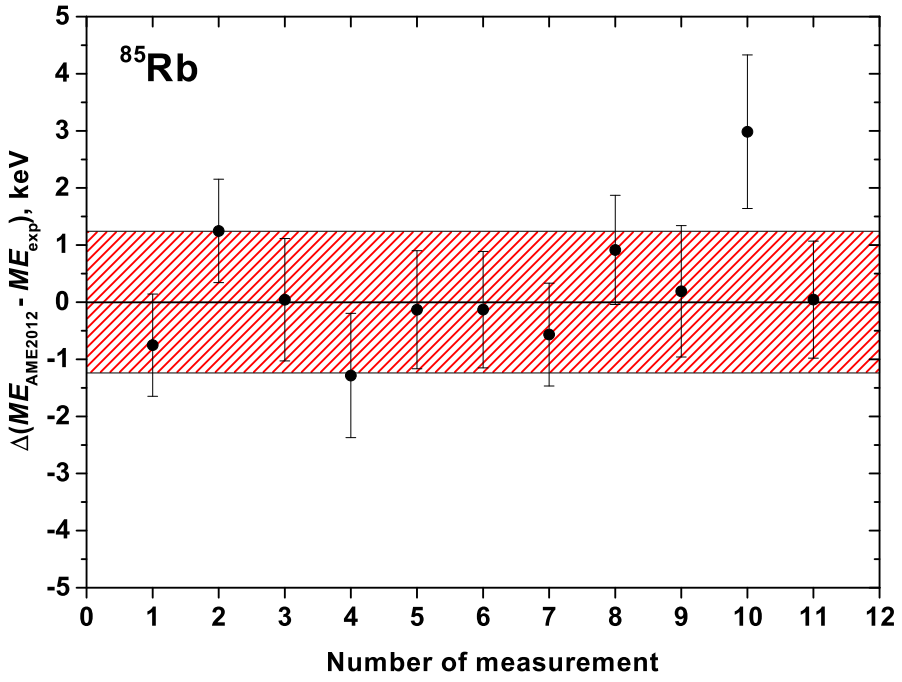

4.3.1 Neutron-rich cadmium isotopes

In this section the results of the mass measurements of neutron-rich cadmium will be discussed. Previous attempts to measure Cd isotopes over the $N = 82$ shell closure at ISOLTRAP [Bor+11; Bre+10] failed in the past due to the not isobarically clean sample. In the latest experiment a major technical improvements and developments led to the successful measurement campaign. First, the introduction of new ISOLDE target, which included neutron converter and quartz tube insert [Bou+08; Bou+07]. The latter enabled us to reduce the isobaric contamination of Cs and In by 4 orders of magnitude. Secondly, the successful operation of the MR-TOF device in comparison to the previous beam times. This trap opened new possibilities for the mass measurements of

exotic nuclear masses at ISOLTRAP [Wie+13; Kre+13; Wol+13]. Three independent analyses for the Penning-trap were performed, all of which agree within the given uncertainties. Concerning the MR-TOF data, two independent analyses were carried out. One incorporated an ordinary least-square analysis while the second one the Maximum Likelihood.

4.3.1.1 ^{129}Cd isotope

The mass of ^{129}Cd isotope was only estimated from systematic studies in this region. During the experimental campaign one regular ToF-ICR and three Ramsey-type resonances were taken. An example of such spectra is shown in Fig. 4.4. The mass excess value for this nuclide was determined to be $ME = -63\,058(17)$ keV. A low lying isomeric state was known to exists in ^{129}Cd

Figure 4.4: The time of flight ion-cyclotron-resonance of ^{129}Cd isotope. For each frequency value, the individual time of flights are indicated by colour-coded bins. The colour intensity of the bins represents the number of ions found in it. The mean time-of-flight of the ions is represented in full circles. The fitted theoretical resonance curve is represented by the red line.

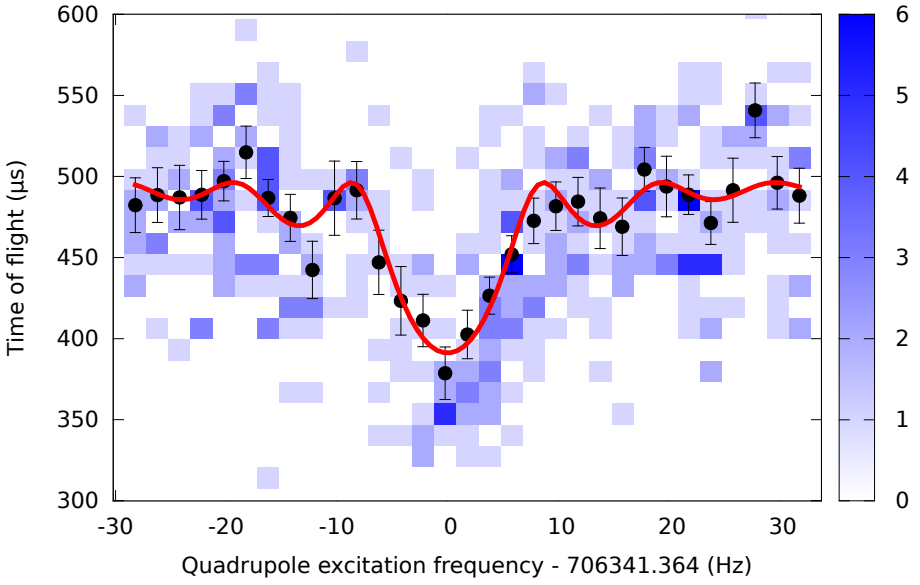

from previous half-life measurements as well as from the recent hyper-fine structure studies using collinear laser spectroscopy [Kra+05; Yor+13]. The two determined spin states have been assigned to $3/2^+$ and $11/2^-$ corresponding to the half-lives of 242(6) ms and 104(6) ms, respectively. During the experiment, half-life measurements were performed in order to address the state produced predominantly in the target. The extracted decay curve is presented in Fig. 4.5.

In the measurement, the cooling time in the buncher was varied. By increasing it, ions spent more time in cooling and more ions would be lost due to decay. Therefore, exponential decrease is observed. Fit to the data using one and two decay constants was performed. The fit result yielded a value suggesting that the measured state was the one having spin 3/2. However, the information obtained was not sufficient to exclude the presence of the other state in the beam from ISOLDE. Due to this fact, in the consecutive measurements the MR-TOF trapping time was adjusted to a period of about 7 to 8 half-lives of the shorter-lived state ($T_{1/2} = 104(6)$ ms). The aim of this increase was to adjust the ratio between 3/2 and the 11/2 states in favour of the

Table 4.2: The half-lives and the frequency ratios (r) between the cyclotron frequencies of the referent ion (^{133}Cs) and the ion of interest. The k parameter represents the number of ToF-ICR or MR-TOF MS spectra considered in the analysis.

Nuclide	Half-life (ms)	k	Ratio r or C_{ToF}
^{129}Cd	151(15),146(8)[2]	4	r = 0.970105338(136)
^{130}Cd	127(2)	3	r = 0.977645186(180)
^{131}Cd	98.0(2)	11	C_{ToF} = 0.4823044(539)
^{132}Cs	6.480(6) d	3	r = 0.9924832508(100)
^{146}Cs	321(2)	3	r = 1.0980789375(250)
^{147}Cs	230(1)	3	r = 1.1056304862(673)
^{148}Cs	140(0)	3	r = 1.113195127(1030)

Figure 4.5: Half-live measurement of ^{129}Cd isotope. The lower histogram presents the obtained data after varying the cooling time in the buncher. All other parameters were fixed during this measurement. The upper panel presents likelihood fit to the data using exponential decay with one decay constant. The value for the half-life obtained with this fit is $T_{1/2}$ = 203(10) ms. However only the statistical uncertainty is taken into account.

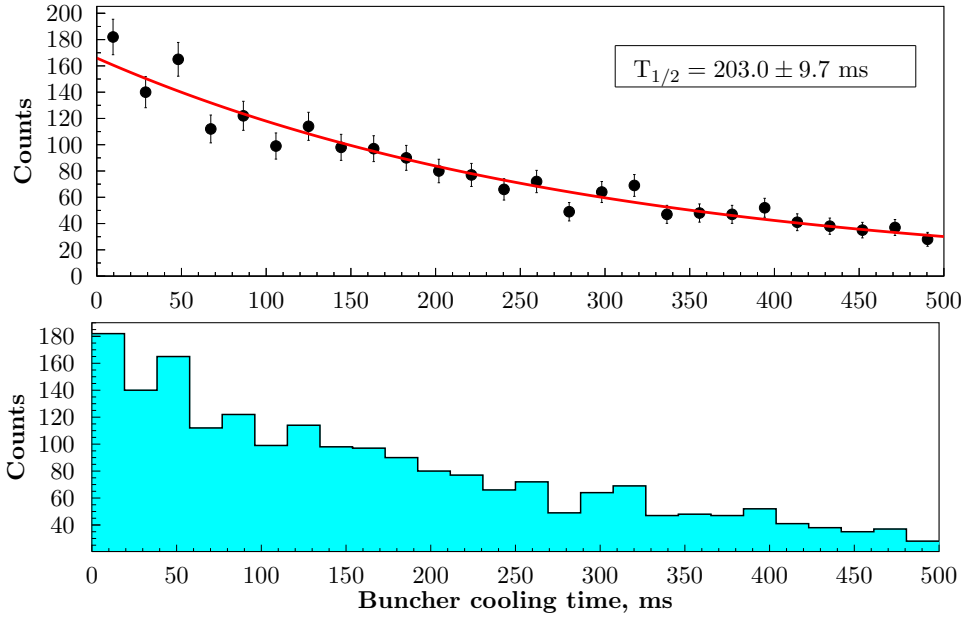

longer lived one. However, about one year after those measurements, new data from beta-decay experiment at RIKEN was published [Lor+15b; Tap+15]. The new results present similar values for both half-lives $T_{1/2}^{3/2}$ = 151(15) ms and $T_{1/2}^{11/2}$ = 146(8) ms.

[2]The values correspond to the $11/2^-$ and $3/2^+$ states, respectively, as determined by the new RIKEN experiment [Tap+15].

Figure 4.6: Excitation energies for the $11/2^-$ state in the odd-mass cadmium isotopes (black circles). The estimated excitation energy for the $11/2^-$ state in ^{129}Cd is given with red circle.

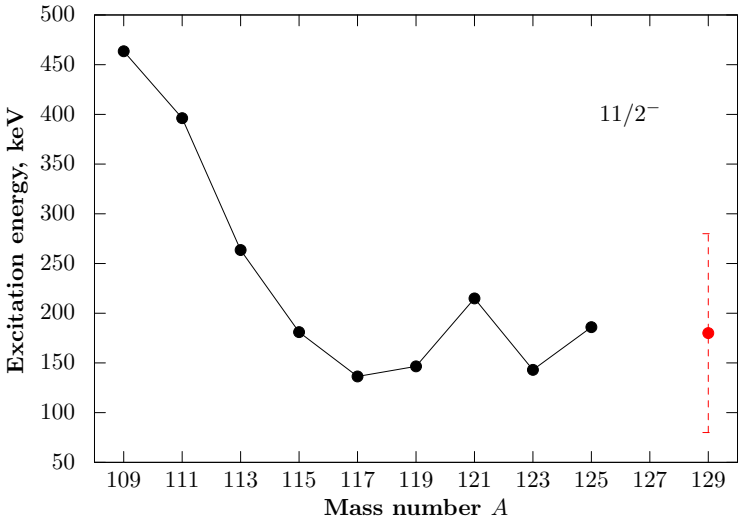

According to the RIKEN results the ratio of the states could not be optimised by varying the waiting time in the MR-TOF. Therefore, we have concluded that within the ToF-ICR spectra an unresolved isomeric state is present. This could potentially explain the observed contamination in the time-of-flight matrix clearly seen in Fig. 4.4 as scattered counts at time of flights corresponding to the non-excited ions, but found at the central region of the spectrum. Estimation for the excitation energy was performed by following the trend for the $11/2^-$ state from the odd-A cadmium isotopes. The excitation energies in the Cd chain is shown in Fig. 4.6.

The estimated energy difference between the ground and the isomeric state was inferred from the trend in the cadmium chain to be about 180(100) keV. Since a definite assignment of the determined ^{129}Cd$^+$ frequency ratio to one of the two nuclear states is not possible, an estimation for the pure ground state mass excess can be determined according to Appendix B of [Aud+12b], resulting in ME = −63 148(74) keV.

4.3.1.2 ^{130}Cd isotope

The mass of ^{130}Cd isotope was previously estimated from Q_β measurements and was included in the AME2012 [Dil+03]. From the Q_β value of the reaction the mass excess value resulted in $ME = -61\ 530(160)$ keV. The newest measurements presented in Fig. 4.7 from ISOLTRAP disagree with these values by 412 keV. The mass excess determined from the cyclotron resonance measurements gives a value of $ME = -61\ 118(22)$ keV. This suggests that the ^{130}Cd isotope is less bound compared to the previous beta-decay measurements. Representation of each individual measurement in comparison to the tabulated value of AME2012 is presented in Fig. 4.8. Mass data on $^{129-131}$Cd obtained by storage-ring mass spectrometry at GSI were recently presented in [Knö+16]. However, the published results have a factor of 10 larger uncertainties compared to the ones reported in this thesis. It is interesting to point out the mass value for the closed-shell nuclide ^{130}Cd, which deviates by almost 1 MeV in contrast to the Penning-trap data as well as to the previous findings from beta-decay spectroscopy.

Figure 4.7: Time-of-flight ion-cyclotron-resonance for ^{130}Cd isotope. The experimental time-of-flight of each detection event is represented. The colour map reflects the number of counts in each time-of-flight bin. The mean time of flight is shown for each frequency value (filled circles). The fitted theoretical resonance curve is represented by the red solid line.

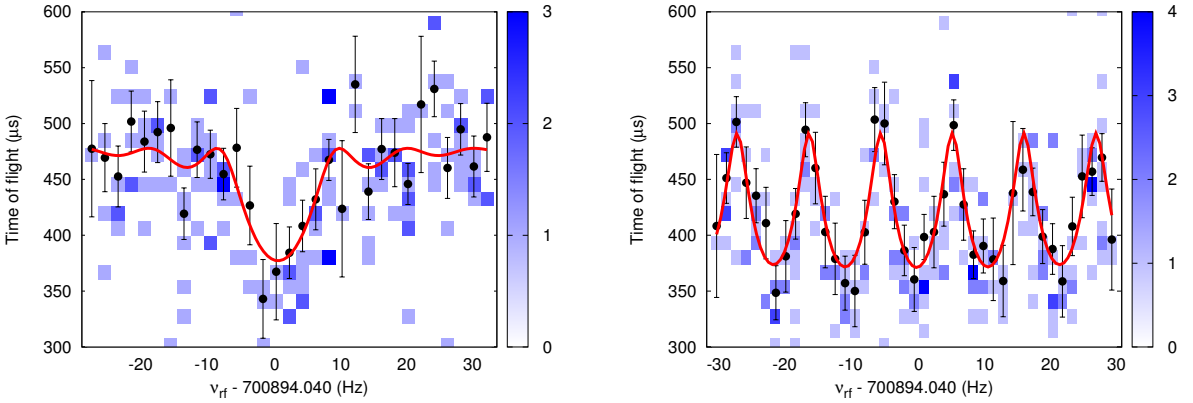

(a) A regular one-pulse quadrupole excitation with T_{rf} = 100 ms.

(b) Two pulse Ramsey-type quadrupole excitation with T_{rf}^{on} - T_{rf}^{off} - T_{rf}^{on} 10 ms - 80 ms - 10 ms.

Figure 4.8: Mass-excess values ME of the ^{130}Cd corresponding to masses calculated with frequency ratios of each individual measurement. The black solid line at zero is the AME2012 value while the cyan band represents its uncertainty. The mass excess corresponding to the mean frequency ratio from the new measuremetns is given with a red shaded band.

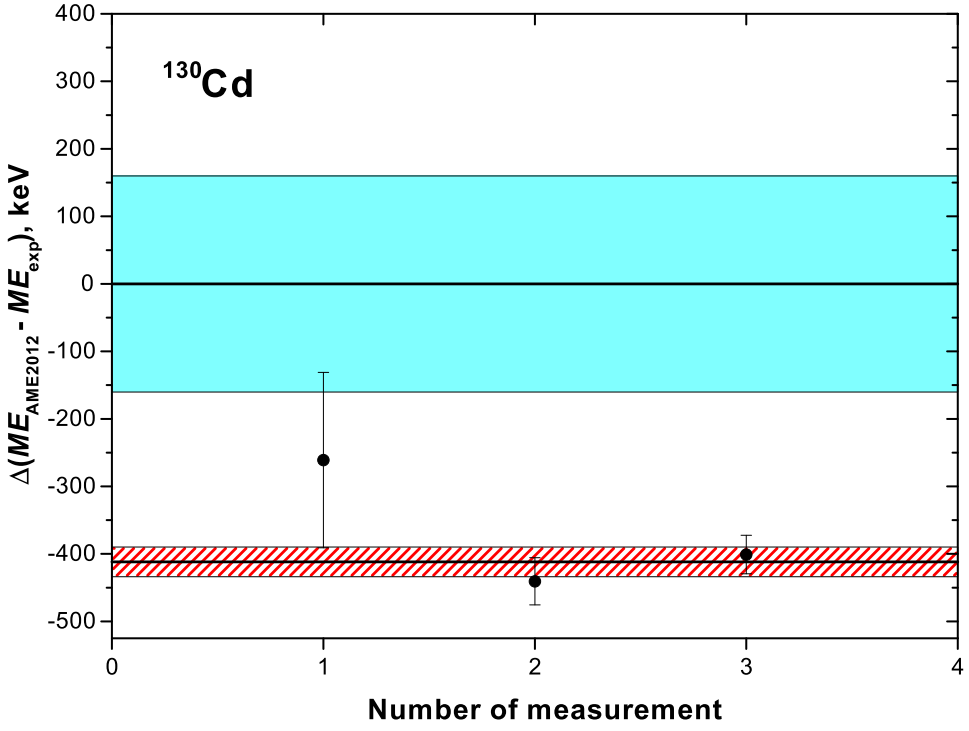

Figure 4.9: Time-of-flight spectrum obtained after trapping isobars with $A = 131$ in the MR-TOF device. The data was binned in every 4 ns. The red curve is a Maximum-Likelihood fit performed on the unbinned data assuming a Gaussian distribution.

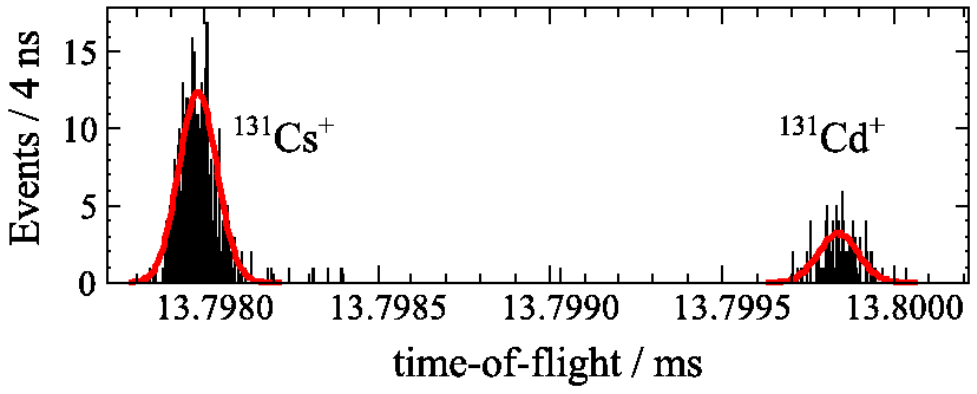

4.3.1.3 ^{131}Cd isotope

The analysis procedure for ^{131}Cd required a separation of the data in three sub-sets according to the trapping time spend inside the device, i.e. the revolution number 500, 800 and 1000. In total 11 files for ^{131}Cd were analysed. In this case, the main contaminant is ^{131}Cs which was delivered within the ISOLDE beam and which has a mass excess known to a precision of 5 keV. This contaminant was used as a reference ion to minimise the time-of-flight shifts. The results from the ToF fits were structured as triplets defining the calculation of the mass for the ion of interest. In Fig. 4.10 the comparison between the two fitting routines is given as well. Different models were used in order to investigate possible shifts in the final mass determination because of the assumption for Gaussian-like shape of the time-of-flight peaks. The comparison is presented in Fig. 4.2.

4.3.2 Neutron-rich caesium isotopes

4.3.2.1 ^{132}Cs isotope

In this case three Penning-trap Ramsey resonances agree nicely with each other. The determined mass excess value is $ME = -87\ 151.4(1.2)$ keV. The new result has however about 2σ deviation from the previously tabulated value in the AME2012.

4.3.2.2 ^{146}Cs isotope

The mass excess in this case is $ME = -55\ 305(3)$ keV. The tabulated value in AME2012 is $ME = -55\ 570(40)$ and deviates from our result by 264 keV. We note that the uncertainty of our new measurement is 2.9 keV. In the process of data analysis, a second Penning-trap experiment (the CPT situated at the CARIBU facility in Argonne, USA) published new value ($ME = -55\ 323.2(8.6)$ keV) in the same region. Comparing to the CPT value gives a difference of 18 keV [Van+13]. This is an about 2σ deviation if considering the uncertainties of both

Figure 4.10: Results for the mass excess of ^{131}Cd by taking isobaric contamination (^{131}Cs) from the same spectra and offline ^{133}Cs ions as the reference ions. The triplets determine the C_{ToF} ratio from which the ME is extracted. The black line represents the weighted mean value ($\overline{ME}$ = −55 212 keV) of all measurements considering the Maximum-Likelihood fitting procedure, while the light blue band correspond to its uncertainty $\sigma(\overline{ME})$ = 22 keV. The latter represents only the statistical uncertainty of the measurements.

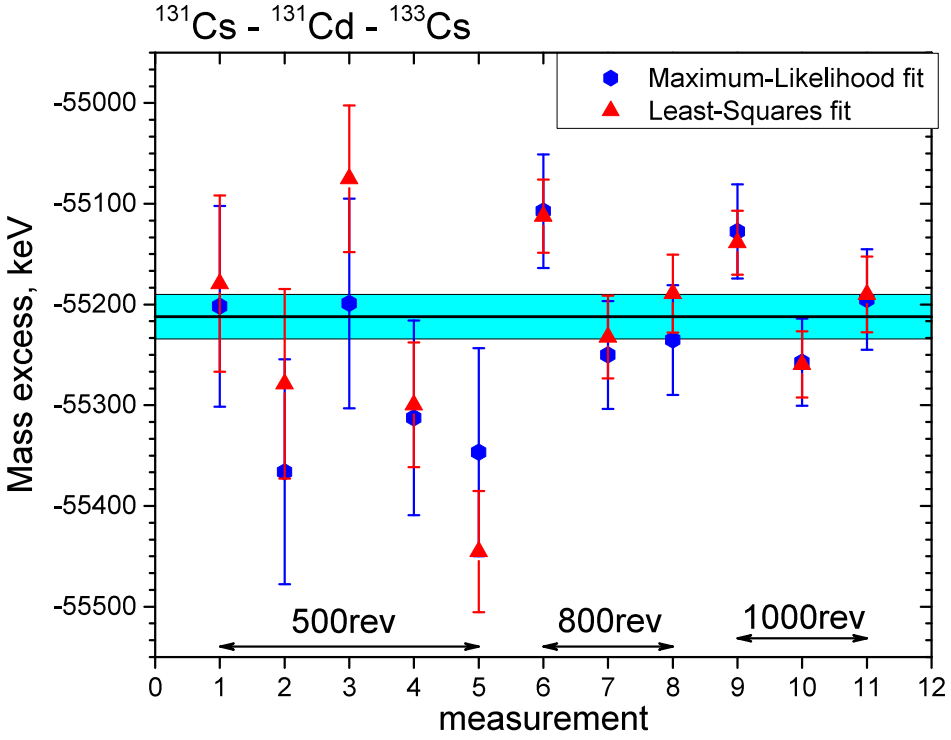

measurements. However, the new values are by an order of magnitude more precise compared to the tabulated one in the AME2012.

4.3.2.3 ^{147}Cs isotope

Previous investigations of this nuclide were done by Penning-trap mass spectrometry and in particular with the ISOLTRAP setup back in 2008 [Web+08]. The mass excess from this work was calculated to be ME = −52 011(60) keV. The newly determined mass excess is ME = −51 920.1(8.3) keV. A difference of about 90 keV is observed. Such deviation can originate from a contamination. In our last experiment new developments have led to more isobarically clean beams delivered to the precision Penning trap. In addition, the Cs beam was exceptionally pure in respect to a later attempt, in which an abundant stable Sm contamination was identified. This might have been the reason for the deviation of the results from different experiments.

4.3.2.4 ^{148}Cs isotope

This nuclide was previously investigated by beta-decay spectroscopy. The Q_β value was used to extrapolate the mass excess to ME = −47 300(580) keV. The new more precise values from the

Figure 4.11: Comparison of the mass-excess values ME, as determined in the present work the the corresponding tabulated values in AME2012. The shaded regions correspond to the uncertainty of the values indicated in AME2012.

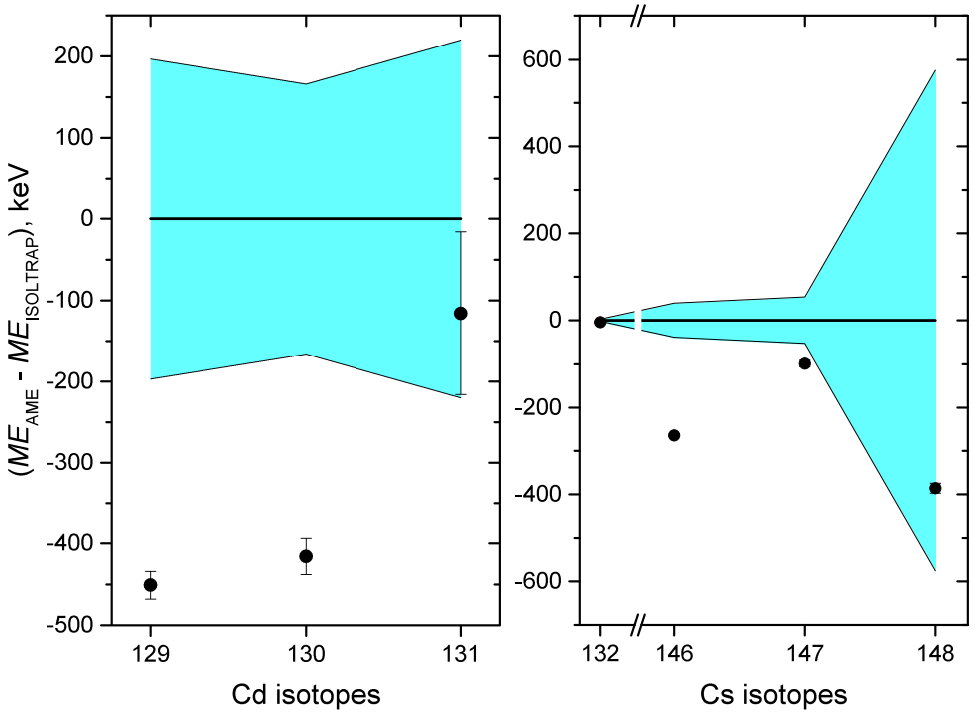

measurements reported here gave a result of $ME = -46\ 911(13)$ keV. The uncertainty in our experiment is smaller by a factor of 10.

To conclude this chapter, all mass-excess values for the newly determined masses have been compared to the already existing data or extrapolation tabulated in AME2012 [Aud+12a]. The comparison is presented in Fig. 4.11.

Chapter 5

Physics Interpretation

The results of the mass measurements described in the previous chapters have small uncertainties. Prior to the discussion of the astrophysical applications, it is worth comparing the newly determined masses to modern mass-model predictions. The main motivation for our comparison is driven by the fact that ^{130}Cd mass is an important nuclide along the path of the r-process. Its nuclear properties are determining whether the reaction flow proceeds quicker or slower, leading to changes in the abundance pattern. The lack of experimental data for the neighbouring nuclides, however, was a limiting factor for making definitive conclusions in the astrophysical calculations performed in the past [Dil+03; Lor+15a]. Hence, it is useful to compare the results of the mass measurements to nuclear mass models, that had been employed in astrophysical simulations. Thus one can obtain a clear picture of the changes due to nuclear masses in the region under investigation.

Numerous nuclear models were developed in the last seventy years, but only a small fraction can be used nowadays to satisfy the demanding requirements for r-process calculations. To evaluate the predictive power of global nuclear mass models, the root-mean square deviation between the theoretical mass predictions and the experimental data is calculated:

$$\sigma^2 = \frac{1}{n} \cdot \sum_{i}^{n} (M_i^{\mathrm{th}} - M_i^{\mathrm{exp}})^2. \tag{5.1}$$

In Table 5.1 summarised are the predictive powers of several nuclear mass models frequently used in astrophysical calculations.

5.1 Macroscopic-Microscopic mass models

Modern mass models can be divided into several categories. The first one comprises the so-called macroscopic-microscopic approach, where the models are based on the well-known Bethe-Weizsäcker formula [Wei35], representing the liquid-drop model of the nucleus. By applying the model to a nucleus with Z protons and N neutrons, we obtain for its mass ($M(N,Z)$) the basis equation for the macroscopic mass formulas:

$$c^2 \cdot M_{mac}(N,Z) = c^2 \cdot Z \cdot m_\pi + c^2 \cdot N \cdot m_\nu - a_v \cdot A + a_s \cdot A^{2/3} + a_c \cdot Z^2 \cdot A^{-1/3} + a_{as} \cdot \frac{(Z - A/2)^2}{A}. \tag{5.2}$$

Table 5.1: The root-mean square deviations for different mass models employed in the past in astrophysical simulations compared to AME2012, see Eq. (5.1).

Number of Isotopes Used	3048
Mass Dataset	RMS Average / MeV
HFB-24	0.550
FRDM12	0.570
ETFSI-2	0.690

where m_π and m_ν are the proton and neutron masses, respectively. The mass number is given as $A = N + Z$. The other constants are: volume parameter - $a_v = 15.85$ MeV, surface parameter - $a_s = 18.34$ MeV, Coulomb parameter - $a_c = 0.7110$ MeV and asymmetry parameter $a_{as} = 92.86$ MeV. The Coulomb and the surface energies are dependent on the deformation shape of the nucleus [MNK97]. The microscopic part added to the macroscopic formula are the shell ($E^{\text{shell}}_{\text{corr}}$) and the pairing ($E^{\text{pair}}_{\text{corr}}$) correction terms. Respectively for the total nuclear mass (M_{tot}) we obtain:

$$M_{tot}(N,Z) = M_{mac}(N,Z) + M_{mic}(N,Z) = M_{mac}(N,Z) + (E^{\text{shell}}_{\text{corr}} + E^{\text{pair}}_{\text{corr}})/\text{c}^2. \tag{5.3}$$

The $E^{\text{shell}}_{\text{corr}}$ term takes into account contributions of the single-particle energy levels. The nuclear corrections that are not considered in the shell correction term are included in the pairing one. The shell correction is calculated by using the method proposed by V. M. Strutinski [Str67] and the pairing can be treated with Bardeen-Cooper-Schrieffer (BCS) [BCS57] or Bogoliubov-Valatin theory [BOG58; Val61]. Currently, the most commonly used macroscopic-microscopic mass models are the Finite-Range Droplet Model, developed by P. Möller and co-workers [MNK97] and the Extended Thomas–Fermi with Strutinski Integral (ETFSI) model of J. Pearson [PNG96]. In the FRDM model there are 31 independent mass-related parameters included, out of which only 19 were effectively involved in the mass fit [LPT03], resulting in a rms deviation of $\sigma = 0.669$ MeV in comparison to AME2003 [WAT03]. With the increase of the computing power, new much finer optimisation and minimisation procedures became possible leading to a re-determination of many of the models parameters [Möl+12], yielding a considerably improved mass-accuracy $\sigma = 0.570$ MeV. The ETFSI model offers much stronger consolidation between the macroscopic and microscopic parts than the FRDM. Its macroscopic term for the binding energies emerge from a fourth-order approximation of the extended Thomas-Fermi expression, while the shell corrections are applied by using the Strutinsky theorem in its integral form [LPT03]. One of the last refinements of the ETFSI method yielded the ETFSI-2 mass table with a rms error of $\sigma = 0.690$ MeV.

Despite the success of the FRDM mass formula, the incoherent link between the macroscopic liquid-drop part and the shell-corrections term, as well as a few other deficiencies [AGT07], pose the question on the reliability of extrapolations to the neutron-rich nuclides of the nuclear chart. A much greater unity between the microscopic and the macroscopic considerations has been achieved in the semi-empirical models based on the ETFSI formalism. However, the ETFSI approximation has been made redundant by the microscopic Hartree-Fock calculations, but still remains superior for the far more complicated calculations of fission barriers [Mam+98].

5.2 Microscopic mass models

The second category of mass models is based on the nuclear many-body theory. It is inspired by the success of the independent-particle model and works on a microscopic level by considering nucleons as the relevant degrees of freedom. Different approaches exist for microscopic mass models. Generally speaking, it is assumed that nucleons move independently in a mean field created by all other nucleons. The focus here will be put on the mean-field (MF) model using the Hartree-Fock-Bogoliubov (HFB) method [LPT03; BHR03]. In this method the Schrödinger equation $H\Psi = E\Psi$ is solved with an effective Hamiltonian (H^{eff}):

$$H^{\text{eff}} = \sum_{i=1}^{A} T_i + \sum_{i<j} V_{ij}^{\text{eff}}, \tag{5.4}$$

where T_i is the kinetic energy operator for the i^{th} nucleon, and V_{ij}^{eff} is the interaction between the ij pair of nucleons. The total wave function (Φ) has a form of a Slater determinant ($\Psi = \det\phi_i(x_i)$), which corresponds to the antisymmetrized product of all single particles wave functions. The unknown single particle wave functions $\phi_i(x_i)$ are the eigenfunctions of the so-called Hartree-Fock equation, which is a single-particle Schrödinger-like equation:

$$\left(-\frac{\hbar^2}{2m}\nabla^2 + U \right)\phi_i = \epsilon_i\phi_i, \tag{5.5}$$

with U being a single-particle field, which is in general deformed and spin-dependent, and is determined by the effective interaction V_{ij}. The energy of the nucleus is then calculated by minimising the expectation value $< \Psi|H^{\text{eff}}|\Psi >$ with respect to arbitrary variations in the single-particle wavefunctions [PGC13]. The wavefuntions of the form Ψ containing no correlations will never be identical to the nuclear wavefunctions corresponding to the *real* nucleonic forces. Thus, if the HF method is to give the exact ground-state energy, the *real* forces shall be replaced by model *effective* forces that are not fit to the nucleon-nucleon scattering data. To some extend, the neglected correlations in the real nuclear wavefunctions have been compensated by the effective forces, when adopting the model wavefunctions Ψ.

The most popular form of effective forces is that of a Skyrme [Sky56; Sky58] type. In its usual form this force has ten free parameters, consisting of five separate zero-range terms: a static term (t_0), a momentum-dependent s-wave term (t_1), a momentum-dependent p-wave term (t_2), a static density-dependent term ($t3$) and a spin–orbit term (W_0). The Skyrme-force [VB72], has seen many parametrisations over the years [GCP09; GCP10]. The best mass tables of refitted Skyrme-based functionals, labeled HFB-24, HFB-25 [GCP13a] and the newly published HFB-31 [GCP16], were able to provide the rms deviations of 0.55 MeV, 0.54 MeV and 0.561 MeV, respectively.

5.3 Empirical separation energies and shell gaps

The one- and two-nucleon separation energies are important empirical observables of the atomic nucleus. They can be obtained as finite-difference formulas applied to the binding energies of neighbouring nuclides. The one-neutron separation energy (S_{n}) has an important role in nuclear structure (for example in the behaviour of skin in halo nuclei [HJJ95]) as well as in nuclear astrophysics (see Sec. 5.4). The general trend of the neutron separation energy is a smooth decrease with increasing the neutron number N for a fixed Z. The physical meaning is that it costs less

energy to remove neutrons with increasing N. This dependence reflects the approach towards the drip lines, beyond which the nuclei becomes unbound with respect to nucleon emission.

Nucleon separation energies are directly connected to the mass values of neighbouring nuclides. The mass differences are used in this context to filter and probe the nuclear structure effects. They serve as valuable mass filters to detect closed shells or intrinsic nuclear deformation. The one-neutron separation energy for atomic nucleus with Z protons and N neutrons is defined as:

$$\begin{aligned} S_{\mathrm{n}}(N,Z) &= BE(N,Z) - BE(N-1,Z) \\ &= (M(N-1,Z) + m_{\nu} - M(N,Z))c^2, \end{aligned} \tag{5.6}$$

where M is the mass of the nucleus and c the speed of light, BE corresponds to the binding energy. The magnitude of the odd-even staggering can be extracted from the S_{n}, which provides information about the binding energy of the last neutron (pairing effect). It is also useful to investigate the behaviour of the two-neutron separation energy. The latter is defined as finite difference of every second neighbouring isotope:

$$\begin{aligned} S_{2\mathrm{n}}(N,Z) &= BE(N,Z) - BE(N-2,Z) \\ &= (M(N-2,Z) + 2 \cdot m_{\nu} - M(N,Z))c^2. \end{aligned} \tag{5.7}$$

The general trend of the two-neutron separation energies in the region around $N = 82$ is presented in Fig. 5.1. For the $S_{2\mathrm{n}}$ one sees a smooth decrease with increasing N. When reaching a neutron number with a filled (closed) shell it exhibits a sudden drop. The sudden drop happens as it costs less energy to remove a pair of neutrons outside the closed shell. In the case of S_{n} one can see that the pairing effect is roughly half as big as the drop due to the shell closure. Hence, both effects are on the same order of magnitude. The one- and two-neutron separation energies are presented in Fig. 5.2 considering the newly measured masses for the Cd and Cs isotopic chains. Additionally, determination of the magnitude of the drop of the one-neutron separation energy, the so-called

Figure 5.1: Two-neutron separation energies in the region around ^{130}Cd. Isotopic chains from Zr up to Ba are presented. The sudden drop in the separation energies presents the closed neutron shell at $N = 82$.

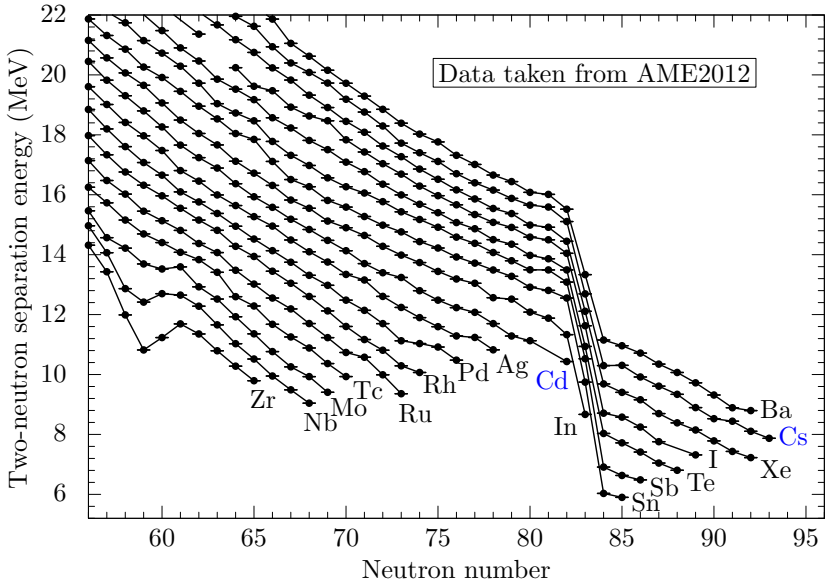

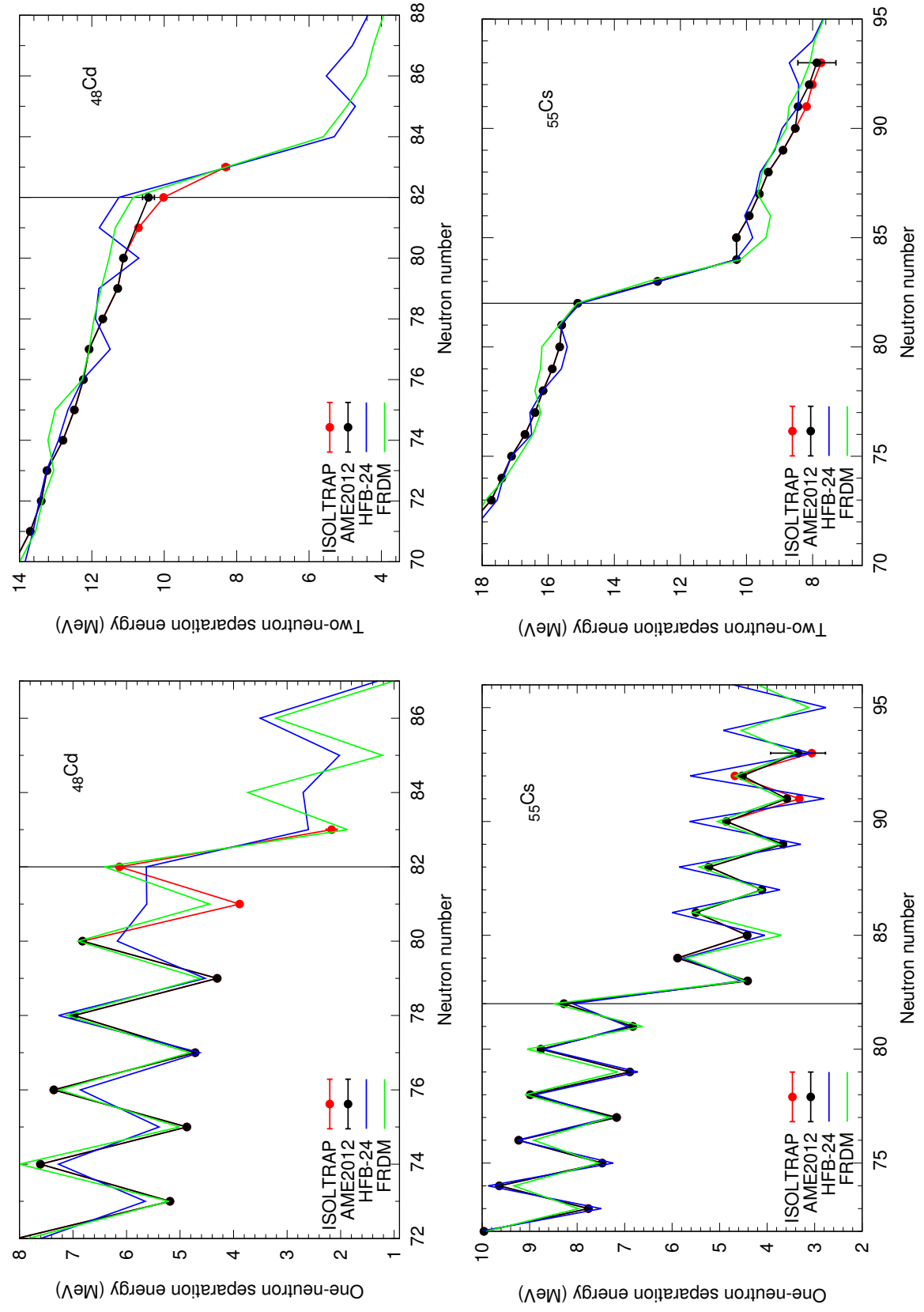

Figure 5.2: One- and two-neutron separation energy in the isotopic chains of cadmium and caesium. The black vertical lines correspond to the neutron closed shell $N = 82$, while theoretical values are given with colour lines, corresponding to FRDM [Möl+12] and HFB-24 [GCP13b]. The error bars if not shown are within the symbol size.

empirical one-neutron shell gap $D_n(N,Z)$ can be calculated [Bro13]:

$$\begin{aligned} D_n(N,Z) &= S_n(N,Z) - S_n(N+1,Z) \\ &= 2\cdot BE(N,Z) - BE(N-1,Z) - BE(N+1,Z) \\ &= (M(N+1,Z) + M(N-1,Z) - 2\cdot M(N,Z))c^2. \end{aligned} \tag{5.8}$$

This mass difference shows a sudden increase in energy at closed neutron or proton shells by varying Z or N. With such a mass filter new nuclear structure effects may be revealed (see for example [Ros+15; Wie+13]). Interesting discussion has arisen in the last years that pose the question on whether shell gaps for exotic magic (closed-shell) nuclei encountered along the path of r-process are significantly smaller (*quenched*) than those for stable magic nuclei. The first experimental insight relevant for the shell closure at neutron number $N = 82$ was given by beta- and gamma-decay spectroscopy on ^{130}Cd [Dil+03]. While these data were pointing to possible shell quenching of $N = 82$, the direct experimental proof was still missing. In agreement with the indications of the earlier beta-decay results, our precision mass measurements strengthen and quantify the decrease of the shell strength below ^{132}Sn, see Fig. 5.3. Specifically, we observe a reduction of the gap by 1 MeV between ^{132}Sn ($Z = 50$) and ^{130}Cd ($Z = 48$), also highlighting the doubly-magic character of ^{132}Sn.

Figure 5.3: The empirical one-neutron shell gap for $N = 82$. The black circles use the available data from the AME2012 [Aud+12a] and the red filled circle is the ^{130}Cd value calculated using the masses from this work. Theoretical values from two mass models are presented for comparison, the FRDM [Möl+12] and HFB-24 [GCP13b]. The error bars - if not visible - are within the symbol size.

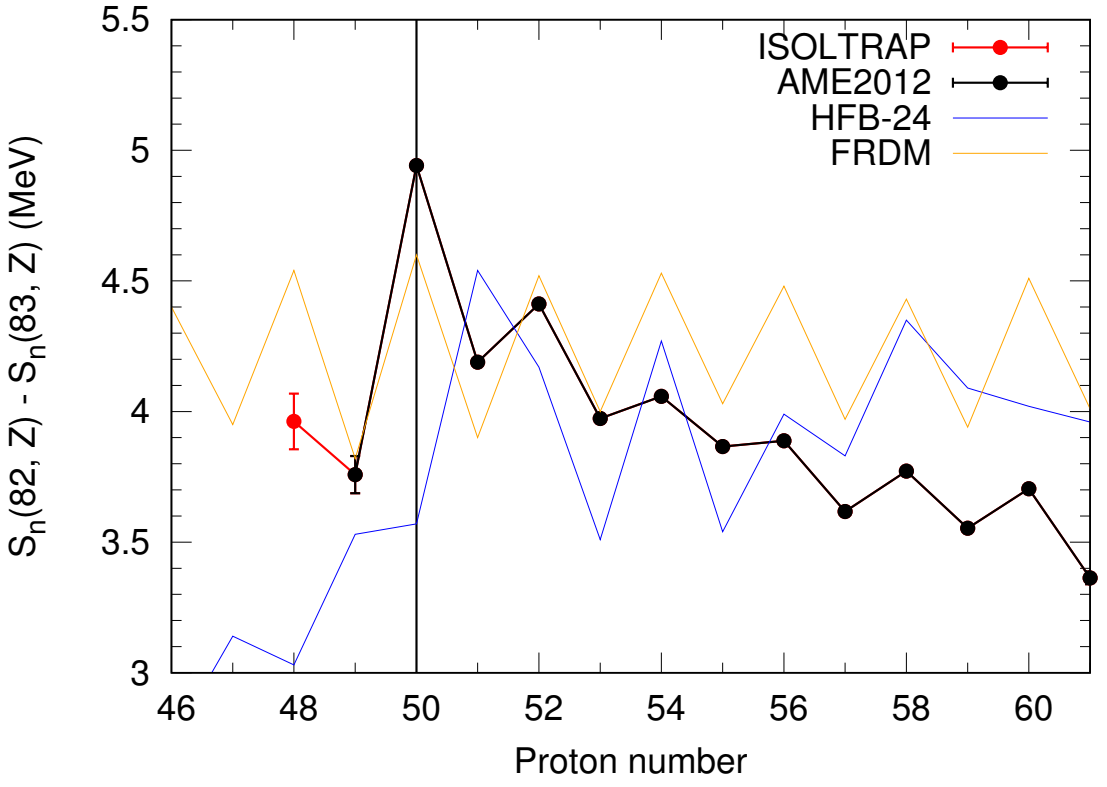

5.4 Basics of nucleosynthesis

The nucleosynthesis theory predicts that the formation of nuclear species with mass $A > 60$ occurs in nature as a consequence of neutron-capture processes and β^--decays. Evidence supporting this hypothesis is given by the patterns of the elemental abundances in heavy-elements. They are a main characteristics of the matter as observed in the Solar System [LPG09]. Features in the elemental abundances are found to be correlated with the positions of the neutron shell closures at neutron numbers $N = 50, 82$ and 126 [LW01]. In fact, the abundance peaks in the mass regions $A = 80 - 90$, $130 - 140$ and $190 - 210$, seems to reveal signatures of two distinct neutron fluxes. This has led historically to the definition of two nucleosynthesis processes that are associated with quite different astrophysical environments [AGT07].

The distinction is mainly given by the characteristic lifetimes for neutron capture (τ_n) and β-decay (τ_β) reactions. The condition $\tau_n > \tau_\beta$ ensures that while neutron captures proceed, the process path will remain close or near to the valley of beta stability, defining the slow-neutron capture process (s-process) [Bur+57; Wal+97]. The short beta-decay lifetimes in comparison to the neutron-capture's ones, constrains the s-process flow to the vicinity of the line of beta stability. For example in the region with $A > 209$ there are only unstable nuclei. Some of these might decay by alpha particle emission to nuclei with $A < 209$ and on a timescale shorter then the one of the s-process. The process is terminated at the last (semi)stable nuclide before the region of α-decaying nuclei, namely $^{209}_{83}$Bi. Along the s-process neutron-capture path, the small cross section for capturing neutrons away from the closed-shell configurations of $N = 50, 82$ and 126 give rise to the pronounced abundance peaks around strontium ($A = 88$) barium ($A = 138$) and lead ($A = 208$) [KBW89].

In the other limit $\tau_n < \tau_\beta$, known as rapid neutron-capture process (r-process) [Wal+97], in which one has large neutron densities, it follows that the successive neutron captures will proceed well off the valley of beta stability, i.e. into the very neutron-rich regions of the nuclidic chart. In this manner, the closed neutron shells at neutron numbers $N = 82, 126$ are encountered in the neutron-rich side at lower proton numbers and thus at lower mass numbers, in contrast to s-process. After exhaustion of the neutron flux the capture products decay to the valley of stability by beta decay. In this way the abundance peaks found at mass number $A = 130, 196$ are believed to be produced. These abundance peaks are found in fact at lower mass number compared to the ones found for s-process. The r-process mechanism is therefore believed to be operating in a stellar environment with a high neutron flux.

The Solar System distribution for r-nuclides abundance is classically obtained by subtracting from the observed elemental abundances, as presented in Fig. 1.3, those predicted to originate from the s-process. The s-process predictions are classically based on a parametric model, referred to as the canonical exponential model developed by D. Clayton *et al.* [Cla+61], and which has received some refinements over the years (e.g. [KBW89]). The model assumes that the stellar material composed only of iron nuclei is subjected to neutron densities and temperatures that remain constant over the whole period of the neutron irradiation. However, some of its basic assumptions deserve questioning. This concerns in particular the presumed exponential form for the distribution of the neutron exposures. In addition, the model makes it difficult to evaluate uncertainties of nuclear or observational nature. The shortcomings of the canonical model are cured to some extent by the so-called multi-event s-process model (MES) as described in [Gor99]. The r-process residuals plotted in Fig. 5.4 highlight the importance of ^{130}Cd isotope. This isotope is the progenitor of the top of the peak found at $A = 130$, which is produced only by r-process. Hence, the nuclear properties of this nuclide can affect the final elemental abundances.

Figure 5.4: Different symbols represent different levels of *r*-process contributions to the Solar System isotopic abundances. The label *s-dominant* nuclides are those predicted by the multi-event *s*-process model [PB93; Gor97] to have more than 50% of their abundances produced by the *s*-process. The contributions from *s*-process vary from 10 to 50% in the case of the *r-dominant* species, and does not exceed 10% for those labelled as *r-only* nuclides.

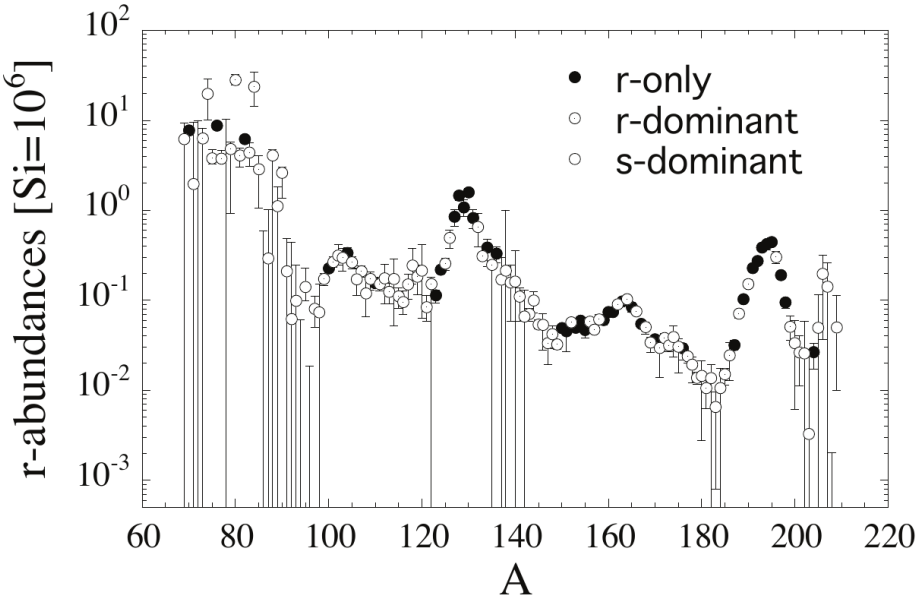

5.5 The element abundance equation

The importance of nuclear masses can be understood by looking closely to the principle of reaction network calculations given briefly in the following text using the derivation from [Lan99] and [AGT07].

The equation governing the change of the number densities $n(A, Z)$ of a nucleus with mass A and proton number Z has the form [Lan99]:

$$\frac{d}{dt}n_i = -\sum_j n_i n_j < \sigma v >_{ij} + \sum_{kl} n_k n_l < \sigma v >_{kl}, \tag{5.9}$$

where n_i is the number density of the ith nucleus, $< \sigma v >_{ij}$ is the product cross section and the relative velocity for an interaction involving species i and j. The summations runs over all reactions which either create or destroy the species i. Each species involved in the process obeys one such equation. All equations are coupled as the creation and the loss processes of a given species involves a knowledge of the abundances of all others. However, it is useful for numerical calculations to define a parameter that does not depend on the volume or the density of the astrophysical environment:

$$Y_i = Y(N, Z) = \frac{n(N, Z)}{\rho N_A} = \frac{n_i}{\rho N_A}, \tag{5.10}$$

where ρ is the mass density of the gas under consideration and N_A is the Avogadro's number and $n(N, Z)$ is the number density of the nucleus (N, Z) for equilibrium between the nuclides, protons

and neutrons and is expressed as:

$$n(N,Z) = \sum_r (2I_r + 1) \exp\left(-\frac{E_r}{kT}\right) \left(\frac{A\mathrm{u}kT}{2\pi\hbar^2}\right)^{3/2} \left(\frac{2\pi\hbar^2}{\mathrm{u}kT}\right)^{3A/2} \left(\frac{n_n^N n_p^Z}{2^A}\right) \exp\left[\frac{BE(N,Z)}{kT}\right], \quad (5.11)$$

where I_r and E_r are the spin and energy of the rth excited level, u is the atomic mass unit, n_n and n_p denote respectively the number density of free neutrons and protons.

With this substitution the connection between the reactions of type $i + j \rightarrow k + l$ which creates or destroys the ith nucleus can be written as:

$$\frac{d}{dt}Y_i = -\sum_j f_{ij} + \sum_j f_{kl}, \quad (5.12)$$

where the vector flow containing nuclei i and j in the entrance channel is given by:

$$f_{ij} = \frac{n_i n_j < \sigma v >_{ij}}{\rho N_A} = Y_i Y_j \rho N_A < \sigma v >_{ij}, \quad (5.13)$$

with $N_A < \sigma v >$ the cross section averaged over the Maxwell-Boltzmann distribution of the astrophysical plasma.

Considering r-process, in the build up of material the most important nuclear reactions are those capturing neutron (n, γ), photo-disintegration (γ, n) and beta decay. The full set of equations dictating the process are [AGT07]:

$$\begin{aligned}
\frac{dn(N,Z)}{dt} &= n(N-1,Z)\lambda_{n\gamma}^{(N-1,Z)} + n(N+1,Z)\lambda_{\gamma n}^{(N+1,Z)} \\
&+ n(N,Z-1)\lambda_{\beta 0}^{(N,Z-1)} + \sum_k n(N+k,Z-1)\lambda_{\beta kn}^{(N+k,Z-1)} \\
&+ n(N+2,Z+2)\lambda_{\alpha}^{(N+2,Z+2)} \\
&- n(N,Z)[\lambda_{n\gamma}^{(N,Z)} + \lambda_{\gamma n}^{(N,Z)} + \lambda_{\beta}^{(N,Z)}] \\
&- n(N,Z)[\lambda_{f}^{(N,Z)} + \lambda_{nf}^{(N,Z)} + \lambda_{\alpha}^{(N,Z)}] \\
&+ \sum_f q_{N_f,Z_f}(N,Z)\lambda_f^{(N_f,Z_f)} n(N_f,Z_f) \\
&+ \sum_f q^{\beta}_{N_f,Z_f}(N,Z)\lambda_{\beta f}^{(N_f,Z_f-1)} n(N_f,Z_f-1) \\
&+ \sum_f q^{n}_{N_f,Z_f}(N,Z)\lambda_{nf}^{(N_f-1,Z_f)} n(N_f-1,Z_f),
\end{aligned} \quad (5.14)$$

where $n(N,Z)$ is the number density of nucleus (N,Z); λ's are the reaction rates standing for: $\lambda_{n\gamma}$ for radiative neutron captures; $\lambda_{\gamma n}$ for the inverse photo-disintegration; $\lambda_{\beta 0}$ for β-decays; $\lambda_{\beta kn}$ for β-decays followed by the delayed emission of k neutrons; $\lambda_{\beta f}$ for β-delayed fission; λ_{β} = $\lambda_{\beta 0} + sum_k \lambda_{\beta kn} + \lambda_{\beta f}$ for the total β-decay rate; λ_{α} for α-decay; $\lambda_f^{(N_f,Z_f)}$ and $\lambda_{nf}^{(N_f,Z_f)}$ for spontaneous and neutron-induced fission. The last three terms in this equation correspond to fission of the synthesised heavy elements. Here the factor $q_{N_f,Z_f}(N,Z)$ is the probability for spontaneous fission of nucleus (N_f,Z_f) producing a fragment (N,Z). Fragmentation can similarly result from β-delayed or from neutron-induced fission. Fission of $Z < 80$ nuclei does not play significant role and thus only neutron captures, photo-disintegration and β-decay processes can be considered in the region around $A = 130$.

Assuming an equilibrium between (n,γ) and (γ,n) to be reached, the general equation for the statistical balance in r-process can be described by [HKT76; GA96]:

$$\log\frac{n(N+1,Z)}{n(N,Z)} = \log n_n - 34.07 - \frac{3}{2}\log T_9 + \frac{5.04}{T_9}S_n, \tag{5.15}$$

with S_n being the one-neutron separation energy (expressed in MeV), the $T_9 = T/10^9$ is the temperature in GK, and the n_n is the number density of the neutrons. In this framework also called *waiting point approximation* [SFC65], the evaluation of the final abundances depends only on three free parameters - temperature, neutron density and separation energy. In spite of the early success of this approximation by using easily tractable mathematics, in recent years this approach gave a way to dynamical r-process calculations including all the appropriate reaction processes.

One of the main goals of all r-process studies is to identify a realistic astrophysical scenario in which the nucleosynthesis of heavy nuclides can occur [Wal+97; AGT07]. This task is enormously challenging and its solution is still to be found. The core-collapse supernova of massive stars has been for a long time imagined as the best location for r-process. But new information from observational astronomy give confidence for the existence of even more exotic astrophysical sites, such as the coalescence of two neutron stars, which might bring new information on the subject. Before we focus on the results from the the r-process calculation and in particular on the influence of the newly measured masses of cadmium, a brief presentation of the astrophysical sites is given.

5.5.1 Neutrino-driven-wind core-collapse supernovae

Following the developments in the evolutionary theory of stars one could consider the inner regions of massive stars at the end of their lives (also known as a supernova explosion) as a plausible r-process site [WJT94b; WJT94a]. With the end of the hydrostatic burning stage in the core regions of massive stars, they have an onion-like structure with various shells still continuing the nuclear burning processes (hydrogen, helium, carbon, oxygen, neon and silicon burning). However, in the central region of the star there is no nuclear energy source that can sustain an equilibrium with the gravitational pressure from the outer layers [AGT07].

The characterisation of the core-collapse supernova (CCSN) mechanisms became better in recent years and could provide suitable conditions for the r-process. The findings show that the most-likely progenitor stars are those that develop during their evolutionary stage on the main-sequence, a core made of the elements around the iron group [WHW02]. These nuclides have the highest binding energy per nucleon from all known stable and unstable elements found in nature. At this point the outer layers of the star can no longer be supported by fusion burning, so that the core contracts and heats up. Temperatures of the star core reach values of about 4×10^9K [MA06].

If we consider single objects, restrictions for the total mass of the star that leads to CCSN are found to be in the mass range of approximate $9M_\odot$ to $100M_\odot$. But those limits are still quite uncertain and are most probably dependent on the stellar metallicity, mass-loss, nuclear reaction rates etc. [AGT07].

As mass continues to be added to the core, temperature increases even further and finally enables the electron capture process which reduces the star free energy [LM03]. In this process electrons from the atomic inner shells are captured by the protons in the nucleus leading to the creation of neutrons and emission of neutrinos. This process reduces the electron degeneracy pressure as well as the core temperature due to the unhindered escaping neutrinos.

The gravitational collapse of the iron core does not stop until the density of the material from which it is made of exceeds the one of the nuclear matter $\rho_0 \approx 1.5 \times 10^{14}$ g cm^{-3} [AGT07]. At this very moment, the inner most part of the core forms an in-compressible material, becoming the so-called proto-neutron star (PNS). This creates a shock wave, which propagates supersonically outwards into the in-falling outer layers of the star. This supernova shock loses energy by photo-disintegration of iron-group nuclei in the material encountered by the passing shock wave. Whenever the endothermic photo-disintegration is triggered, all of the nuclides found in that region of the shock wave are brought down to α-particles and/or even nucleons. The energy deficit creates then pressure decrease which is responsible for changing the state of the star from contraction into a collapse. The collapse may start for different masses of the core, depending on its equation of state. But at a first approximation these gravitational instabilities will take place near the Chandrasekhar mass limit, defined for cold white dwarfs $M_{Ch} = 5.83 Y_e^2$ [Cha67] with Y_e being the electron fraction [MFW96]. Consequently, this leads to a stalled shock, and the re-acceleration producing a successful explosion still remains an open question today [AT13]. The best studied mechanism up to date that can re-accelerate the shock is believed to be the transport of energy from the hot PNS to the shock by the escaping neutrinos. The energy that is deposited by these neutrinos via nucleon capture and scattering processes powers an outflow that expands with supersonic velocities and is known as the neutrino-driven wind [AT13].

The neutrino-driven winds are certainly interesting from a purely hydrodynamical point of view. The nucleosynthesis produced in this scenario has been studied in details in the hope that it could provide a natural site for dynamical r-process. The dynamical r-process considers a material, that is hot enough initially, which allows for a nuclear statistical equilibrium (NSE) to be achieved, expands and cools in a prescribed way for a given time [Sat74; HKT76]. This evolution is however highly parametrised. By applying the charge and mass conservation requirements, the initial NSE composition can be determined from the nuclear Saha equation for initial temperature and density. Such dynamical r-process occurring in a given mass element can be described by three parameters: the evolution of the entropy per baryon s_{k_B}, specifying the thermodynamics of the material, the evolution of the electron fraction Y_e (which specifies the composition of the material and is connected to the neutron excess), and the dynamic timescale (t_{dyn}) over which this material cools.

5.5.2 Compact binary mergers

Compact binary merger is a name given to compact stars in a binary system and was first proposed by Lattimer and Schramm [LS74; LS76]. This kind of systems can be composed of two neutron-stars (NS-NS) or black hole and a neutron star (NS-BH). The fate of these systems was predicted to be terminated by a catastrophic event after million or hundred of millions years of evolution. The occurrence frequency for our Milky way galaxy was calculated to be in the order of one NS-NS merger per 10^5 years [Bel+08]. However, these calculations are based on numbers with big uncertainties. During and after the coalescence event of such binary system, a fraction of the NS matter can be expelled into the interstellar medium. Because of the extremely neutron-rich initial state, the matter has been for long time speculated to be a possible site for the formation of r-process.

In the NS-NS case, during the last phases the two NSs develop long tidal arms stretching into a disc/torus made of cold material from their crusts [RD02; RL03; OJM07]. This is caused by the in-spiral process and of the centrifugal forces acting at the time of merging between the two NSs. Through its expansion, this material decompresses while releasing energy via nucleon recombination in nuclei and radioactive decay. An r-process is believed to accompany this decompression. In the

stages of the final collision, the matter is pulled out from the NS surfaces and consequently squeezed out from the massive NS remnant. Most of the dynamical ejecta are produced within less than 10 ms after the merging [AGT07].

In the calculations presented in the next section, a prompt collapse scenario is considered. The full description of the model (SFHO 13518) can be found in Ref. [Jus+15]. For this scenario the merging of a 1.35 $M_\odot$ NS and a 1.8 $M_\odot$ NS results in a direct collapse, and more specifically in the BH formation in only about one millisecond after the initial stars touch each other. The less massive NS is tidally strongly stretched before and during the merging and forms a massive tidal tail. This tidal tail winds around the BH, collides with itself after one orbit, and most of it ends up in a torus. The torus comprises a mass of about 0.1 $M_\odot$. When considering the prompt collapse scenario, the spatial distribution of unbound material is nearly isotropic with somewhat less matter being expelled towards the poles than close to the orbital plane [Jus+15].

5.6 Results from the r-process calculations

In the present application, the newly measured masses are used to estimate the neutron capture and photo-disintegration rates, but not the β-decay half-lives (experimental half-lives are available in this mass region [Aud+12b; Lor+15a]). The reaction rates are calculated using the TALYS reaction code [KHD08; GHK08]. The impact of the new masses on the reaction rates is illustrated in Fig. 5.5 where the Maxwellian-averaged radiative neutron capture and the photoneutron emission rates at $T = 10^9$ K are compared considering a set of nuclear masses from the AME2012, complemented with the masses measured in this work, or calculations from the HFB-24 model. In the ν-driven

Figure 5.5: Ratio of the neutron capture (n,γ) and photo-disintegration (γ,n) rates obtained with experimental masses from this work and the HFB-24 model.

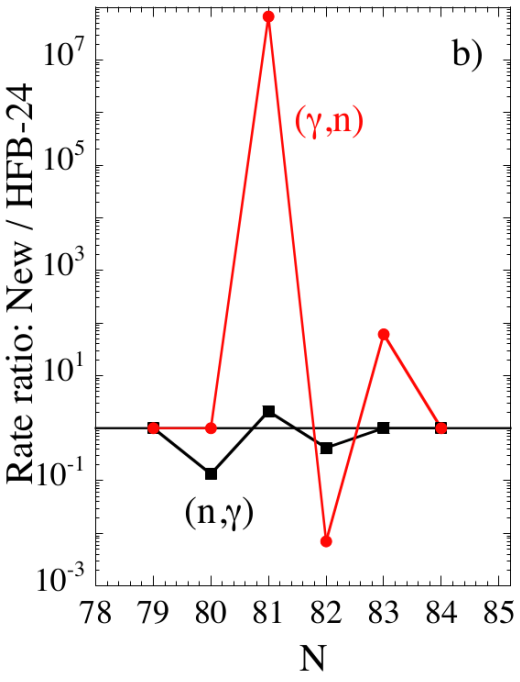

wind scenario, the adopted wind model corresponds to a subsonic breeze expansion with an entropy $s_{k_B} = 193$, electron fraction $Y_e = 0.48$, mass loss rate $dM/dt = 6\ 10^{-7}\ M_\odot\ \mathrm{s}^{-1}$ and breeze solution $f_\mathrm{w} = 3$ (see [AGT07; TJ97] for more details). For such conditions, the $A \simeq 130$ nuclei are

dominantly produced and the expansion is rather fast, so that the neutron irradiation responsible for the r-processing takes place at a rather low temperature and the final abundance distribution is sensitive to the adopted neutron capture rates. This specific event is chosen since it is found to strongly produce isotopes around the second r-process peak, as shown in Fig. 5.6. The modified rates based on the new Cd masses are seen to have an impact in the $A \simeq 130$ region. In particular, the odd-even effect between $A = 128$ and $A = 130$ is significantly modified due to the changes in the neutron separation energies, especially for ^{129}Cd (Fig. 5.5). This first example shows that the three newly measured masses affect directly the r-process abundance distribution in this specific ν-driven wind scenario, which could potentially explain the origin of the Solar System abundances of r-nuclei in the vicinity of the second $A \simeq 130$ peak despite all the remaining uncertainties still affecting the astrophysical modelling of this site.

Figure 5.6: Calculated distributions of the r-process abundance pattern obtained within the ν-driven wind scenario, see text for the conditions of the calculations and [AGT07; TJ97] for further details. The blue squares are obtained from AME12 (complemented with HFB-24 masses for experimentally unknown isotopes) and the corresponding rates, while the red circles include the new Cd masses. For comparison, the r-process Solar System abundance distribution is shown by open circles. Both theoretical distributions are normalised by the same factor, such that the mass fraction of ^{128}Te obtained with the new Cd masses reproduces the solar value.

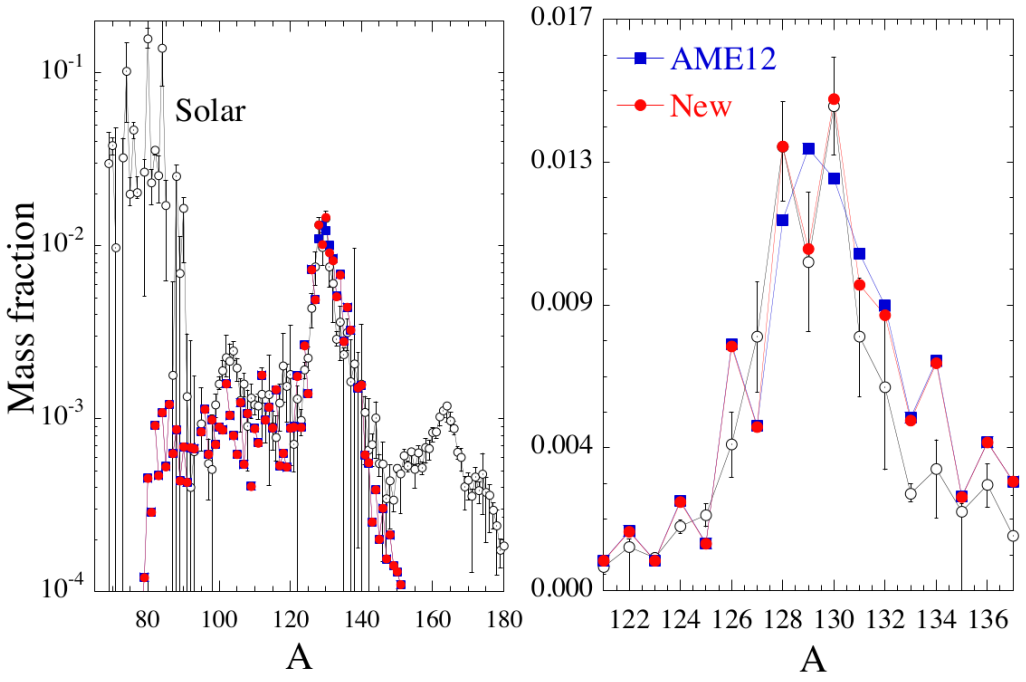

For the compact binary merger scenario, we do not study the nucleosynthesis in the matter that is dynamically ejected by tidal and pressure forces during the merging of the two compact objects, but rather in the neutrino and viscously driven outflows generated during the post-merger remnant evolution of the relic BH-torus systems. Indeed, in the prompt ejecta, large neutron-to-seed ratios drive the nuclear flow into the very heavy-mass region along a path close to the neutron drip line, leading to multiple fission recycling at relatively low temperatures and essentially $A > 140$ nuclei are found to be produced. In contrast, the BH-torus ejecta produce heavy elements in the range from $A \sim 80$ up to thorium and uranium with a significant contribution to the $A \simeq 130$

Figure 5.7: Same as Fig. 5.6 but showing the final r-process abundance curve for viscously driven ejecta from a $3\,M_\odot$ BH - $0.1\,M_\odot$ torus system model.

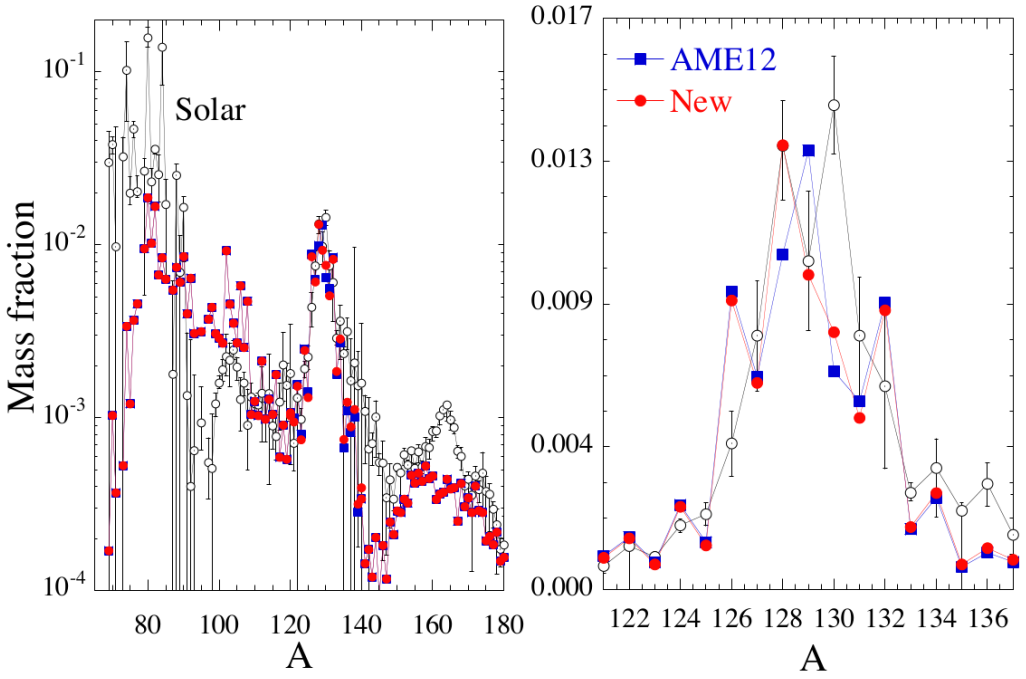

abundance peak. We consider here a representative sample of 310 trajectories ejected from a system characterized by a torus mass of $0.1\ M_\odot$ and a $3\,M_\odot$ BH (corresponding to the M3A8m1a5 model of Ref. [Jus+15]). The total mass ejected from the BH-torus system amounts to $2.5 \times 10^{-2} M_\odot$, and the outflow is characterised by a mean electron fraction $\bar{Y}_e = 0.24$, a mean entropy $\bar{s}/k_B = 28$ and a mean velocity $\bar{v} = 1.56 \times 10^9$ cm/s.

5.7 Conclusions and Outlook

In the present work, the masses of neutron-rich nuclides $^{129-131}$Cd and $^{132,146-148}$Cs were determined with high precision using the mass spectrometer ISOLTRAP. Due to the relatively clean samples and the good production yield from ISOLDE, it was possible to determine most of their masses by using the time-of-flight ion-cyclotron resonance technique in a Penning trap. The multi-reflection time-of-flight mass spectrometer (MR-TOF MS) was used as a beam-analysis tool, however, in the case of ^{131}Cd nuclide it was used as a primary device for the mass determination, reaching a precision of 100 keV. Reduction of the mass uncertainties was possible down to few keV for the masses determined by the Penning trap, which was not the case in previous attempts. In four cases out of the performed measurements, $^{129-131}$Cd and ^{148}Cs, the masses were measured directly for the first time.

In the case of Cs nuclides, we observed a displacement of the kink in the two-neutron separation energies found at $A = 146$. Such kink in the separation energies could originate from structural changes of the intrinsic ground state. Deformation region is expected by theory to exist in the very neutron-rich region of the nuclidic chart at about $A = 155$. The present measurements are,

however, only at the outskirts of the region where huge structural changes are not expected to be observed.

The new masses for Cd show a significant reduction of the $N = 82$ shell gap for $Z < 50$. The new data provide additional constraints for nuclear theory, considering the diverging predictions of mass models concerning the $N = 82$ empirical one-neutron shell gap for $Z < 50$. Results from the astrophysical simulations clearly show that the new mass measurements bring reliability to the description of the r-process nucleosynthesis by reducing the uncertainty from the nuclear-mass input. Given the large volume of experimental and theoretical data that are required for performing astrophysical calculations, it is remarkable that only three masses do make an observable impact on the predicted abundances. These results highlight the importance of precision measurements in this region of the nuclear chart.

The precision mass-measurement program at ISOLTRAP foresees in the future experiments extending the data presented in this thesis. This includes measurements of the ^{132}Cd, ^{132,133}In and $^{125-129}$Ag nuclides. The nuclear astrophysics community will benefit from these measurements, by relying in their r-process simulation on precise nuclear mass data. This will lead to more decisive conclusions out of the simulations concerning the origin of heavy elements. Furthermore, the experiments will provide new precision data that will help constrain the nuclear mass models.

Furthermore, new technical developments at ISOLTRAP aim to improve the measurement technique. A novel mass measurement method known as position-sensitive ion-cyclotron-resonance (PI-ICR)[Eli+13], developed for short-lived nuclides with half-lives well below one second was shown to reach a relative mass uncertainty at the 10^{-9} level. The method is based on the projection of the radial ion motion in a Penning trap onto a position-sensitive detector. Compared with the presently employed TOF-ICR technique, the novel approach is 25-times faster and provides a 40-fold gain in resolving power. This PI-ICR technique is currently being implemented at ISOLTRAP. An improvement of this scale will enable new possibilities for precision mass measurements of nuclides beyond ^{132}Cd with very short half-lives and low production yield at the ISOLTRAP experiment.

Appendix A

Magnetic field at ISOLTRAP - mapping and alignment

Measurements of the strength of the magnetic field at different positions from the centre of the magnets are called "Magnetic Field Mapping". This procedure in the maintenance of a Superconducting Magnet (SUMA) is done once the magnets are energised and shimmed. The ISOLTRAP experiment is equipped with two superconducting magnets, for short named Upper and Lower SUMA. The purpose of this procedure is to understand the position of the magnetic field centre of the magnet and the degree of homogeneity around it. The magnetic field mapping has been divided into two main tasks (divided by the usage of different measurement instruments).

A.1 Nuclear magnetic resonance instrument (NMR probe)

We mounted a NMR probe on a holder placed on top of the magnet's bore. The holder is a customised CF150 flange with which it is possible to rotate the probe on a 360 degrees, as well as displacing it axially on a radius of up to 35 mm. We used during the measurements an Oxford Tesla-meter PT 2025 to read-out the signals from the NMR probe. The instrument has implemented functions to automatically scan and locks on a NMR frequency signal and to display the measured field in Tesla units. Each measurement was transferred and recorded into a PC for a subsequent analysis. With the NMR probe we determined the centre field along the z-axis. Furthermore, we have measured radially the field for different radii and angles thus producing the colour map of the field shown in Fig. A.1b. In total 572 measurements for the Upper Magnet and 450 measurements for the Lower Magnet were performed. Each recorded measurement has been accomplish by averaging 5 single measurements. After the mapping of the Upper Magnet, we have observed a second order z-dependent field term in the magnetic field. The dependence is illustrated in Fig. A.2 and represents the magnetic field strength along the z-axis. We have concluded that the observed effect is produced by the room temperature shim coil. As the magnetic field drifts to lower values due to the normal decay of the current in the superconducting coils, the fixed value of the current in the shim coils creates a discrepancy with respect to previously optimised settings. The optimal value of the current applied on the shim coil up to the date of this thesis equals to I=237 mA.

Figure A.1: Distribution of the magnetic field of the two superconducting magnets in the corresponding central (z = 0) plane.

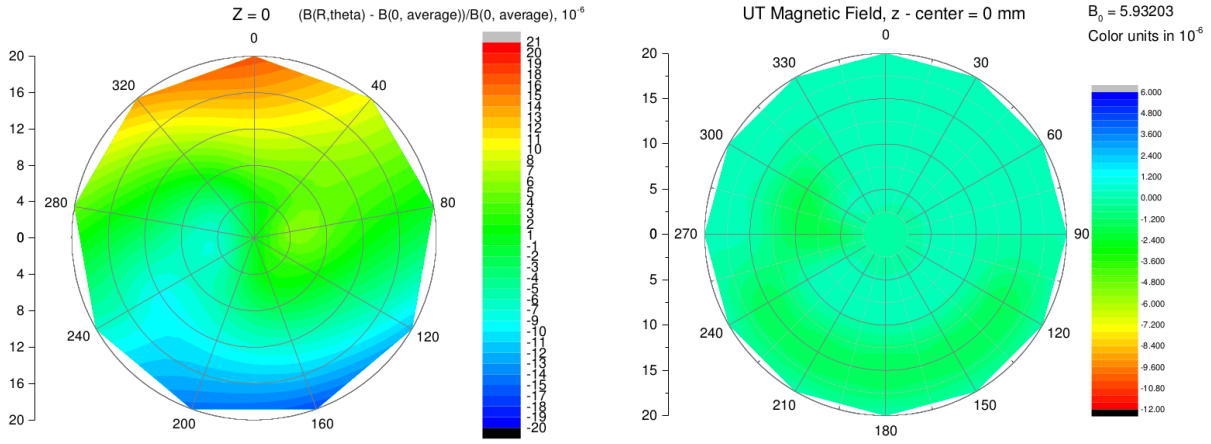

(a) Lower Magnet *Credits: Dimitry Kisler* **(b)** Upper Magnet

The variation of the magnetic field in a cylinder volume of 20 mm (hight) by 25 mm (diameter) for the Upper SUMA equals to $\Delta B = 16\ \mu T$ and for the Lower SUMA considering volume of 40 mm (height) by 20 mm (diameter) to $\Delta B = 36\ \mu T$.

A.2 3-axis Magnetometer (Hall probe)

The gradient of the magnetic field plays an important role in the determination of the cyclotron frequency as well as in the transport of the ions into, along and out of the Penning-trap system. For the first time we have measured the field along the z-axis for the complete vertical beam line. The result is shown in Fig. A.3. These values are now the most reliable and can be used in simulations of ions transported through the system using software packages such as SIMION [SIM]. Previous

Figure A.2: This figure shows the dependence of the magnetic field along the z-axis versus the current flowing through the room temperature shim coil.

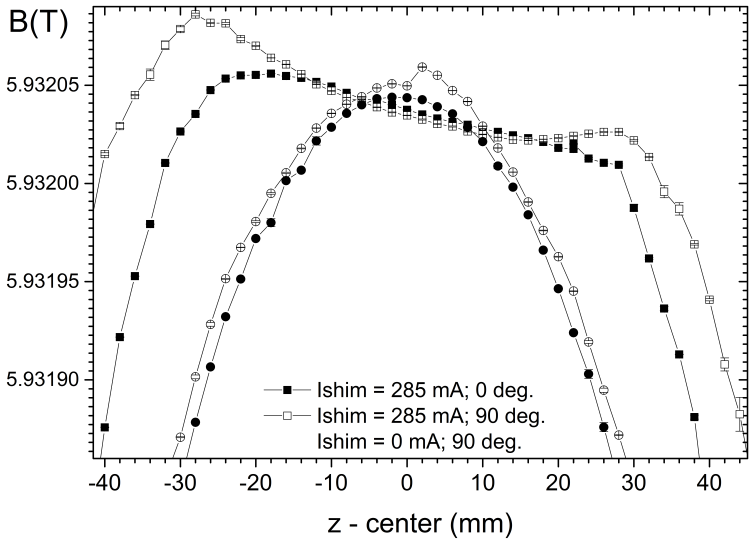

measurements as well as previously used simulations are presented for comparison in Fig. A.4. In our measurements a 3-axis Hall probe (model THM-1176-HF) was used, handling magnetic fields up to 20 Tesla. A LabView program controlled the device through a GPIB connection with a PC. Each measured value was computed by 10000 averaged single measurements (build-in function of the device), which reduced the statistical uncertainty to a sub mT range. The systematic studies on the probe showed an 0.1% uncertainty on the measured value of the magnetic field.

Figure A.3: Complete magnetic field measurement along the z-axis covering the vertical beam line of ISOLTRAP. The zero in the horizontal axis was chosen to be the place of the centre of the precision Penning trap.

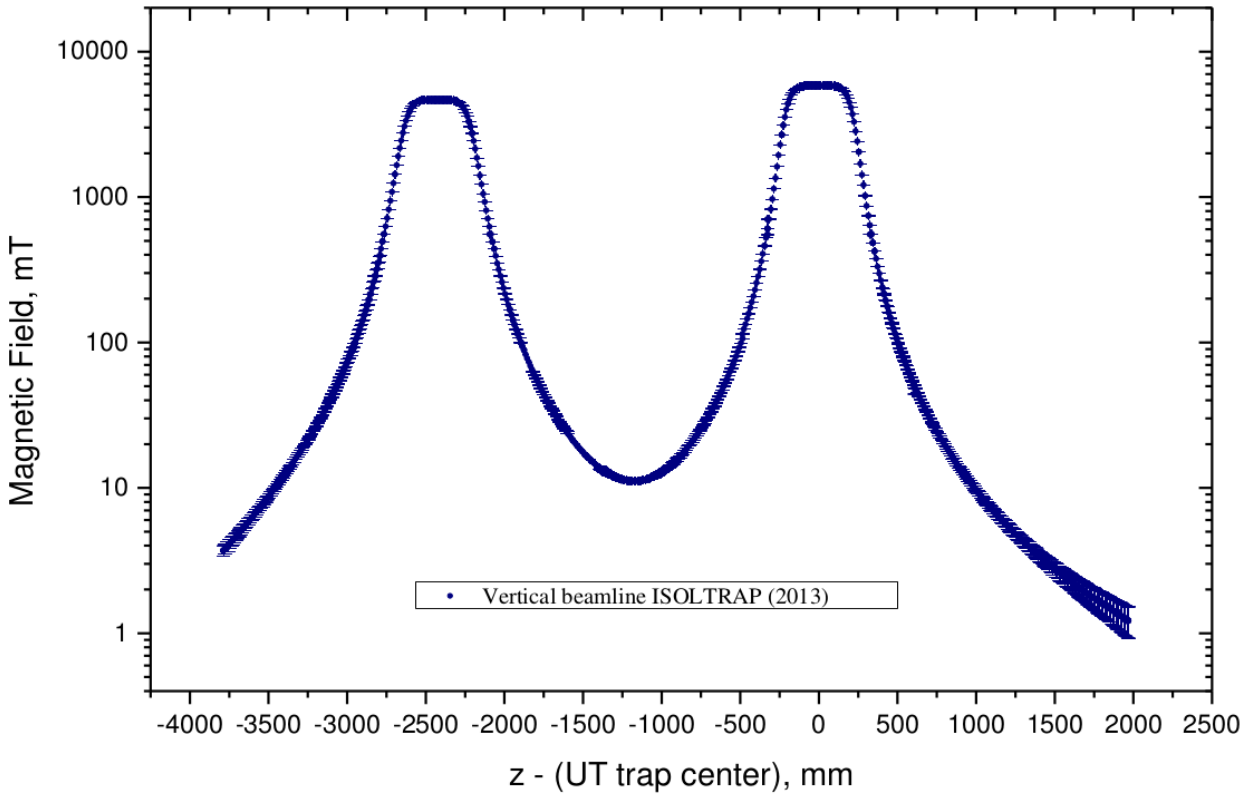

A.3 Alignment of the Magnetic Field

In this section we will describe the alignment procedure of the SUMA tubes with respect to the geometric axis. We are using electron guns as tool of choice as the electrons are light and they follow the lines of the magnetic field.

A.3.1 Electron guns - Operation and Detection

The initial electron beam is created by electrons emitted from a heated filament visible in Fig. A.5a. Two disks plates with apertures of 0.2(0.1) mm placed close on both sides of the filament, create the initial shape of the electron beam. The detectors, that are places on both far ends of the SUMA tube, are collecting the electrons (see Fig. A.5b). Each detector is composed by 10 aluminium

Figure A.4: The magnetic field strength along the z-axis starting from the centre of the Precision trap. For comparison the old measurements are presented as well as the previously used values for simulations in SIMION [SIM].

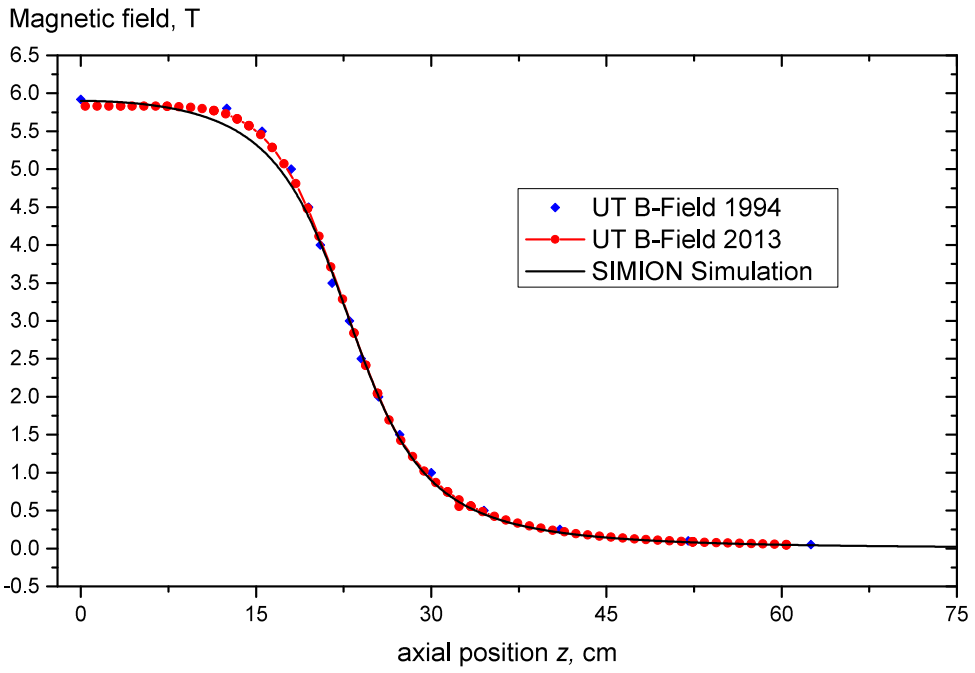

pieces (5 for output signal and 5 to limit the final spot) and 3 insulator pieces for separating the different detection layers. All together they are forming a Faraday Cup like plate-array detector. Each detector is comprises of 3 layers for detecting electrons arranged in the following way:

- For the first layer, two plates are arranged with a distance of 1 mm parallel to one another in a preferred direction.
- The second layer is arrange with smaller opening and perpendicular to the first layer. Thus, the distance between the plates becomes smaller the deeper down the layers are lying.
- The third and the last layer has the smallest size between two plates and was chosen to be 0.6 mm.

The final dimensions of the square between the detector plates have to be larger than the diameter of the dispersion of the electron beam. The rate of the detected electrons is finally monitored via a sensitive Ampere-meter (the current is in the pico Ampere range). Due to the change of the magnetic field from the centre of the SUMA to the detector's position, one will observe an increase in the diameter of the electron beam (dispersion). This raises the question of which is the best position, where the detector should be placed due to the fixed size of its last detection layer. To calculate this dispersion of the electron beam (or in other words the position from the centre of the trap to the detector) one should consider two effects:

- the gradient of the magnetic field towards detector's position
- the helical motion of electrons around the field lines [Sin].

Figure A.5: Different parts of an electron gun

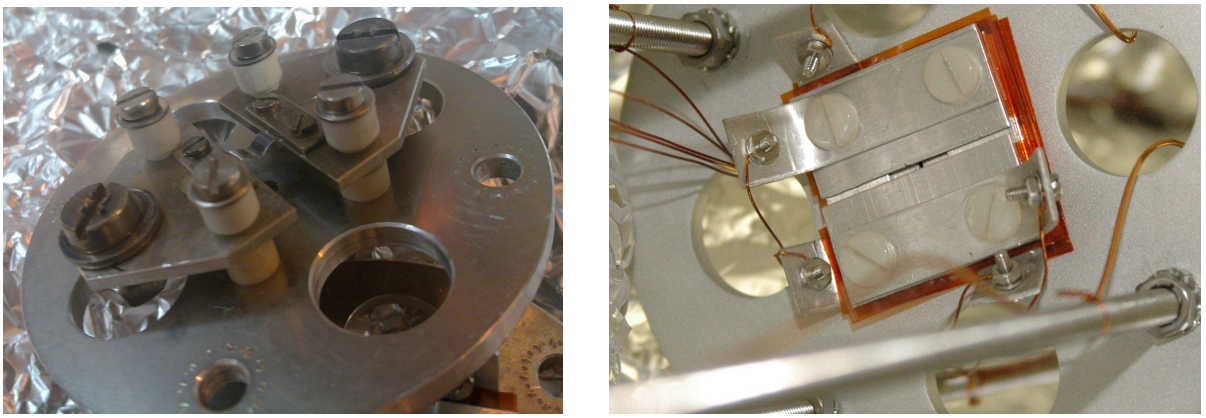

(a) Filament **(b)** Detector

Let's first consider the helical motion of the electrons emitted from the filament. A simple relation can be expressed with the equation:

$$R(z) = \frac{m_e v_e \sin\theta}{q\mathrm{B(z)}} \tag{A.1}$$

where m_e,v_e are the mass and the velocity of the electrons,respectively; B(z) the magnetic field along the z-axis; q the charge state and θ the angle between the initial electron velocity and the z-axis. The resulting increase due to this effect is displayed in Fig. A.6. Interpreting the plot we see that the increase of the radius of the electron beam coming from this motion is in the range of microns and it will not affect the alignment procedure. To estimate the effect of the gradient of the

Figure A.6: Increase of the electron beam radius in a magnetic field due to the helical motion.

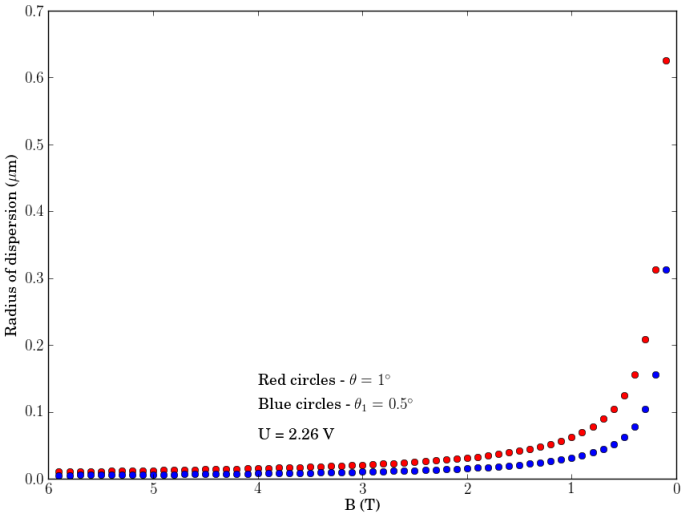

magnetic field to the dispersion of the electron beam, we will use the Gauss law for conservation

the flux of the magnetic field lines, crossing the area A:

$$\oint \mathrm{B} \cdot \mathrm{dA} = 0 \tag{A.2}$$

which can be rewritten, considering a bunch of magnetic field lines emerging from the magnetic centre, as:

$$\oint \mathrm{B_0} \cdot \mathrm{dA_0} - \oint \mathrm{B_1} \cdot \mathrm{dA_1} = 0 \tag{A.3}$$

where $\mathrm{B_0}$, $\mathrm{A_0}$, $\mathrm{B_1}$, $\mathrm{A_1}$ are the magnetic field and the area at the centre of the SUMA and at the position of the detector, respectively. We will consider here the field only in z direction, which will allow to be taken out of the integral. All what is left is a surface integral of a circle:

$$\oint \mathrm{dA_i} = \pi \mathrm{R_i^2} \tag{A.4}$$

where i is indicating the radius of the electron beam at the centre of the SUMA (0) and at the detector's position (1). Using equation A.3 and A.4 we can derive the next formula:

$$\mathrm{B_1} = \mathrm{B_0} \cdot \frac{\mathrm{R_0^2}}{\mathrm{R_1^2}} \tag{A.5}$$

Having in mind the values for the initial electron beam size ($\mathrm{R_0}$ = 0.2/0.1 mm) and the last detection layer ($\mathrm{R_1}$ = 0.6 mm) we can calculate the magnetic field at the position of the detector, which ensures that the electron spot size covers completely the last detection layer opening: - $\mathrm{B_1}$ = 0.66 T if we assume $\mathrm{B_0}$ = 5.93 T. Then, using the axial field plot (see Fig. A.3 and Fig. A.4) we can determine the optimal position for the detector e.g $\mathrm{R_1} \approx 300$ mm.

Figure A.7: The magnetic field profile of the Helmholz coils used in the test.
Credits: Frank Wienholtz

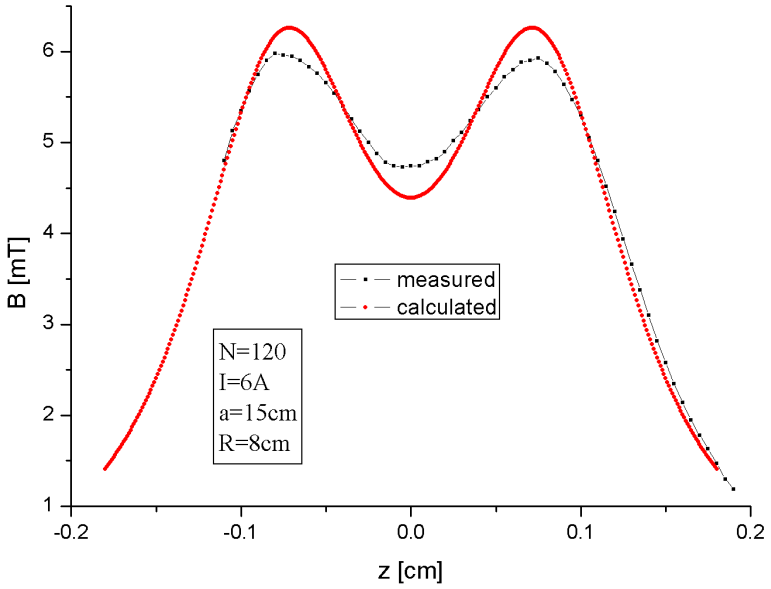

A.4 Electron gun Test Bench

In order to test the components of the electron gun before the actual maintenance operation (filaments, feedthroughs, detectors and cabling), an Electron Gun test bench was assembled. All components used at the test bench are given in the list below:

- Beam line - a combination of CF150 cross flange and Helmholz coils mounted around a CF100 cross flange (*Credits for the Helmholtz coils: Frank Wienholtz*)
- Vacuum - an oil roughing pump, a turbo-molecular pump (Pfeiffer Vacuum TPU 180 H - after a crash of the controller exchanged with a turbo-molecular pump Laybold Vacuum Turbovac TMP 151), a Penning gauge
- Electronics - filament Power Supply (TOE 8852), coils power supply (Xantrex XFR 12-100), acceleration DC power supply (EA-PSI 6150-01), ampere-meter (Keithley 6485)

A.4.1 Electron guns for Upper & Lower SUMA

The construction of both electron guns is based on the same principle. Due to the differences in the diameters of the SUMA tubes of the Upper and the Lower SUMA, each electron gun was adapted to be mounted either on the Upper SUMA (CF100) or on the Lower SUMA (CF150). Both Lower and Upper electron guns consist of: Filament, 2 plates with apertures (holes) of 0.2 mm in the centre, [1] 2 segmented detectors, 2 plates for mounting the detectors, CF100/CF150 flanges with feedthroughs. Preparation needed before the test are listed below:

- **The filament** of the Upper electron gun was exchanged with a 12 μm thick Tungsten foil A.5a.
- **The rods** were made in such a way that they match our Test Bench size.
- **The detector's plates** were dismounted and cleaned. After that they were re-build and the estimated size of the last layer's detection surface is approximately 0.036 mm^2.

A.4.2 Test results

The pressure inside the chamber of the electron-gun test bench was 5.10^{-7} mbar. The filament has been placed at the centre of the magnetic field, produced by the Helmholz coils. Then the filament was heated by a DC Power supply. One of the filament's electrodes has been floated with potential of $\mathbf{V}_{float}$ **= - 50 V** to accelerate the emitted electrons towards the detectors. The electrons from the filament were collimated in their path to one of the two detectors (using the 0.2 mm collimator) and left uncollimated on the other. The idea behind such mounting was to probe if the collimator aperture is blocked and electrons can not pass through it. As a consequence of this arrangement, the detected electrons on the unblocked side was greater then the collimated one. The detectors were mounted at different distances with respect to the filament in order to record the intensity variations of the electron beam at different positions. The magnetic field of the coils is not uniform, but for this primary test it was sufficiently homogeneous. The magnetic field profile is presented in Fig. A.7. After this test we have concluded that the aperture of the filament's plate can collimate electrons (see Fig. A.8a) and the detectors are working properly for the alignment of the SUMA tubes.

[1] one of the plates for the Upper electron gun was re-manufactured with diameter of the hole 0.1 mm

Figure A.8: Detected signal from all detection layers versus the applied current on the filament

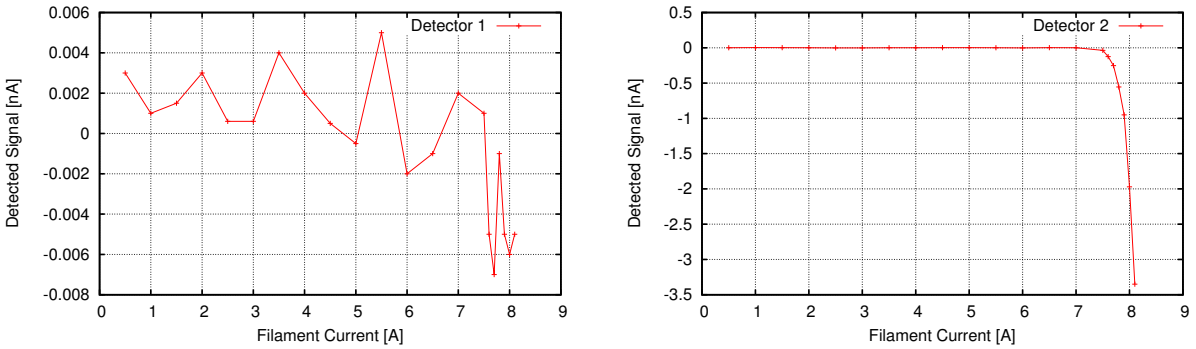

(a) Detector 1

(b) Detector 2

A.5 Final alignment

The alignment was performed once the mapping of the magnetic field procedure ended. The electron guns were prepared for the mounting in the SUMA tubes by using the available information for the strength of the magnetic field. The latter information, allowed calculation of the distance at which the detectors have to be placed to achieve a relative mass precision of about 10^{-8} or better.

Both SUMA tubes are fixed in place by using the so-called *Kardaniken* support, which is placed onto thick metal plates. This type of configuration allows a precision movements of the tube. Thus, by fine adjustments of the distances between individual components of the Kardaniken, a very precise movement of the tube is achieved. In this way the angle between the magnetic field axis and the geometric z-axis of the tube is minimised. Multiple measurements with different accelerating voltages were carried out. The initial kinetic energy of the electrons was chosen to be $E_{kin} = 30$ and 50 eV.

One can calculate using Eq. (2.29) the frequency shift originating from a misalignment due to tilting angle of 1 mrad to be about 2 mHz frequency shift for magnetron frequency of 1087 Hz. The relative mass uncertainty for the magnetic field of the precision Penning trap and ions with a mass $A = 100$ is then shown to be 2×10^{-9}. The outcome of this work was successful and the required precision was achieved for both SUMA. Schematic drawing of the electron gun placement inside the SUMA tube is shown in Fig. A.9. The final distances used throughout the alignment procedure are summarised in Table A.1.

Table A.1: The final dimensions used in the alignment procedure.

SUMA	a (mm)	b (mm)	c (mm)	d (mm)	e (mm)
UT	1133	955	765	30	190
LT	1044	975	620	20	76

Figure A.9: Schematic drawing of the Upper and Lower magnets and the positions of the components of the e-gun.

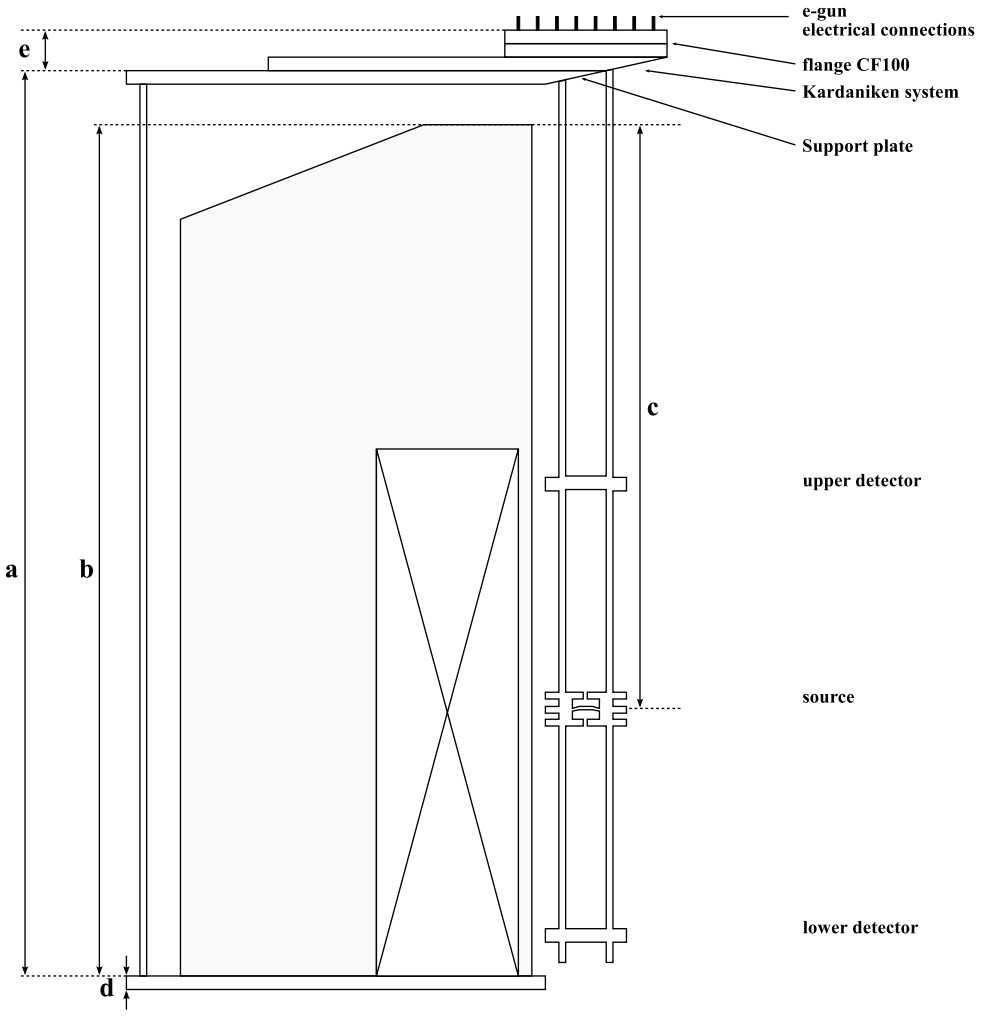

Appendix B

Experimental spectra and Analysis results

B.1 Results from the 2014 experimental run

B.1.1 ToF-ICR for ^{129}Cd isotope

(a) 129Cd_100ms_002.dat

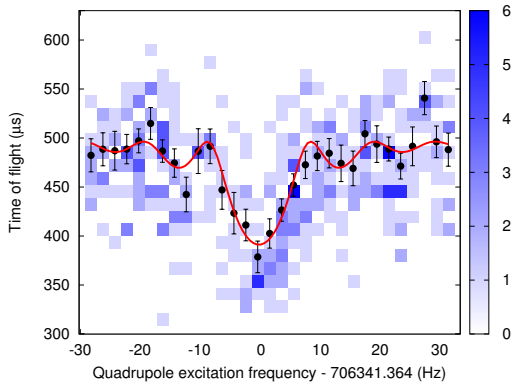

(b) 129Cd_100ms_005.dat

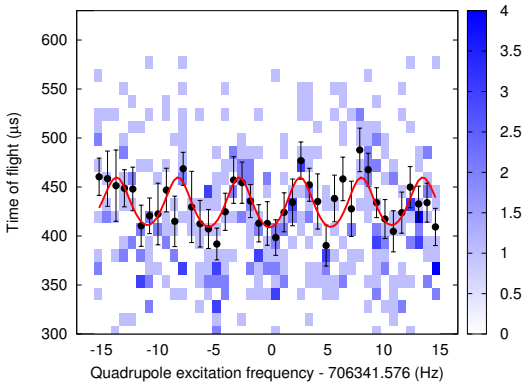

(c) 129Cd_100ms_007.dat

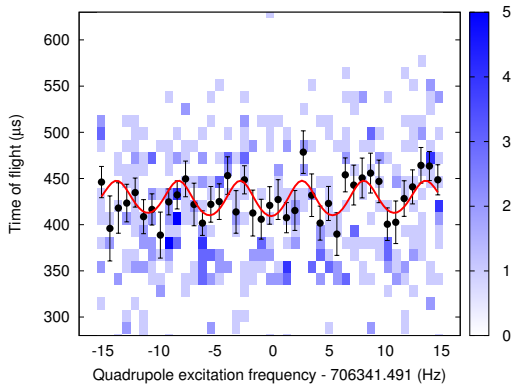

(d) 129Cd_100ms_009.dat

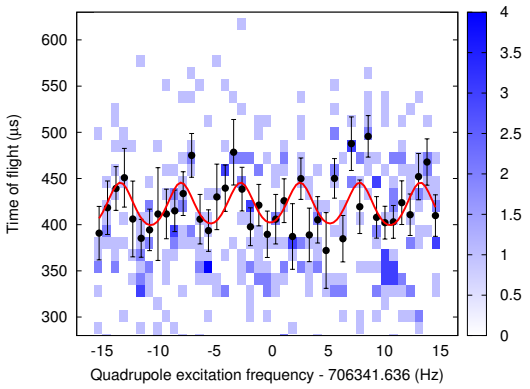

Table B.1: Results from the ^{129}Cd data analysis for the main floating parameters.

DataFile	129Cd_100ms_002	129Cd_20_160_20ms_005	129Cd_20_160_20ms_007	129Cd_20_160_20ms_009
Nr.Ion	413	383	417	335
$\nu_c(Hz)$	706341.364(0.348)	706341.576(0.157)	706341.491(0.203)	706341.636(0.208)
ρ_-	0.51(0.048)	0.273(0.056)	0.268(0.237)	0.249(0.046)
Conv	0.994(0.142)	0.859(0.345)	0.603(0.758)	1.199(0.22)
χ^2/N_{DoF}	0.777	0.703	0.822	1.046
ToF effect	21.195	11.117	8.564	9.725

B.1.2 ToF-ICR for ^{130}Cd isotope

(e) 130Cd_100ms_113.dat

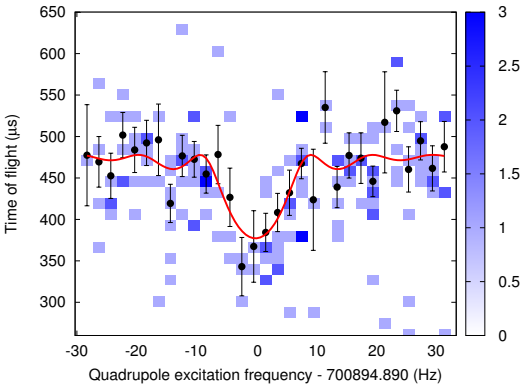

(f) 130Cd_10-80-10ms_116.dat

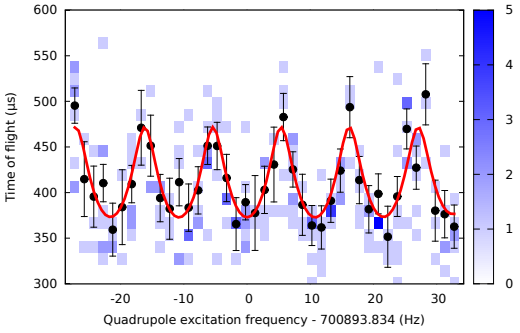

Table B.2: Results from the ^{130}Cd data analysis for the main floating parameters.

DataFile	130Cd_100ms_113	130Cd_10-80-10ms_116	130Cd_10-80-10ms_121
Nr.Ion	153	206	229
$\nu_c(Hz)$	700894.8898(0.7526)	700893.8336(0.2016)	700894.0398(0.1652)
ρ_-	0.528(0.163)	0.477(0.063)	0.604(0.085)
Conv	0.743(0.441)	1.034(0.174)	0.918(0.164)
χ^2/N_{DoF}	0.899	0.669	0.433
ToF effect	21.068	20.968	24.471

B.2 Results from the 2012 experimental run

B.2.1 ToF-ICR for ^{132}Cs isotope

Table B.3: Results from the ^{132}Cs data analysis for the main floating parameters.

DataFile	132Cs_100-1000-100ms_091	132Cs_100-1000-100ms_095	132Cs_100-1000-100ms_097
Nr.Ion	1604	1168	1420
$\nu_c(Hz)$	686656.0199(0.0033)	686656.0078(0.0044)	686656.0172(0.004)
ρ_-	0.657(0.028)	0.634(0.032)	0.611(0.029)
Conv	1.048(0.039)	0.967(0.059)	0.981(0.05)
χ^2/N_{DoF}	0.466	0.456	0.636
ToF effect	24.939	24.138	23.607

(g) 132Cs_100-1000-100ms_091.dat

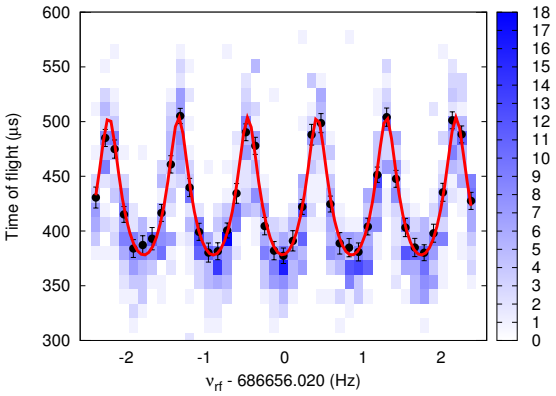

(h) 132Cs_100-1000-100ms_095.dat

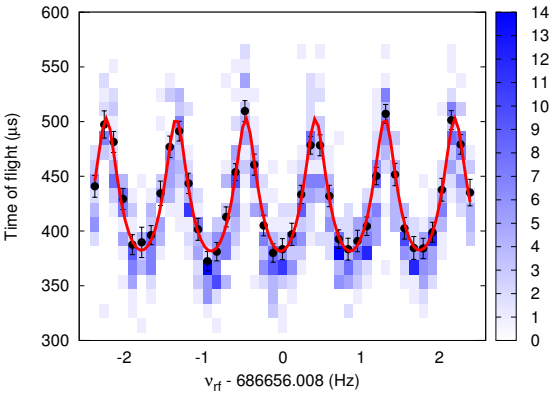

(i) 132Cs_100-1000-100ms_097.dat

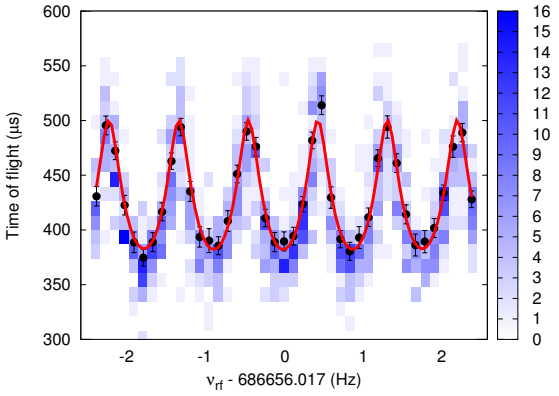

B.2.2 ToF-ICR for ^{146}Cs isotope

Table B.4: Results from the ^{146}Cs data analysis for the main floating parameters.

DataFile	146Cs_400ms_083	146Cs_40-320-40ms_085	146Cs_40-320-40ms_087
Nr.Ion	670	2349	952
$\nu_c(Hz)$	620624.4055(0.0864)	620624.4212(0.0125)	620624.4034(0.025)
ρ_-	0.511(0.019)	0.511(0.019)	0.418(0.035)
Conv	1.162(0.095)	0.926(0.043)	0.847(0.118)
χ^2/N_{DoF}	0.869	0.961	0.581
ToF effect	17.558	21.256	17.781

(j) 146Cs_400ms_083.dat

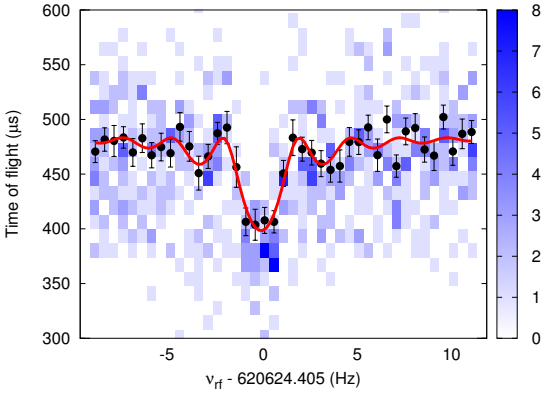

(k) 146Cs_40-320-40ms_085.dat

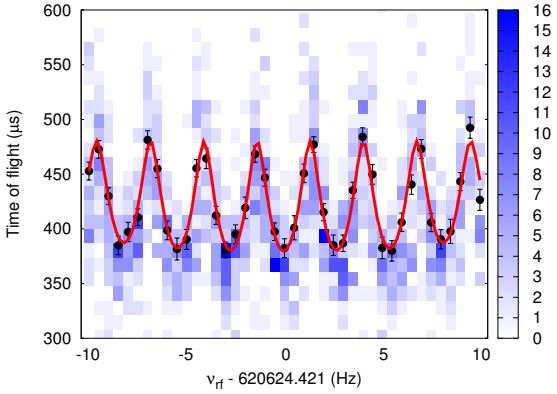

(l) 146Cs_40-320-40ms_087.dat

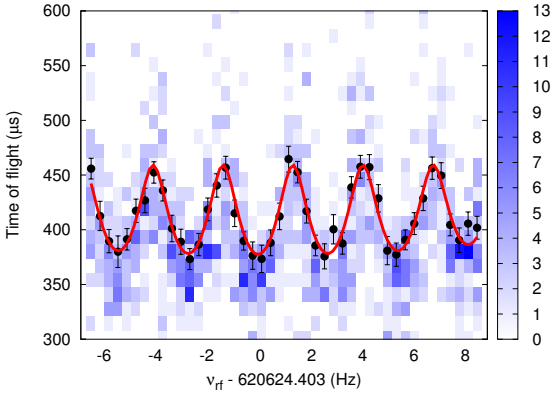

B.2.3 ToF-ICR for ^{147}Cs isotope

Table B.5: Results from the ^{147}Cs data analysis for the main floating parameters.

DataFile	147Cs_200ms_083	147Cs_20-160-20ms_085	147Cs_20-160-20ms_087
Nr.Ion	579	424	844
$\nu_c(Hz)$	616385.4948(0.1316)	616385.458(0.0649)	616385.5388(0.0407)
ρ_-	0.456(0.033)	0.411(0.055)	0.418(0.022)
Conv	0.968(0.130)	0.760(0.171)	0.985(0.071)
χ^2/N_{DoF}	1.526	0.756	1.032
ToF effect	19.428	16.703	18.213

(m) 147Cs_200ms_083.dat

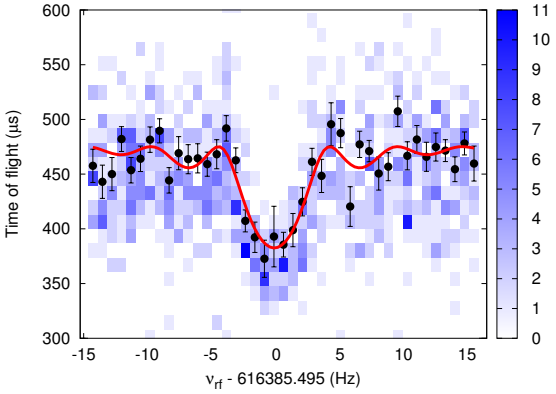

(n) 147Cs_20-160-20ms_085.dat

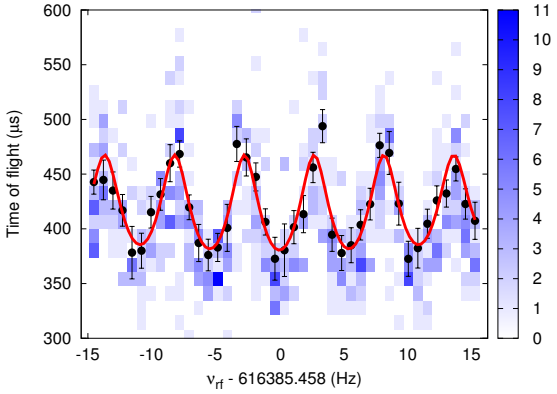

(o) 147Cs_20-160-20ms_087.dat

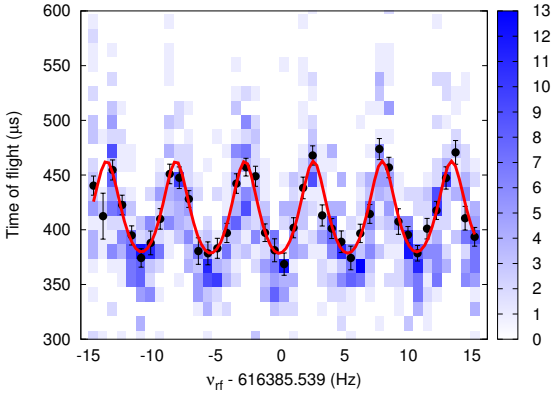

B.2.4 ToF-ICR for ^{148}Cs isotope

Table B.6: Results from the ^{148}Cs data analysis for the main floating parameters.

DataFile	148Cs_200ms_067	148Cs_20-160-20ms_069	148Cs_20-160-20ms_071
Nr.Ion	220	283	280
$\nu_c(Hz)$	612197.0007(0.3451)	612196.965(0.0776)	612196.8811(0.067)
$\rho-$	0.600(0.077)	0.400(0.038)	0.499(0.047)
Conv	1.207(0.089)	0.997(0.125)	1.004(0.121)
χ^2/N_{DoF}	0.792	0.929	0.82
ToF effect	23.571	17.374	21.531

(p) 148Cs_200ms_067.dat

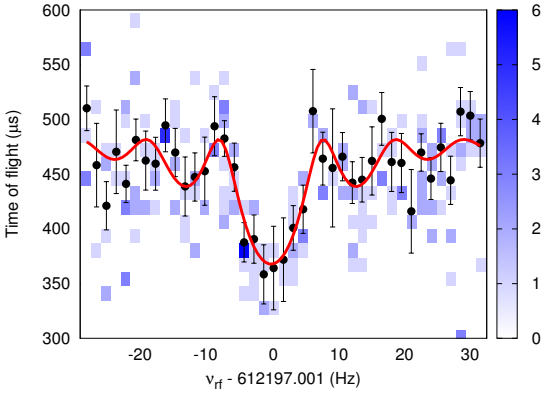

(q) 148Cs_20-160-20ms_069.dat

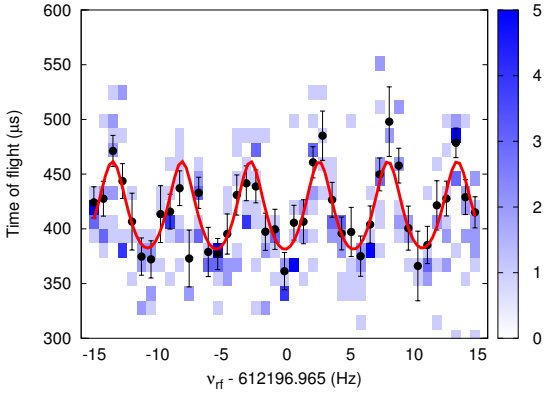

(r) 148Cs_20-160-20ms_071.dat

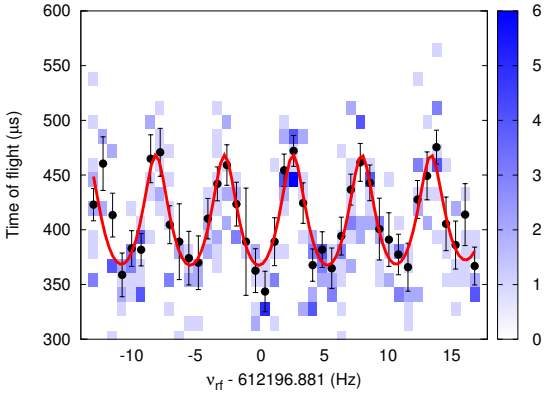

Bibliography

[AGT07] M. Arnould, S. Goriely, and K. Takahashi. "The r-process of stellar nucleosynthesis: Astrophysics and nuclear physics achievements and mysteries". In: *Phys. Rep.* 450.4-6 (2007), pp. 97–213. DOI: 10.1016/j.physrep.2007.06.002 (cit. on pp. 56, 61–67).

[AH29] R. d. E. Atkinson and F. G. Houtermans. "Zur Frage der Aufbaumöglichkeit der Elemente in Sternen". In: *Zeitschrift für Physik* 54.9 (Mar. 1929), pp. 656–665. DOI: 10.1007/BF01341595 (cit. on p. 4).

[Ald97] John Aldrich. "R.A. Fisher and the making of maximum likelihood 1912-1922". In: *Statist. Sci.* 12.3 (Sept. 1997), pp. 162–176. DOI: 10.1214/ss/1030037906 (cit. on p. 42).

[Arz+07] Arzner, K., Güdel, M., Briggs, K., et al. "Unbinned maximum-likelihood estimators for low-count data". In: *AA* 468.2 (Sept. 2007), pp. 501–514. DOI: 10.1051/0004-6361:20064927 (cit. on p. 42).

[Ast21] F. W. Aston. "Isotopes and Atomic Weights". In: *Nature* 105 (1921), p. 617 (cit. on p. 3).

[Ast22] F. W. Aston. "Isotopes". In: *E. Arnould, London* (1922) (cit. on p. 1).

[Ast23] F. W. Aston. "The Mass-spectra of Chemical Elements". In: *Phil. Mag.* 45 (1923), p. 934 (cit. on p. 1).

[AT13] A Arcones and F-K Thielemann. "Neutrino-driven wind simulations and nucleosynthesis of heavy elements". In: *J. Phys. G* 40.1 (2013), p. 013201 (cit. on p. 65).

[Aud+12a] G. Audi et al. "The atomic mass evaluation". In: *Chinese Phys. C* 36 (2012), p. 1287. DOI: 10.1088/1674-1137/36/12/001 (cit. on pp. 3, 42, 47, 54, 60).

[Aud+12b] G. Audi et al. "The Nubase2012 evaluation of nuclear properties". In: *Chinese Phys. C* 36 (2012), p. 1157. DOI: 10.1088/1674-1137/36/12/001 (cit. on pp. 50, 66).

[AW95] G. Audi and A.H. Wapstra. "The 1995 update to the atomic mass evaluation". In: *Nuc. Phys. A* 595.4 (1995), pp. 409 –480. DOI: 10.1016/0375-9474(95)00445-9 (cit. on p. 3).

[BB36] H. A. Bethe and R. F. Bacher. "Nuclear Physics A. Stationary States of Nuclei". In: *Rev. Mod. Phys.* 8 (2 1936), pp. 82–229. DOI: 10.1103/RevModPhys.8.82 (cit. on p. 2).

[BCS57] J. Bardeen, L. N. Cooper, and J. R. Schrieffer. "Theory of Superconductivity". In: *Phys. Rev.* 108 (5 Dec. 1957), pp. 1175–1204. DOI: 10.1103/PhysRev.108.1175 (cit. on p. 56).

[Bec+08] D. Beck et al. "Electric and magnetic field optimization procedure for Penning trap mass spectrometers". In: *Nucl. Instrum. Methods A* 598 (2008), p. 635. DOI: 10.1016/j.nima.2008.09.019 (cit. on p. 29).

[Bel+08] K. Belczynski, R. O'Shaughnessy, V. Kalogera, et al. "The Lowest-Mass Stellar Black Holes: Catastrophic Death of Neutron Stars in Gamma-Ray Bursts". In: *Astrophys. J. Lett.* 680.2 (2008), p. L129. DOI: 10.1086/589970 (cit. on p. 65).

[Ben+00] R. Benett et al. "Radioactive Nuclear Beam Facilities". In: *NuPECC Report* (2000) (cit. on p. 25).

[Bet39] H. A. Bethe. "Energy Production in Stars". In: *Phys. Rev.* 55 (1939), pp. 434 –456. DOI: 10.1103/PhysRev.55.434 (cit. on p. 4).

[BG86] L. S. Brown and G. Gabrielse. "Geonium theory: Physics of a single electron or ion in a Penning trap". In: *Rev. Mod. Phys.* 58 (1 Jan. 1986), pp. 233–311. DOI: 10.1103/RevModPhys.58.233 (cit. on pp. 7, 10–15).

[BHM12] C. Barbero, J. G. Hirsch, and A. E. Mariano. "Deformation and shell effects in nuclear mass formulas". In: *Nuc. Phys. A* 874 (2012), pp. 81 –97. DOI: 10.1016/j.nuclphysa.2011.11.005 (cit. on p. 3).

[BHR03] Michael Bender, Paul-Henri Heenen, and Paul-Gerhard Reinhard. "Self-consistent mean-field models for nuclear structure". In: *Rev. Mod. Phys.* 75 (1 Jan. 2003), pp. 121–180. DOI: 10.1103/RevModPhys.75.121 (cit. on p. 57).

[BL13] K. Blaum and Yu. A. Litvinov. "100 years of mass spectrometry". In: *Int. J Mass Spectrometry* 349 - 350 (2013), pp. 1 –2 (cit. on p. 7).

[Bla+03a] K. Blaum, G. Bollen, F. Herfurth, et al. "Recent developments at ISOLTRAP: towards a relative mass accuracy of exotic nuclei below 10^{-8}". In: *J. Phys B* 36.5 (2003), p. 921 (cit. on pp. 15–17).

[Bla+03b] K. Blaum, C. Geppert, H.-J. Kluge, et al. "A novel scheme for a highly selective laser ion source". In: *Nuclear Instruments and Methods in Physics Research Section B: Beam Interactions with Materials and Atoms* 204 (2003). 14th International Conference on Electromagnetic Isotope Separators and Techniques Related to their Applications, pp. 331 –335. DOI: 10.1016/S0168-583X(02)01942-0 (cit. on p. 28).

[Bla+04] K. Blaum, D. Beck, G. Bollen, et al. "Population inversion of nuclear states by a Penning trap mass spectrometer". In: *Europhys. Lett.)* 67.4 (2004), p. 586 (cit. on p. 38).

[Bla06] Klaus Blaum. "High-accuracy mass spectrometry with stored ions". In: *Phys. Rep.* 425.1 (2006), pp. 1 –78. DOI: 10.1016/j.physrep.2005.10.011 (cit. on pp. 1, 11).

[Blo15] M. Block. "Direct mass measurements of the heaviest elements with Penning traps". In: *Nuc. Phys. A* 944 (2015), pp. 471 –491. DOI: 10.1016/j.nuclphysa.2015.09.009 (cit. on p. 25).

[Blo53] F. Bloch. "Experiments on the g-factor of the electron". In: *Phys* 19.1–12 (1953), pp. 821 –831. DOI: 10.1016/S0031-8914(53)80091-1 (cit. on p. 18).

[BLS08] K. Blaum, Yu. A. Litvinov, and L. Schweikhard. "Masses of Short-Lived Nuclides: Precision Measurement Techniques and Applications". In: *Nucl. Phys. News* 18.3 (2008), pp. 29–34. DOI: 10.1080/10506890802336281 (cit. on pp. 1, 25).

[BM98] A. Bohr and B. R. Mottelson. *Nuclear Structure*. Vol. Volume I. 1998 (cit. on p. 1).

[BN36] N. E. Bradbury and R. A. Nielsen. "Absolute Values of the Electron Mobility in Hydrogen". In: *Phys. Rev.* 49 (5 Mar. 1936), pp. 388–393. DOI: 10.1103/PhysRev.49.388 (cit. on p. 32).

[BND13] Y. Blumenfeld, T. Nilsson, and P. Van Duppen. "Facilities and methods for radioactive ion beam production". In: *Phys. Scr.* T152 (2013), p. 014023 (cit. on p. 25).

[BOG58] N. N. BOGOLIUBOV. "A NEW METHOD IN THE THEORY OF SUPERCONDUCTIVITY. I*". In: *Sov. Phys. JETP* 34 (7 Jan. 1958), pp. 41 –46 (cit. on p. 56).

[Bol+90] G. Bollen, R. B. Moore, G. Savard, et al. "The accuracy of heavy-ion mass measurements using time of flight-ion cyclotron resonance in a Penning trap". In: *J Appl. Phys.* 68.9 (1990), pp. 4355–4374 (cit. on pp. 11, 13, 14).

[Bol+92a] G. Bollen et al. "Resolution of nuclear ground and isomeric states by a Penning trap mass spectrometer". In: *Phys. Rev. C* 46 (1992), R2140–R2143. DOI: 10.1103/PhysRevC.46.R2140 (cit. on pp. 38, 41).

[Bol+92b] G. Bollen, H.-J. Kluge, T. Otto, et al. "Ramsey technique applied in a Penning trap mass spectrometer". In: *Nucl. Instrum. Meth. B* 70.1 (1992), pp. 490–493. DOI: 10.1016/0168-583X(92)95971-S (cit. on p. 21).

[Bol94] G. Bollen. *Präzisionsbestimmung atomarer Massen*. Habilitationsschrift, Johannes Gutenberg - Universität, Mainz. 1994 (cit. on pp. 14, 15).

[Bol+96] G Bollen, S Becker, H.-J Kluge, et al. "ISOLTRAP: a tandem Penning trap system for accurate on-line mass determination of short-lived isotopes". In: *Nuclear Instruments and Methods in Physics Research Section A: Accelerators, Spectrometers, Detectors and Associated Equipment* 368.3 (1996), pp. 675 –697. DOI: 10.1016/0168-9002(95)00561-7 (cit. on p. 7).

[Bor+11] Ch. Borgmann, M. Breitenfeldt, G. Audi, et al. "Cadmium mass measurements between the neutron shell closures at $N = 50$ and 82". In: *AIP Conference Proceedings* 1377.1 (2011), pp. 332–334. DOI: 10.1063/1.3628403 (cit. on p. 47).

[Bos03] F. Bosch. "Schottky mass- and lifetime-spectrometry of unstable, stored ions". In: *J. Phys. B: At. Mol. Opt. Phys.* 36.3 (2003), p. 585 (cit. on pp. 4, 5).

[Bou+07] E. Bouquerel et al. "Purification of a Zn radioactive ion beam by alkali suppression in a quartz line target prototype". In: *Eur. Phys. J Special Topics* 150.1 (2007), pp. 277–280. DOI: 10.1140/epjst/e2007-00323-4 (cit. on pp. 28, 47).

[Bou+08] E. Bouquerel, R. Catherall, M. Eller, et al. "Beam purification by selective trapping in the transfer line of an {ISOL} target unit". In: *Nucl. Instrum. Methods B* 266.19-20 (2008), pp. 4298 –4302. DOI: 10.1016/j.nimb.2008.05.060 (cit. on pp. 28, 47).

[BR97] R. Brun and F. Rademakers. "{ROOT} An object oriented data analysis framework". In: *Nucl. Inst. Methods Phys. Res. A* 389.1 - 2 (1997), pp. 81 –86. DOI: 10.1016/S0168-9002(97)00048-X (cit. on p. 44).

[Bra+99] Michael P. Bradley, James V. Porto, Simon Rainville, et al. "Penning Trap Measurements of the Masses of ^{133}Cs, $^{87,85}Rb$, and ^{23}Na with Uncertainties ≤ 0.2 ppb". In: *Phys. Rev. Lett.* 83 (22 Nov. 1999), pp. 4510–4513. DOI: 10.1103/PhysRevLett.83.4510 (cit. on p. 47).

[Bre+10] M. Breitenfeldt, Ch. Borgmann, G. Audi, et al. "Approaching the $N = 82$ shell closure with mass measurements of Ag and Cd isotopes". In: *Phys. Rev. C* 81 (3 Mar. 2010), p. 034313. DOI: 10.1103/PhysRevC.81.034313 (cit. on p. 47).

[Bro13] B. Alex Brown. "Pairing and shell gaps in nuclei". In: *J. Phys. Conf. Ser.* 445.1 (2013), p. 012010 (cit. on p. 60).

[Bur+57] E. M. Burbidge, G. R. Burbidge, W. A. Fowler, et al. "Synthesis of the Elements in Stars". In: *Rev. Mod. Phys.* 29 (4 1957), pp. 547–650. DOI: 10.1103/RevModPhys.29.547 (cit. on pp. 4, 61).

[Cam57] A. G. W. Cameron. "Stellar Evolution". In: *Nuclear astrophysics and nucleogenesis, Chalk River (Canada) Report CRL-41* (1957) (cit. on p. 4).

[Cha67] S. Chandrasekhar. *Introduction to the study of Stellar Structure*. Dover Publications, INC, 1967 (cit. on p. 65).

[Cla+61] D.D. Clayton, W.A. Fowler, T.E. Hull, et al. "Neutron capture chains in heavy element synthesis". In: *Ann. Phys.* 12.3 (1961), pp. 331–408. DOI: 10.1016/0003-4916(61)90067-7 (cit. on p. 61).

[CM74] Melvin B. Comisarow and Alan G. Marshall. "Fourier transform ion cyclotron resonance spectroscopy". In: *Chem. Phys. Lett.* 25.2 (1974), pp. 282 –283. DOI: 10.1016/0009-2614(74)89137-2 (cit. on p. 18).

[Deh90] H. Dehmelt. "Experiments with an isolated subatomic particle at rest". In: *Rev. Mod. Phys.* 62 (1990), pp. 525–530 (cit. on p. 7).

[Dil+03] I. Dillmann et al. "$N = 82$ Shell Quenching of the Classical r-Process "Waiting-Point" Nucleus ^{130}Cd". In: *Phys. Rev. Lett.* 91 (16 2003), p. 162503. DOI: 10.1103/PhysRevLett.91.162503 (cit. on pp. 50, 55, 60).

[DZ95] J. Duflo and A.P. Zuker. "Microscopic mass formulas". In: *Phys. Rev. C* 52 (1 July 1995), R23–R27. DOI: 10.1103/PhysRevC.52.R23 (cit. on p. 3).

[Edd20] A. S. Eddington. "The Internal Constitution of the Stars". In: *Nature* 106 (1920), p. 14 (cit. on p. 4).

[Eit+09] G. Eitel, M. Block, A. Czasch, et al. "Position-sensitive ion detection in precision Penning trap mass spectrometry". In: *NIM A* 606.3 (2009), pp. 475 –483. DOI: 10.1016/j.nima.2009.04.046 (cit. on p. 18).

[Eli+13] S. Eliseev, K. Blaum, M. Block, et al. "A phase-imaging technique for cyclotron-frequency measurements". In: *Applied Physics B* 114.1 (2013), pp. 107–128. DOI: 10.1007/s00340-013-5621-0 (cit. on p. 69).

[Erl+12] Jochen Erler et al. "The limits of the nuclear landscape". In: *Nature* 486 (2012), pp. 509–512. DOI: 10.1038/nature11188 (cit. on p. 1).

[FGM08] B. Franzke, H. Geissel, and G. Münzenberg. "Mass and lifetime measurements of exotic nuclei in storage rings". In: *Mass Spectr. Rev.* 27.5 (2008), pp. 428–469. DOI: 10.1002/mas.20173 (cit. on pp. 7, 25).

[Fie97] Stephen E. Fienberg. "Introduction to R.A. Fisher on inverse probability and likelihood". In: *Statist. Sci.* 12.3 (Sept. 1997), p. 161. DOI: 10.1214/ss/1030037905 (cit. on p. 42).

[Fin+13] D.A. Fink et al. "First application of the Laser Ion Source and Trap (LIST) for on-line experiments at {ISOLDE}". In: *Nucl. Instrum. Methods B* 317, Part B (2013), pp. 417 –421. DOI: 10.1016/j.nimb.2013.06.039 (cit. on p. 28).

[GA96] S. Goriely and M. Arnould. "Waiting point approximation and canonical multi-event r-process revisited". In: *Astron. Astrophys.* 312 (Aug. 1996), pp. 327–337 (cit. on p. 64).

[Gam28] G. Gamow. "Zur Quantentheorie des Atomkernes". German. In: *Z. Phys.* 51.3-4 (1928), pp. 204–212. DOI: 10.1007/BF01343196 (cit. on p. 4).

[Gam30] G. Gamow. "Mass Defect Curve and Nuclear Constitution". In: *Proc. R. Soc. London, Ser. A* 126.803 (1930), pp. 632–644. DOI: 10.1098/rspa.1930.0032 (cit. on p. 2).

[GC29] R. W. Gurney and E. U. Condon. *Quantum Mechanics and Radioactive Disintegration*. Feb. 1929. DOI: 10.1103/PhysRev.33.127 (cit. on p. 4).

[GCP09] S. Goriely, N. Chamel, and J. M. Pearson. "Skyrme-Hartree-Fock-Bogoliubov Nuclear Mass Formulas: Crossing the 0.6 MeV Accuracy Threshold with Microscopically Deduced Pairing". In: *Phys. Rev. Lett.* 102 (15 Apr. 2009), p. 152503. DOI: 10.1103/PhysRevLett.102.152503 (cit. on p. 57).

[GCP10] S. Goriely, N. Chamel, and J. M. Pearson. "Further explorations of Skyrme-Hartree-Fock-Bogoliubov mass formulas. XII. Stiffness and stability of neutron-star matter". In: *Phys. Rev. C* 82 (3 Sept. 2010), p. 035804. DOI: 10.1103/PhysRevC.82.035804 (cit. on p. 57).

[GCP13a] S. Goriely, N. Chamel, and J. M. Pearson. "Further explorations of Skyrme-Hartree-Fock-Bogoliubov mass formulas. XIII. The 2012 atomic mass evaluation and the symmetry coefficient". In: *Phys. Rev. C* 88 (2 Aug. 2013), p. 024308. DOI: 10.1103/PhysRevC.88.024308 (cit. on p. 57).

[GCP13b] S. Goriely, N. Chamel, and J. M. Pearson. "Further explorations of Skyrme-Hartree-Fock-Bogoliubov mass formulas. XIII. The 2012 atomic mass evaluation and the symmetry coefficient". In: *Phys. Rev. C* 88 (2 Aug. 2013), p. 024308. DOI: 10.1103/PhysRevC.88.024308 (cit. on pp. 59, 60).

[GCP16] S. Goriely, N. Chamel, and J. M. Pearson. "Further explorations of Skyrme-Hartree-Fock-Bogoliubov mass formulas. XVI. Inclusion of self-energy effects in pairing". In: *Phys. Rev. C* 93 (3 Mar. 2016), p. 034337. DOI: 10.1103/PhysRevC.93.034337 (cit. on p. 57).

[Geo+07] S. George, K. Blaum, F. Herfurth, et al. "The Ramsey method in high-precision mass spectrometry with Penning traps: Experimental results". In: *Int. J. Mass Spectrom.* 264 (2007), pp. 110 –121. DOI: 10.1016/j.ijms.2007.04.003 (cit. on p. 21).

[Geo+08] S. George, G. Audi, B. Blank, et al. "Time-separated oscillatory fields for high-precision mass measurements on short-lived Al and Ca nuclides". In: *Europhys. Lett.* 82.5 (2008), p. 50005. DOI: 10.1209/0295-5075/82/50005 (cit. on p. 21).

[GHK08] S. Goriely, S. Hilaire, and A. J. Koning. "Improved predictions of nuclear reaction rates with the TALYS reaction code for astrophysical applications". In: *Astron. Astrophys.* 487.2 (2008), p. 767 (cit. on p. 66).

[Gil+03] T.J. Giles, R. Catherall, V. Fedosseev, et al. "The high resolution spectrometer at {ISOLDE}". In: *Nuclear Instruments and Methods in Physics Research Section B: Beam Interactions with Materials and Atoms* 204 (2003). 14th International Conference on Electromagnetic Isotope Separators and Techniques Related to their Applications, pp. 497 –501. DOI: 10.1016/S0168-583X(02)02119-5 (cit. on p. 28).

[GKT80] G. Gräff, H. Kalinowsky, and J. Traut. "A direct determination of the proton electron mass ratio". In: *Z Phys* 297.1 (1980), pp. 35–39. DOI: 10.1007/BF01414243 (cit. on p. 18).

[Gor+09] S. Goriely, S. Hilaire, M. Girod, et al. "First Gogny-Hartree-Fock-Bogoliubov Nuclear Mass Model". In: *Phys. Rev. Lett.* 102 (24 June 2009), p. 242501. DOI: 10.1103/PhysRevLett.102.242501 (cit. on p. 3).

[Gor97] S. Goriely. "A new approach to the canonical s-process model". In: *Astron. Astrophys.* 327 (2 1997), pp. 845–853 (cit. on p. 62).

[Gor99] S. Goriely. "Uncertainties in the solar system r-abundance distribution". In: *Astron. Astrophys.* 342 (1999), pp. 881–891 (cit. on p. 61).

[Har17] W. D. Harkins. In: *J. Am. Chem. Soc.* 39 (1917), p. 856. DOI: 10.1021/ja02250a002 (cit. on p. 4).

[Her+01] F. Herfurth et al. "A linear radiofrequency ion trap for accumulation, bunching, and emittance improvement of radioactive ion beams". In: *Nucl. Instrum. Methods A* 469.2 (2001), pp. 254 –275. DOI: 10.1016/S0168-9002(01)00168-1 (cit. on p. 30).

[Her+03] F Herfurth et al. "Mass measurements and nuclear physics—recent results from ISOLTRAP". In: *J Phys. B* 36.5 (2003), p. 931 (cit. on p. 30).

[Her+15] F. Herfurth, Z. Andelkovic, W. Barth, et al. "The HITRAP facility for slow highly charged ions". In: *Phys. Scr.* T166 (2015), p. 014065 (cit. on p. 25).

[HJJ95] P. G. Hansen, A. S. Jensen, and B. Jonson. "Nuclear Halos". In: *Ann. Rev. Nuc. Part. Sci.* 45.1 (1995), pp. 591–634. DOI: 10.1146/annurev.ns.45.120195.003111 (cit. on p. 57).

[HKT76] W. Hillebrandt, T. Kodama, and K. Takahashi. "R-process nucleosynthesis - A dynamical model". In: *Astron. Astrophys.* 52 (Oct. 1976), pp. 63–68 (cit. on pp. 64, 65).

[HT09] J. C. Hardy and I. S. Towner. "Superallowed $0^+ \rightarrow 0^+$ nuclear β decays: A new survey with precision tests of the conserved vector current hypothesis and the standard model". In: *Phys. Rev. C* 79 (5 May 2009), p. 055502. DOI: 10.1103/PhysRevC.79.055502 (cit. on p. 1).

[HT15] J. C. Hardy and I. S. Towner. "Superallowed $0^+ \rightarrow 0^+$ nuclear β decays: 2014 critical survey, with precise results for V_{ud} and CKM unitarity". In: *Phys. Rev. C* 91 (2 Feb. 2015), p. 025501. DOI: 10.1103/PhysRevC.91.025501 (cit. on p. 1).

[Ili07] C. Iliadis. *Nuclear Physics of stars*. WILEY-VCH Verlag GmbH & Co. KGaA, 2007 (cit. on p. 4).

[Jus+15] O. Just et al. "Comprehensive nucleosynthesis analysis for ejecta of compact binary mergers". In: *Month. Not. Roy. Astron. Soc.* 448 (2015), p. 541 (cit. on pp. 66, 68).

[KBW89] F. Käppeler, H. Beer, and K. Wisshak. "s-process nucleosynthesis-nuclear physics and the classical model". In: *Reports on Progress in Physics* 52.8 (1989), p. 945 (cit. on p. 61).

[Kel+03] A. Kellerbauer, K. Blaum, G. Bollen, et al. "From direct to absolute mass measurements: A study of the accuracy of ISOLTRAP". In: *Eur. Phys. J. D* 22.1 (2003), pp. 53–64. DOI: 10.1140/epjd/e2002-00222-0 (cit. on pp. 14, 40, 41).

[KHD08] A. J. Koning, S. Hilaire, and M. C. Duijvestijn. "TALYS-1.0". In: *Nucl. Data Science and Technology* (2008). (EDP Sciences; eds O. Bersillon et al.), pp. 211–214. DOI: 10.1051/ndata:07767 (cit. on p. 66).

[Knö+16] R. Knöbel et al. "First direct mass measurements of stored neutron-rich ^{129,130,131}Cd isotopes with FRS-ESR". In: *Phys. Lett. B* 754 (2016), pp. 288 –293. DOI: 10.1016/j.physletb.2016.01.039 (cit. on p. 50).

[Kön+95] M. König, G. Bollen, H.-J. Kluge, et al. "Quadrupole excitation of stored ion motion at the true cyclotron frequency". In: *Int. J. Mass Spectrom* 142.1–2 (1995), pp. 95 –116. DOI: 10.1016/0168-1176(95)04146-C (cit. on pp. 17, 20, 40).

[Kös01] U. Köster. "How to produce Intense and pure ISOL beams". In: *Prog. Part. Nucl. Phys* 46 (2001), p. 411 (cit. on p. 28).

[Kös02] U. Köster. "Intense radioactive-ion beams produced with the ISOL method". In: *Eur. Phys. J. A* 15.1 (2002), pp. 255–263. DOI: 10.1140/epja/i2001-10264-2 (cit. on p. 26).

[Kou+00] H. Koura, M. Uno, T. Tachibana, et al. "Nuclear mass formula with shell energies calculated by a new method". In: *Nuc. Phys. A* 674.1-2 (2000), pp. 47 –76. DOI: 10.1016/S0375-9474(00)00155-X (cit. on p. 3).

[Kow+12] M. Kowalska et al. "Trap-assisted decay spectroscopy with ISOLTRAP". In: *Nucl. Instrum. Methods A* 689 (2012), p. 102. DOI: doi:10.1016/j.nima.2012.04.059 (cit. on p. 38).

[Kra+05] K. -L. Kratz, B. Pfeiffer, O. Arndt, et al. "r-process isotopes in the ^{132}Sn region". In: *Eur. Phys. J. A* 25.1 (2005), pp. 633–638. DOI: 10.1140/epjad/i2005-06-157-2 (cit. on p. 48).

[Kre07] M. Kretzschmar. "The Ramsey method in high-precision mass spectrometry with Penning traps: Theoretical foundations". In: *Int. J. Mass Spectr.* 264.2-3 (2007), pp. 122 –145. DOI: 10.1016/j.ijms.2007.04.002 (cit. on p. 21).

[Kre08] M. Kretzschmar. "Calculating damping effects for the ion motion in a Penning trap". In: *Eur. Phys. J. D* 48.3 (2008), pp. 313–319. DOI: 10.1140/epjd/e2008-00125-0 (cit. on p. 21).

[Kre+13] S. Kreim et al. "Recent exploits of the {ISOLTRAP} mass spectrometer". In: *Nucl. Instrum. Methods B* 317 (2013), pp. 492 –500. DOI: 10.1016/j.nimb.2013.07.072 (cit. on pp. 28, 29, 33, 34, 48).

[Kug00] Erich Kugler. "The ISOLDE facility". In: *Hyp. Int.* 129.1-4 (2000), pp. 23–42. DOI: 10.1023/A:1012603025802 (cit. on p. 26).

[Lan99] K. R. Lang. "Nuclide Abundance Equations". In: *Astrophysical formulae*. Springer-Verlag, Berlin Heidelberg, 1999. Chap. 4.4.5 (cit. on p. 62).

[Liu+11] M. Liu, N. Wang, Y. Deng, et al. "Further improvements on a global nuclear mass model". In: *Phys. Rev. C* 84 (1 July 2011), p. 014333. DOI: 10.1103/PhysRevC.84.014333 (cit. on p. 3).

[LM03] K. Langanke and G. Martínez-Pinedo. "Nuclear weak-interaction processes in stars". In: *Rev. Mod. Phys.* 75 (3 June 2003), pp. 819–862. DOI: 10.1103/RevModPhys.75.819 (cit. on p. 64).

[Lor+15a] G. Lorusso et al. "β-Decay Half-Lives of 110 Neutron-Rich Nuclei across the $N = 82$ Shell Gap: Implications for the Mechanism and Universality of the Astrophysical r Process". In: *Phys. Rev. Lett.* 114 (19 May 2015), p. 192501. DOI: 10.1103/PhysRevLett.114.192501 (cit. on pp. 55, 66).

[Lor+15b] G. Lorusso, S. Nishimura, Z. Y. Xu, et al. "β-Decay Half-Lives of 110 Neutron-Rich Nuclei across the $N = 82$ Shell Gap: Implications for the Mechanism and Universality of the Astrophysical r Process". In: *Phys. Rev. Lett.* 114 (19 May 2015), p. 192501. DOI: 10.1103/PhysRevLett.114.192501 (cit. on p. 49).

[LPG09] K. Lodders, H. Palme, and H.-P. Gail. "Abundances of the elements in the Solar System". In: *Solar System*. Ed. by J.E. Trümper. 2009. Chap. 4B. DOI: 10.1007/978-3-540-88055-4_34 (cit. on pp. 4, 61).

[LPT03] D. Lunney, J. M. Pearson, and C. Thibault. "Recent trends in the determination of nuclear masses". In: *Rev. Mod. Phys.* 75 (3 Aug. 2003), pp. 1021–1082. DOI: 10.1103/RevModPhys.75.1021 (cit. on pp. 56, 57).

[LS74] J. M. Lattimer and D. N. Schramm. "Black-hole-neutron-star collisions". In: *Astrophys. J.* 192 (1974), p. L145. DOI: 10.1086/181612 (cit. on p. 65).

[LS76] J. M. Lattimer and D. N. Schramm. "The tidal disruption of neutron stars by black holes in close binaries". In: *Astrophys. J.* 210 (1976), p. 549. DOI: 10.1086/154860 (cit. on p. 65).

[LW01] K. Langanke and M. Wiescher. "Nuclear reactions and stellar processes". In: *Rep. Prog. Phys.* 64.12 (2001), p. 1657 (cit. on pp. 5, 61).

[MA06] C. A. Meakin and D. Arnett. "Active Carbon and Oxygen Shell Burning Hydrodynamics". In: *The Astrophys. J. Lett.* 637.1 (2006), p. L53 (cit. on p. 64).

[Mam+98] A. Mamdouh, J.M. Pearson, M. Rayet, et al. "Large-scale fission-barrier calculations with the {ETFSI} method". In: *Nucl. Phys. A* 644.4 (1998), pp. 389 –414. DOI: 10.1016/S0375-9474(98)00576-4 (cit. on p. 56).

[Mar+13] B.A. Marsh, B. Andel, A.N. Andreyev, et al. "New developments of the in-source spectroscopy method at RILIS/ISOLDE". In: *Nucl. Instrum. Methods B* 317, Part B (2013), pp. 550 –556. DOI: 10.1016/j.nimb.2013.07.070 (cit. on p. 27).

[May49] Maria Goeppert Mayer. "On Closed Shells in Nuclei. II". In: *Phys. Rev.* 75 (12 1949), pp. 1969–1970. DOI: 10.1103/PhysRev.75.1969 (cit. on p. 2).

[MFW96] Gail C. Mclaughlin, George M. Fuller, and James R. Wilson. "The Influence of Nuclear Composition on the Electron Fraction in the Post-Core Bounce Supernova Environment". In: *Astrophys. J.* 472.2 (1996), p. 440 (cit. on p. 65).

[MH02] Alan G. Marshall and Christopher L. Hendrickson. "Fourier transform ion cyclotron resonance detection: principles and experimental configurations". In: *Int. J. Mass Spectrom.* 215.1-3 (2002), pp. 59 –75. DOI: 10.1016/S1387-3806(01)00588-7 (cit. on p. 18).

[MNK97] P. MÖLLER, J.R. NIX, and K.-L. KRATZ. "NUCLEAR PROPERTIES FOR ASTROPHYSICAL AND RADIOACTIVE-ION-BEAM APPLICATIONS". In: *At. Data Nucl. Data Tables* 66.2 (1997), pp. 131 –343. DOI: 10.1006/adnd.1997.0746 (cit. on p. 56).

[Möl+12] Peter Möller, William D. Myers, Hiroyuki Sagawa, et al. "New Finite-Range Droplet Mass Model and Equation-of-State Parameters". In: *Phys. Rev. Lett.* 108 (5 Jan. 2012), p. 052501. DOI: 10.1103/PhysRevLett.108.052501 (cit. on pp. 3, 56, 59, 60).

[Muk+08] M. Mukherjee et al. "ISOLTRAP: An on-line Penning trap for mass spectrometry on short-lived nuclides". In: *Eur. Phys. J. A* 35.1 (2008), pp. 1–29. DOI: 10.1140/epja/i2007-10528-9 (cit. on p. 28).

[Mül+12] C. Müller et al. "A Unique Matched Quadruplet of Terbium Radioisotopes for PET and SPECT and for α- and β^--Radionuclide Therapy: An In Vivo Proof-of-Concept Study with a New Receptor-Targeted Folate Derivative". In: *J. Nucl. Med.* 53 (2012), pp. 1951–1959. DOI: 10.2967/jnumed.112.107540 (cit. on p. 33).

[Myu03] In Jae Myung. "Tutorial on Maximum Likelihood Estimation". In: *J. Math. Psychol.* 47.1 (Feb. 2003), pp. 90–100. DOI: 10.1016/S0022-2496(02)00028-7 (cit. on p. 42).

[NG10] K Nakamura and Particle Data Group. "Review of Particle Physics". In: *J. Phys. G: Nucl. Part. Phys.* 37.7A (2010), p. 075021 (cit. on p. 41).

[OJM07] R. Oechlin, H.-T. Janka, and A. Marek. "Relativistic neutron star merger simulations with non-zero temperature equations of state". In: *Astron. Astrophys.* 467.2 (2007), pp. 395–409. DOI: 10.1051/0004-6361:20066682 (cit. on p. 65).

[PB93] H. Palme and H. Beer. "Nuclear abundances and their decomposition in nucleosynthetic components". In: *Astronomy and Astrophysics · Instruments, Methods, Solar System*. Ed. by H. H. Voigt. 1993. Chap. 3A. DOI: 10.1007/10057790_60 (cit. on p. 62).

[Pen36] F. M. Penning. "Die Glimmentladung bei niedrigem Druck zwischen koaxialen Zylindern in einem axialen Magnetfeld". In: *Physica* 3 (1936), pp. 873–894 (cit. on p. 7).

[PGC13] J.M. Pearson, S. Goriely, and N. Chamel. "Microscopic mass models for astrophysics". In: *Int. J. Mass Spectr.* 349–350 (2013). 100 years of Mass Spectrometry, pp. 57 –62. DOI: 10.1016/j.ijms.2013.04.003 (cit. on p. 57).

[PNG96] J.M. Pearson, R.C. Nayak, and S. Goriely. "Nuclear mass formula with Bogolyubov-enhanced shell-quenching: application to r-process". In: *Phys. Lett. B* 387.3 (1996), pp. 455 –459. DOI: 10.1016/0370-2693(96)01071-4 (cit. on p. 56).

[Rai+97] H. Raimbault-Hartmann et al. "A cylindrical Penning trap for capture, mass selective cooling, and bunching of radioactive ion beams". In: *Nucl. Instrum. Methods B* 126 (1997), pp. 378 –382. DOI: 10.1016/S0168-583X(96)01067-1 (cit. on p. 34).

[RAM15] Tomás R. Rodríguez, Alexander Arzhanov, and Gabriel Martínez-Pinedo. "Toward global beyond-mean-field calculations of nuclear masses and low-energy spectra". In: *Phys. Rev. C* 91 (4 Apr. 2015), p. 044315. DOI: 10.1103/PhysRevC.91.044315 (cit. on p. 3).

[Ram90] N. F. Ramsey. "Experiments with separated oscillatory fields and hydrogen masers". In: *Rev. Mod. Phys.* 62 (3 July 1990), pp. 541–552. DOI: 10.1103/RevModPhys.62.541 (cit. on p. 20).

[Rav79] H. L. Ravn. "Experiments with intense secondary beams of radioactive ions". In: *Phys. Rep.* 54.3 (1979), pp. 201 –259. DOI: 10.1016/0370-1573(79)90045-0 (cit. on p. 28).

[RD02] S. Rosswog and M. B. Davies. "High-resolution calculations of merging neutron stars - I. Model description and hydrodynamic evolution". In: *Mon. Not. Roy. Astron. Soc.* 334.3 (2002), pp. 481–497. DOI: 10.1046/j.1365-8711.2002.05409.x (cit. on p. 65).

[RFD15] A. Radionova, I. Filippov, and P. J Derrick. "In pursuit of resolution in time-of-flight mass spectrometry: A historical perspective". In: *Mass Spectr. Rev.* MAS21470 (2015). DOI: 10.1002/mas.21470 (cit. on p. 22).

[Rin+06] R. Ringle, P. Schury, T. Sun, et al. "Precision mass measurements with {LEBIT} at {MSU}". In: *I. J. Mass Spectr.* 251.2-3 (2006). ULTRA-ACCURATE {MASS} {SPECTROMETRY} {AND} {RELATED} {TOPICS} Dedicated to H.-J. Kluge on the occasion of his 65th birthday anniversary Jürgen Kluge Special Issue, pp. 300 –306. DOI: 10.1016/j.ijms.2006.02.011 (cit. on p. 25).

[RL03] S. Rosswog and M. Liebendörfer. "High-resolution calculations of merging neutron stars - II. Neutrino emission". In: *Mon. Not. Roy. Astron. Soc.* 342.3 (2003), pp. 673–689. DOI: 10.1046/j.1365-8711.2003.06579.x (cit. on p. 65).

[Ros+12] M. Rosenbusch, Ch. Böhm, Ch. Borgmann, et al. "A study of octupolar excitation for mass-selective centering in Penning traps". In: *Int. J. Mass Spectr.* 314 (2012), pp. 6 –12. DOI: 10.1016/j.ijms.2012.01.002 (cit. on p. 35).

[Ros+15] M. Rosenbusch, P. Ascher, D. Atanasov, et al. "Probing the $N = 32$ Shell Closure below the Magic Proton Number $Z = 20$: Mass Measurements of the Exotic Isotopes ^{52,53}K". In: *Phys. Rev. Lett.* 114 (20 May 2015), p. 202501. DOI: 10.1103/PhysRevLett.114.202501 (cit. on p. 60).

[S+13] J. Stanja, Ch. Borgmann, et al. "Mass spectrometry and decay spectroscopy of isomers across the $Z = 82$ shell closure". In: *Phys. Rev. C* 88 (2013), p. 054304. DOI: 10.1103/PhysRevC.88.054304 (cit. on p. 38).

[Sat74] K. Sato. "Formation of Elements in Neutron Rich Ejected Matter of Supernovae. II: Dynamical r-Process Stage". In: *Prog. Theor. Phys.* 51.3 (1974), pp. 726–744. DOI: 10.1143/PTP.51.726 (cit. on p. 65).

[Sav+91] G. Savard et al. "A new cooling technique for heavy ions in a Penning trap". In: *Phys. Lett. A* 158.5 (1991), pp. 247 –252. DOI: 10.1016/0375-9601(91)91008-2 (cit. on p. 35).

[SFC65] P. A. Seeger, W. A. Fowler, and D. D. Clayton. "Nucleosynthesis of Heavy Elements by Neutron Capture". In: *Astrophys. J.* 11 (1965). Suppl., p. 121. DOI: 10.1086/190111 (cit. on p. 64).

[SIM] SIMION. *The field and particle trajectory simulator*. http://www.simion.com (cit. on pp. 72, 74).

[Sin] S. K. Singh. *Motion of a charged particle in magnetic field*. DOI: http://cnx.org/content/m31345/latest/ (cit. on p. 74).

[Sky56] T. H. R. Skyrme. "CVII. The nuclear surface". In: *Phil. Mag.* 1.11 (1956), pp. 1043–1054. DOI: 10.1080/14786435608238186 (cit. on p. 57).

[Sky58] T.H.R. Skyrme. "The effective nuclear potential". In: *Nucl. Phys.* 9.4 (1958), pp. 615 –634. DOI: 10.1016/0029-5582(58)90345-6 (cit. on p. 57).

[SR16] S. Swartz and R. Ringle. *EVA software and documentation*. https://groups.nscl.msu.edu/lebit/downloads/index.html. 2016 (cit. on p. 40).

[Sto13] T. Stora. "Recent developments of target and ion sources to produce {ISOL} beams". In: *Nucl. Instrum. Methods B* 317 (2013), pp. 402 –410. DOI: 10.1016/j.nimb.2013.07.024 (cit. on p. 33).

[Str67] V.M. Strutinsky. "Shell effects in nuclear masses and deformation energies". In: *Nucl. Phys. A* 95.2 (1967), pp. 420 –442. DOI: 10.1016/0375-9474(67)90510-6 (cit. on p. 56).

[Tap+15] J. Taprogge, A. Jungclaus, H. Grawe, et al. "β decay of ^{129}Cd and excited states in ^{129}In". In: *Phys. Rev. C* 91 (5 May 2015), p. 054324. DOI: 10.1103/PhysRevC.91.054324 (cit. on p. 49).

[TJ97] K. Takahashi and H. Janka. "Origin of Matter and Evolution of Galaxies". In: *Singapore: World Scientific* 213 (1997) (cit. on pp. 66, 67).

[Val61] J. G. Valatin. "Generalized Hartree-Fock Method". In: *Phys. Rev.* 122 (4 May 1961), pp. 1012–1020. DOI: 10.1103/PhysRev.122.1012 (cit. on p. 56).

[Van+13] J. Van Schelt et al. "First Results from the CARIBU Facility: Mass Measurements on the r-Process Path". In: *Phys. Rev. Lett.* 111 (2013), p. 061102. DOI: 10.1103/PhysRevLett.111.061102 (cit. on p. 52).

[Van+99] R. S. Van Dyck, D. L. Farnham, S. L. Zafonte, et al. "Ultrastable superconducting magnet system for a penning trap mass spectrometer". In: *Review of Scientific Instruments* 70.3 (1999), pp. 1665–1671. DOI: 10.1063/1.1149649 (cit. on p. 12).

[VB72] D. Vautherin and D. M. Brink. "Hartree-Fock Calculations with Skyrme's Interaction. I. Spherical Nuclei". In: *Phys. Rev. C* 5 (3 Mar. 1972), pp. 626–647. DOI: 10.1103/PhysRevC.5.626 (cit. on p. 57).

[VK05] W. Verkerke and D. Kirkby. *The ROOFIT toolkit for data modeling*. http://roofit.sourceforge.net/docs/roofit_phystat05.pdf. 2005 (cit. on p. 44).

[Wal+97] G. Wallerstein, I. Iben, P. Parker, et al. "Synthesis of the elements in stars: forty years of progress". In: *Rev. Mod. Phys.* 69 (4 Oct. 1997), pp. 995–1084. DOI: 10.1103/RevModPhys.69.995 (cit. on pp. 61, 64).

[WAT03] A.H. Wapstra, G. Audi, and C. Thibault. "The Ame2003 atomic mass evaluation: (I). Evaluation of input data, adjustment procedures". In: *Nuc. Phys. A* 729.1 (2003). The 2003 {NUBASE} and Atomic Mass Evaluations, pp. 129 –336. DOI: 10.1016/j.nuclphysa.2003.11.002 (cit. on pp. 3, 56).

[Web+05] C. Weber et al. "Weighing excited nuclear states with a Penning trap mass spectrometer". In: *Phys. Lett. A* 347 (2005), pp. 81–87 (cit. on p. 37).

[Web+08] C. Weber et al. "Atomic mass measurements of short-lived nuclides around the doubly-magic ^{208}Pb". In: *Nuc. Phys. A* 803 (2008), pp. 1–29 (cit. on p. 53).

[Wei35] C. F. v. Weizsäcker. "Zur Theorie der Kernmassen". In: *Z. Phys.* 96.7 (1935), pp. 431 –458. DOI: 10.1007/BF01337700 (cit. on pp. 2, 55).

[Wei38] C. F. v. Weizsäcker. "Über Elementumwandlungen in Innern der Sterne II". In: *Physik. Z.* 39 (1938), p. 633 (cit. on p. 4).

[WHW02] S. E. Woosley, A. Heger, and T. A. Weaver. "The evolution and explosion of massive stars". In: *Rev. Mod. Phys.* 74 (4 Nov. 2002), pp. 1015–1071. DOI: 10.1103/RevModPhys.74.1015 (cit. on p. 64).

[Wie+13] F. Wienholtz, D. Beck, K. Blaum, et al. "Masses of exotic calcium isotopes pin down nuclear forces". In: *Nature* 498 (2013), pp. 346–349. DOI: 10.1038/nature12226 (cit. on pp. 21, 22, 33, 48, 60).

[WJT94a] J. Witti, H.-T. Janka, and K. Takahashi. "Nucleosynthesis in neutrino-driven winds from protoneutron stars II. The r-process". In: *Astron. Astrophys.* 286 (1994), pp. 857–869 (cit. on p. 64).

[WJT94b] J. Witti, H.-T. Janka, and K. Takahashi. "Nucleosynthesis in neutrino-driven winds from protoneutron stars I. The α-process". In: *Astron. Astrophys.* 286 (1994), pp. 841–856 (cit. on p. 64).

[Wol+12a] R.N. Wolf et al. "On-line separation of short-lived nuclei by a multi-reflection time-of-flight device". In: *Nucl. Instrum. Methods A* 686 (2012), pp. 82 –90. DOI: 10.1016/j.nima.2012.05.067 (cit. on pp. 28, 31, 32).

[Wol+12b] R. N. Wolf, G. Marx, M. Rosenbusch, et al. "Static-mirror ion capture and time focusing for electrostatic ion-beam traps and multi-reflection time-of-flight mass analyzers by use of an in-trap potential lift". In: *Int. J. Mass Spectr.* 313 (2012), pp. 8–14. DOI: 10.1016/j.ijms.2011.12.006 (cit. on pp. 22, 32).

[Wol+13] R. N. Wolf et al. "Plumbing Neutron Stars to New Depths with the Binding Energy of the Exotic Nuclide ^{82}Zn". In: *Phys. Rev. Lett.* 110 (2013), p. 041101. DOI: 10.1103/PhysRevLett.110.041101 (cit. on pp. 21, 33, 48).

[Wol13] H. Wollnik. "Static-mirror ion capture and time focusing for electrostatic ion-beam traps and multi-reflection time-of-flight mass analyzers by use of an in-trap potential lift". In: *Int. J. Mass Spectr.* 349-350 (2013). 100 years of Mass Spectrometry, pp. 38 –46. DOI: 10.1016/j.ijms.2013.04.023 (cit. on p. 22).

[WP90] H. Wollnik and M. Przewloka. "Time-of-flight mass spectrometers with multiply reflected ion trajectories". In: *International Journal of Mass Spectrometry and Ion Processes* 96.3 (1990), pp. 267 –274. DOI: 10.1016/0168-1176(90)85127-N (cit. on p. 23).

[Yaz06] Chabouh Yazidjian. "A new detector setup for ISOLTRAP and test of the Isobaric Multiplet Mass Equation". PhD thesis. l'Universite de CAEN, 2006 (cit. on p. 17).

[Yor+13] D. T. Yordanov, D. L. Balabanski, J. Biero ń, et al. "Spins, Electromagnetic Moments, and Isomers of $^{107\text{-}129}$Cd". In: *Phys. Rev. Lett.* 110 (19 May 2013), p. 192501. DOI: 10.1103/PhysRevLett.110.192501 (cit. on p. 48).